Structural Parameters (Size, Defect and Doping) of ZnO Nanostructures and Relations with their Optical and Electrical Properties

Dissertation

zur Erlangung des Doktorgrades

Dr. rer. nat.

vorgelegt der
Fakultät für Mathematik und Naturwissenschaften der
Technischen Universität Ilmenau

von
M. Sc. Yaoguo Fang
Ilmenau

TECHNISCHE UNIVERSITÄT
ILMENAU

Doktorvater und 1. Gutachter: Prof. Dr. Yong Lei
2. Gutachter: Prof. Dr. Gerhard Wilde
3. Gutachter: Prof. Dr. Heiko O. Jacobs

Tag der Einreichung: 14.06.2016

Tag der wissenschaftlichen Aussprache: 26.01.2017

urn:nbn:de:gbv:ilm1-2017000012

Die Arbeit wurde von Prof. Dr. Yong Lei betreut.

Abstract

The performance and properties of the ZnO nanostructure-based devices (mainly including the wire-like and leaf-like structure) are highly dependent on the sizes, defects and doping of ZnO. Therefore, it is necessary to investigate these parameters in the ZnO nanostructure for optimizing its properties, hence providing the motivation of this PhD work. In this thesis, ultralong ZnO nanowires (NWs), indium (In)-doped leaf-like and needle-like ZnO nanostructures, which are fabricated via the chemical vapor deposition (CVD) process and hydrothermal method, have been investigated in details for the relationship of the sizes, defects and doping with their properties. Firstly, a number of analysis techniques are used to understand the correlation between the defects and sizes (diameter and length) of the ZnO NWs. The results show that the concentration of oxygen vacancies (V_o) jointly with zinc interstitials (Zn_i) defects is observed to be positively correlated with the increasing sizes of the NWs. Importantly, it is found that the variation of the field-enhancement factor (β) of the ZnO NWs in field emission is highly dependent on the concentration of V_o with the length of the NWs. As compared with the ultralong and needle-like ZnO NWs, In-doped ZnO nanostructure has the lowest turn-on and threshold field as well as its relatively high β value. The reason is ascribed to the specific leaf-like morphology and In doping. Therefore, knowledge of the correlation and inter-relationship between the amount and type of native intrinsic defects or doping present in the NWs as their size varies is a crucial step towards optimizing and tuning the performances of ZnO nanostructure-based devices.

Zusammenfassung

Die Eigenschaften und Leistung von Gerätschaften, welche auf ZnO-Nanostrukturen basieren (vornehmlich drahtähnliche und blattähnliche) hängen im Wesentlichen von der Größe der Nanostrukturen, denen in ihnen auftretenden strukturellen Defekten sowie der Dotierung des ZnO ab. Daher ist es nötig diese Parameter in ZnO zu untersuchen um dessen Eigenschaften optimieren zu können, was somit auch die Motivation für diese Dissertationsschrift darstellt. In dieser Arbeit wurden Größen, Defekt- und Dotierungseffekte auf die Eigenschaften von ultralangen ZnO-Nanodrähten, In-dotierten blattähnlichen ZnO Strukturen sowie nadelförmigen ZnO-Nanostrukturen untersucht, welche mittels chemischer Gasphasenabscheidung (CVD) und einer hydrothermalen Abscheidungsmethode hergestellt wurden.

Zunächst wurde eine Vielzahl von Analysetechniken angewendet um die Korrelation zwischen den auftretenden Defekten und der Größe, respektive dem Durchmesser und der Länge, der ZnO-Nanodrähte zu ermitteln. Die entsprechenden Resultate zeigen, dass eine steigende Konzentration von Sauerstoffleerstellen (V_o) in Kombination mit einer steigenden Konzentration von Zn Zwischengitterdefekten (Zn_i) für eine ansteigende Größe der Nanodrähte verantwortlich ist. Besonders erwähnenswert ist, dass die Variation des Feldverstärkungsfaktors (β) der ZnO-Nanodrähte bei Feldemission erheblich von der Konzentration der Sauerstoffleerstellen (V_o) in Kombination mit der Länge der Nanodrähte zusammenhängt.

Im Vergleich mit den ultralangen und nadelförmigen ZnO-Nanodrähten, weisen die In-dotierten Nanostrukturen das niedrigste Anschalt- und Grenzfeld sowie den relativ höchsten Feldverstärkungsfaktor β auf. Der Grund hierfür wird der blattähnlichen Morphologie sowie der Dotierung zugesprochen. Daher ist das Wissen um die Korrelation zwischen der Menge und der Art von natürlichen intrinsischen Defektstrukturen sowie der Dotierung in den

Nanodrähten mit sich ändernder Größe der Strukturen ein wichtiger Schritt in Richtung einer Optimierung und eines allgemeinen Tuningprozesses von Geräten, welche auf ZnO-Nanostrukturen basieren.

Table of Content

List of Figures

List of Abbreviations

A^*	the effective Richardson constant
A^{**}	the reduced effective Richardson constant
AAO	anodic aluminum oxide
C	Concentration Value
CAFM	conductive atomic force microscopy
CBD	chemical bath deposition
$C_6H_{12}N_4$	hexamethylenetetramine
CPL	confocal photoluminescence
CVD	chemical vapor deposition
CRT	cathode ray tube
CTRPLS	confocal time-resolved photo-luminescence spectroscopy
DL	deep-level emission
DLTS	deep-level transient spectroscopy
E	the applied field
EDX	energy-dispersive X-ray spectroscopy
EDTA-2Na	ethylenediaminetetraacetic acid disodium salt
Eg	band gap
EL	electroluminescence
EDLCs	electrical double-layer capacitors
FE	field emission
FED	field emission display
F-N	Fowler-Nordheim
FTO	fluorine-doped tin oxide
FFT	fast-Fourier transformed
GaN	gallium nitride
h	Planck's constant
HMTA	hexamethylenetetramine
In_2O_3	indium oxide
$I_{S,Pt-NW}$	the saturation current
I-V	current-voltage
J	the current density
J-E	the current density-electric field
K	the Boltzmann constant

LO	longitudinal optical
LED	light emitting diode
m_e^*	electron effective mass
m_o	electron rest mass
MOCVD	metal organic chemical vapor phase deposition
NPs	nanoparticles
N_d	the donor concentration
NFs	nano-flowers
NRs	nanorods
NW	nanowire
NZO	N doping ZnO
O_i	interstitial O
P	the actual vapor pressure
P_o	the equilibrium vapor pressure
P_N	the nucleation probability
PEC	Photo electrochemical
PS	polystyrene
PVD	physical vapor deposition
Q	elementary charge
QCE	the quantum confinement effect
$r_{NW,average}$	the average radius
RhB	Rhodamine B
S	the slope of the F-N plot
SAED	selected area electron diffraction
SCs	supercapacitors
FESEM	field emission scanning electron microscopy
Sccm	standard cubic centimeters per minute
SnO_2	tin oxide
S/V	surface-to-volume
SnO_2	tin oxide
T	the absolute temperature in Kelvin
TEM	transmission electron microscopy
TO	transverse optical
τ_1	fast radiative decay
τ_2	slow radiative decay
τ_f	fast time constant

τ_B	decay time constant of bulk materials
τ_s	slow time constant
$\tau_{average}$	the average lifetime
UV-Vis	Ultraviolet-visible spectroscopy
UTAM	ultra-thin alumina mask
V_o	O vacancies
V_{Zn}	Zn vacancies
VLS	vapor-liquid-solid
VS	vapor-solid
WO_3	tungsten trioxide
Xe	xenon
XPS	X-ray photoelectron spectroscopy
Zn_i	interstitial Zn
ZnO	zinc oxide
$Zn(NO_3)_2{\cdot}6H_2O$	zinc nitrate hexahydrate
β	field-enhanced factors
σ	the surface energy of the solid whisker
ε_s	the permittivity
ε_r	the relative permittivity
ε_o	the permittivity of free space
α	the supersaturation ratio
Φ	the work function

1 Introduction

ZnO is a wide-bandgap semiconductor with a hexagonal wurtzite structure and possesses a number of fundamental advantages including the band gap of 3.37 eV, large exciton binding energy (60 meV), strong room-temperature luminescence, and high electron mobility.[1, 2] Over the years, investigation of the ZnO nanostructures has been considered as one of the hottest research area. Among these nanostructures, ZnO nanostructures have many unique advantages including controllable morphology, high mechanical strength, and chemical stability etc., thereby they have been utilized as an essential candidate for multifunctional applications in optical and electrical devices, such as field emission,[3-5] nano-piezotronics,[6, 7] sensors,[8-11] and water splitting[12, 13] etc. Importantly, in these applications, the structural parameters (sizes, defects, and doping)[14-18] play an important role. Therefore, investigation of the structural parameters become more and more imperative for optimizing the performance of the ZnO nanostructure-based devices. However, only a few articles have been focusing on this field. In this thesis, the correlation between the structural parameters and performance of ZnO nanostructures (mainly including the wire-like and leaf-like structure) in the optical and electrical applications is studied. Firstly, the combined spectroscopic techniques [X-ray powder diffraction (XRD), X-ray photoelectron spectroscopy (XPS), photoluminescence (PL), ultraviolet-visible spectroscopy (UV-Vis), confocal photoluminescence (CPL), conductive atomic force microscopy (CAFM), and confocal time-resolved photoluminescence spectroscopy (CTRPLS)] are performed to investigate the important role of the native intrinsic defects in affecting the properties of the ZnO NWs. The relationship between the concentration of V_o and Zn_i defects with the donor concentration and the length of the NW are observed to be positively correlated. An analytical model which is verified by the Hall measurements is derived which can directly calculate the donor concentration of the NWs from the reverse biased current-voltage (I-V) characteristics.

Secondly, ZnO nanostructures with different morphologies are fabricated on the silicon substrate. For example, well-aligned and ultralong ZnO NW arrays, as well as the leaf-like ZnO nanostructures (which consist of modulated and single-phase structures), are fabricated by the CVD method without the assistance of catalysts. On the other hand, needle-like ZnO NW arrays are fabricated with the CVD process followed by the chemical etching of the NW arrays. As compared with the ultralong and needle-like ZnO nanostructures, In-doped leaf-like ZnO nanostructures possess the best emission performance where the reasons are ascribed to the specific morphology and In doping.

The detail information of this thesis is given as follows: In the chapter 2, the background of ZnO nanostructures is introduced including the properties, different synthesis methods and applications. The characteristic techniques are introduced to investigate the structural parameters of the ZnO nanostructures and performance as well as the correlation between them in the chapter 3. This section highlights the role of the structural parameters (sizes, defects and doping) in the optical and electrical performance, such as the field emission, sensor, water splitting, photocatalysis, and piezoelectric effect.

Chapter 4 presents a detailed overview of the experimental and instrumental conditions, which are used to synthesize and characterize the ZnO nanostructures, respectively. The morphologies and chemical compositions of the ZnO nanostructures are investigated by the field emission scanning electron microscopy (FESEM), transmission electron microscopy (TEM), EDX, XPS, and XRD. On the other hand, the optical properties are characterized by the PL, CPL, UV-Vis, and CTRPLS. The electrical properties of the ZnO nanostructures are investigated via the CAFM, Hall and field emission system.

The results and discussions are shown in the chapter 5, which consists of two main parts. The first part is that the combined spectroscopic approach is used as a systematic analysis strategy to investigate and understand the important role of the native intrinsic defects in influencing

the properties of the ZnO NWs. These results show that the correlation between the different measurements, the concentration of the V_o jointly with the Zn_i defects is observed to be positively correlated with the increasing NW sizes. Moreover, the CPL emission spectra show that at different spatial locations on the ZnO NW surfaces, the spectra near the NW edges is observed to have maximum intensity, which subsequently decreases to a minimum near the NW center. For the NW arrays, similar intensity distribution of the CPL emission spectra is also visually shown. These results are important for understanding the optical response of the ZnO NW-based devices. On the other hand, as the donor concentration plays a critical function in the properties of the ZnO NWs, an analytical model was derived for the calculation of the donor concentration of the NWs directly from its reverse-biased current–voltage characteristics that are obtained from the CAFM measurements.

In the second part, the TEM image shows that the In-doped ZnO leaf-like nanostructures consist of alternate bright field and darkfield regions where the darkfield parts belongs to pure ZnO, and the brightfield parts consist of a modulated structure of the ($In_2O_3(ZnO)_7$ or $In_2O_3(ZnO)_8$). Owing to the indium doping, the emission peak of the UV-vis spectra corresponding to the leaf-like structures was observed to be shifted to lower energy. From the field emission properties corresponding to the different nanostructures, the In-doped leaf-like nanostructures are more suitable for field emitter in microelectronic devices.

The section 6 summarizes the results and gives an outlook to this thesis.

Finally, section 7 provides a short summary of the other research works performed with other semiconductor materials for the nanostructure-based applications such as in supercapacitors or battery based applications.

2 Background

2.1 Properties of ZnO

2.1.1 Crystal structures

The crystal structures of ZnO consist of the wurtzite (Figure 2-1a), zinc blende, and rocksalt (or NaCl structure). Wurtzite ZnO has a hexagonal structure where the lattice parameters are a = 3.2495 Å and c = 5.2069 Å[19]. In the unit of hexagonal wurtzite, each anion is surrounded by four cations at the corners of a tetrahedron, and vice versa in figure 2-1a. This tetrahedral coordination is of the typical sp^3 covalent bonding nature, but the band of Zn-O also has a substantial ionic character, thus ZnO lies on the borderline between being classified as a covalent and ionic compound with an ionicity of f_i = 0.616 on the Phillips ionicity scale. [1, 7, 20-22]

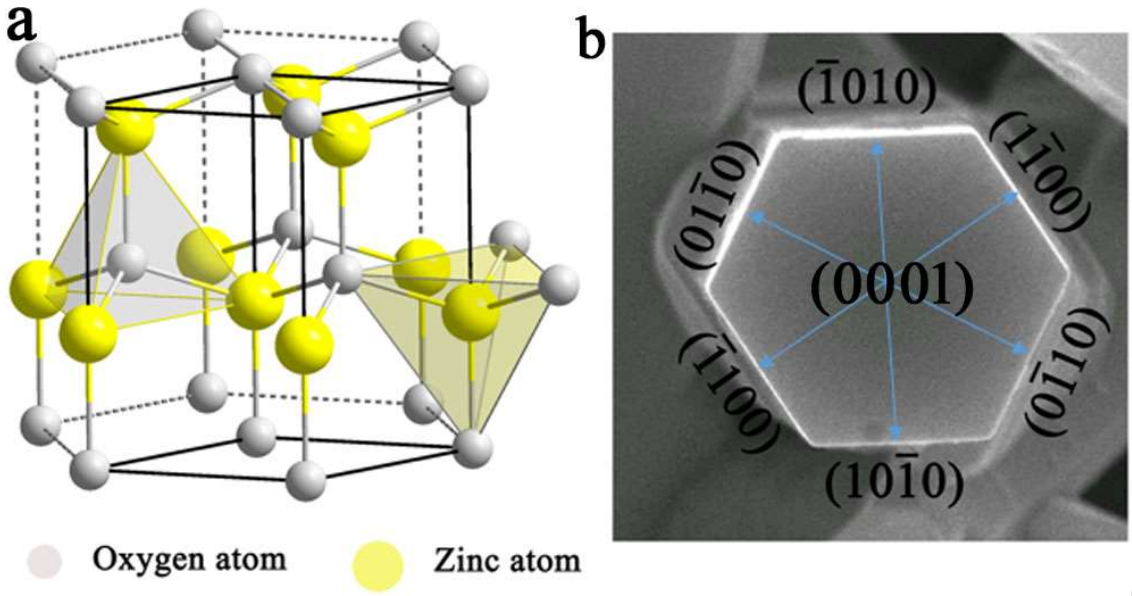

Figure 2-1. (a) The wurtzite phases of ZnO,[23] (Figure are redrawn from)[23] (b) SEM image of the top view of the ZnO NW with different crystal planes.

The hexagonal wurtzite structure of ZnO is the most common phase with a space group of C6v or P63mc, which occurs almost exclusively at ambient conditions.[24-26] The wurtzite

structure of ZnO can be simply described as a number of alternating planes which are composed of tetrahedrally coordinated O^{2-} and Zn^{2+} ions, that are alternatively stacking along the c-axis. This tetrahedral coordination gives rise to non-central symmetric crystal structure, which can influence various properties including its piezoelectricity and spontaneous polarization.[20, 27] Another important characteristic of the ZnO is polar/nonpolar surfaces. The four most common faces of wurtzite ZnO have polar surface ± (0001) which are either Zn or O terminated and the non-polar $(11\bar{2}0)$ (a-axis) and the $(10\bar{1}0)$ faces which both contain an equal number of Zn and O atoms (Figure 2-1b)[25, 28-30]. The oppositely charged ions produce the polar surface, resulting in a normal dipole moment and the spontaneous polarization along the c-axis as well as a divergence in the surface energy. In addition, these polar/nonpolar surfaces have different crystal growth rates at fixed conditions, which result in rich ZnO microstructures.[31, 32] Such as, with the presence of Indium atoms, the growth rate of the c-axes (0001) is hindered, while the side-face $(10\bar{1}0)$ grows fast to induce changing of the morphology from nanowires to nanobelts.[33]

2.1.2 Optical Properties

Photoluminescence (PL) spectra of the ZnO with different nanostructures have been extensively reported [34, 35]. Generally speaking, PL emission spectra of the ZnO NWs have two components. One is the typical exciton emission or near-band-edge emission, i.e., photo-generated electron recombination process with holes in the valence band or in traps near the valence band in the UV-Vis region, such as the 373[36], 378, [37-39] 380, [40-42] 381, [43] 383, [44, 45] 384-391, [46] 387, [46]389, [47, 48] and 390 nm.[49] The other component is the visible emission (also called deep-level emission, DL) which is related with defects, such as the peaks at 405, 420, 446, 466, 485, 510, 544, 583, and 640 nm emission in the visible region[50-54]. In defect chemistry[22, 55-57], several calculations of the native defect levels in ZnO have been reported as shown in figure 2-2b. The different emission spectra are related to the V_o, V_{Zn}, O_{Zn}, Zn_i and

O_i [58-63]. Such as the 3.15 eV peak (DL) in the violet region is due to the band transition from the Zn_i level to the valence band and the position of the Zn_i level is theoretically located at 0.22 eV below the conduction band.[58]

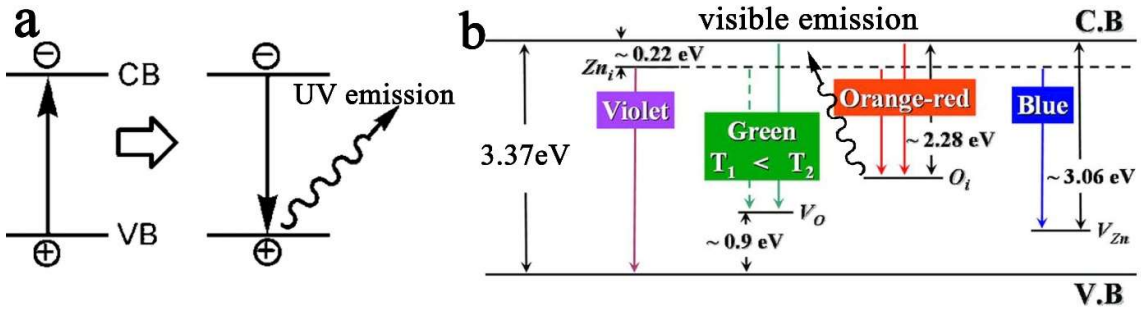

Figure 2-2. Two kinds of Photoluminescent processes for ZnO. (a) Typical exciton emission;[35] (b) schematic band diagram of DL in ZnO based on the full potential linear muffin-tin orbital method and the reported data.[58] (Figures are redrawn from [35, 58])

2.1.3 Doping of ZnO

Doping means intentionally introducing impurities into an extremely pure semiconductor.[64] It is well known that the doping of impurities greatly affects the basic physical properties, (e.g., electrical, optical, and magnetic properties). As for ZnO, doping can be divided into two categories as described below:

The doping of a cation is known as cationic doping; e.g. Al[65, 66], Sn[67], Ga[68], In[33, 69], Cd,[70] Cu,[71, 72] FeCo,[73] Mn,[74, 75] and Ni[76], which are used as cationic dopant. The doping of anions to ZnO is known anionic doping; e.g. As,[77] N,[78, 79] and S [80, 81], which are used as anionic dopant. On the other hand, there are two main topics according to these dopant function: (1) doping with donor and acceptor impurities to achieve high n-type or p-type conductivity, respectively; (2) doping with transition metals[71-75] or rare elements[82] to achieve the desired semiconductor properties. These effects have been systematically investigated for the majority of dopants and some changes in the semiconductor properties have been reported.[83-94] For example, incorporation of Al resulted in an increased bandgap

from 3.29 eV to 3.34 eV; a blue shift of the absorption peak and UV-Vis emission peak, and the ratio of UV-Vis to green emission decreased after doping.[66] In addition, ZnO nanowires are evolved into nanobelts after In-doping and so on.[33] Therefore, doping will act as a significant route to change the microstructures and practical performance of ZnO.

2.2 Synthesis methods

For fabrication of 1D ZnO nanostructures, many methods have been reported such as chemical-vapor deposition (CVD),[33, 95, 96] aqueous solution,[97-100] electrochemical deposition, [101-104] template,[95, 105, 106], PVD,[107] Molecular-beam epitaxy,[108] and rf magnetron sputtering method.[109]

2.2.1 Chemical vapor deposition (CVD)

In principle, the CVD method is a simple process where source materials (s) are vaporized with increased temperature and then the resultants with the vapor phase (s) react under the given conditions (temperature, pressure, atmosphere, substrate etc.) to form the desired products (s).[110] The key point for the CVD method is that the thermal evaporation process is very sensitive to the local temperature, pressure, the concentration of reaction gas, gas rate, and the location of the reactant source. In this thesis, ZnO, In_2O_3 and Carbon powder act as source materials to fabricate the ZnO NWs and In-doped leaf-like ZnO nanostructure using the CVD process. The specific details are shown in the experimental section.

Growth of the 1D ZnO nanostructures usually follows the vapor-liquid-solid (VLS) and vapor-solid (VS) principle. The VLS crystal growth mechanism was first proposed by Wagner and Ellis in 1964 for the Si whisker with the presence of Au and Sn as the catalysts [96]. In the VLS process, a liquid alloy droplet consisting of a pure metal catalyst (such as Au,[33] Sn[96]) and the component from the initial reaction of source materials (such as Si, III-V compound,

II-V compound, oxide) is first formed under the given reaction conditions. Then, the alloy droplets can be used as guidance for the growth of NWs with increasing reaction time.[111]

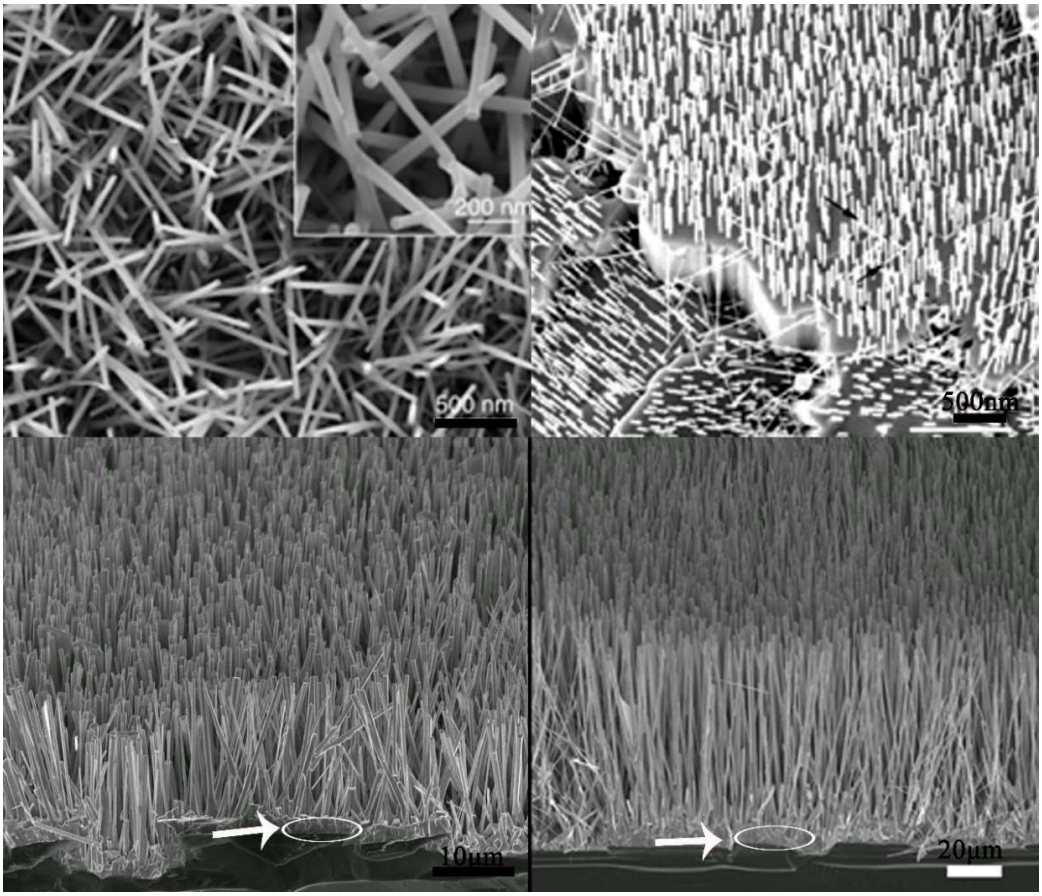

Figure 2-3 (a) Synthesis of the ZnO nanorods using Au as a catalyst, the inset shows Au particles at the tips.[7] (b) Aligned ZnO NWs epitaxial grown on the ZnO substrate using Sn as a catalyst.[96] (c) and (d) ZnO NWs grown on the ZnO seed layers (the white ellipses) for 10 and 20 mins, respectively. (Figures are taken from [7, 96])

Z.L. Wang's group has reported that the orientation-ordered ZnO nanorods grow on a polycrystalline Al_2O_3 substrate with assistance of the Au or Sn catalyst in figure 2-3a and b. [7, 96, 111] As for the VS process, without the presence of catalysts, the ZnO NWs can also be fabricated using the ZnO seed layers instead of the Au catalyst. In my work, without the presence of catalysts, a seed layer of ZnO is grown on the Si substrate by the spin-coating method. Well-ordered ZnO NWs length of ~90 μm are fabricated on the seed layers as shown

in figure 2-3c and d. The white ellipse positions visibly show the ZnO seed layers. In addition, the reason for the vertical ZnO NWs on the seed layers is that the crystal structure of the ZnO seed layers perfectly matches with the lattice of the ZnO NWs, which result in the NW perpendicular growth on the seed layers.

2.2.2 Aqueous solution

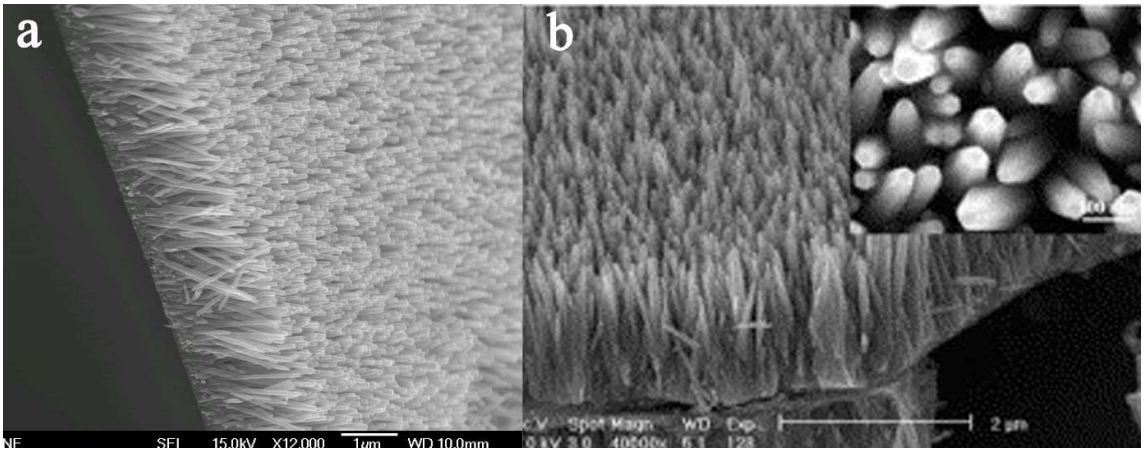

Figure 2-4. (a) Well-ordered ZnO NW arrays by the aqueous chemical method. (b) ZnO nanorods with the tailored dimensions.[99] (Figure is taken from [99])

Aqueous synthesis can be defined as a synthesis method for crystals that depend on the solubility of minerals in hot water under sealed environment.[112] With the increasing reaction time, the reaction products are generated on the substrates or with deposition. L. Vayssieres. reported the fabrication of highly oriented ZnO NWs via a aqueous solution method at 95 ^{o}C[113]. This method offers a classic strategy to fabricate the ZnO NWs. Figure 2-4a shows the well-ordered ZnO NW arrays with the diameter of ~80 nm and length of ~1.5μm. In addition, the well-aligned ZnO nanorod arrays are also prepared on substrates by the hydrothermal growth under different conditions in figure 2-4b. The growth conditions such as the pre-treatment of the substrates, growth temperature, deposition time and the concentration of the precursors have great influence on the ZnO nanorod morphologies. In terms of application,

the uniform ZnO nanostructures with the tailored dimension that are perpendicularly grown on the substrate are beneficial for the field emission applications. [99]

2.2.3 Template

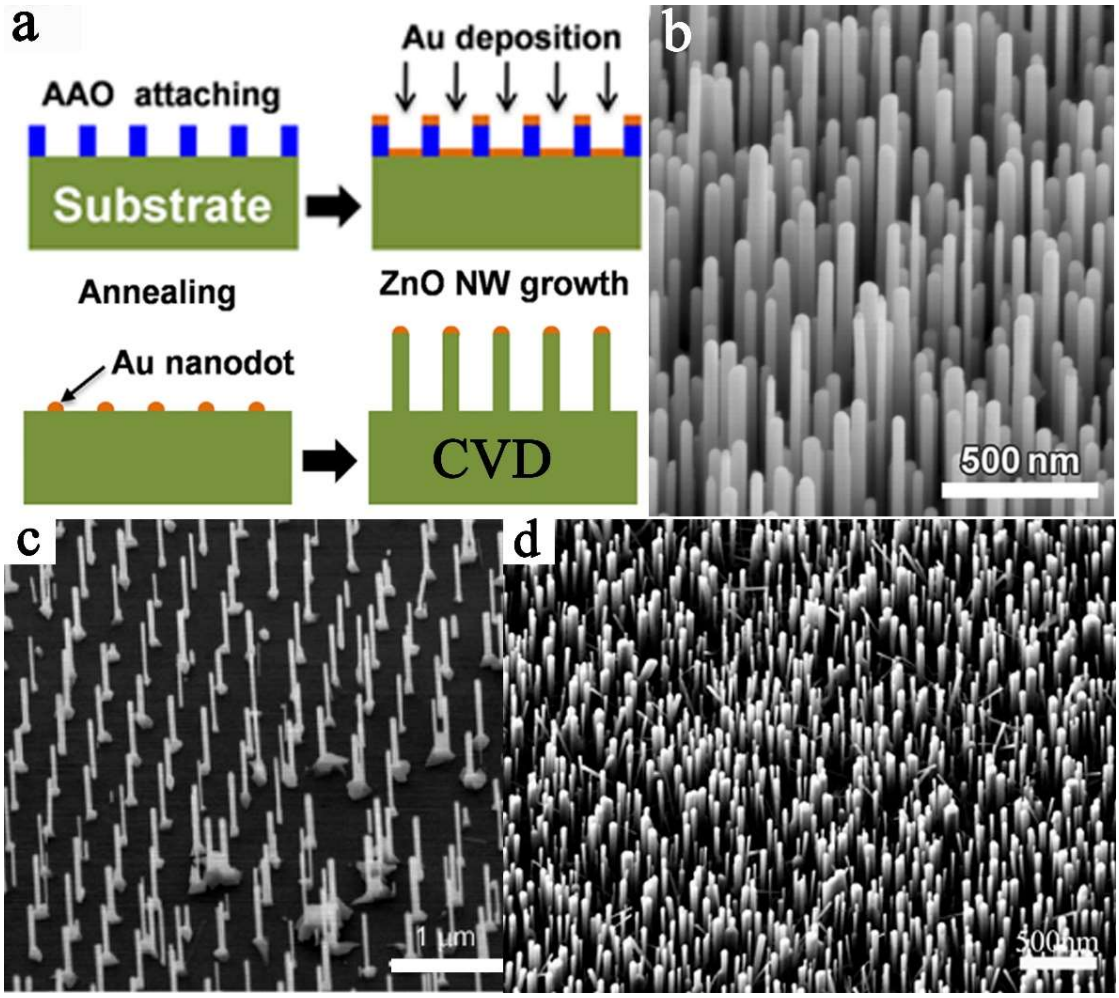

Figure 2-5. (a) Schematic of the fabrication process of the Au nanodots and ZnO NWs; (b), (c) and (d) well-aligned ZnO NW grown on the ZnO film/GaN/UTAM with Au pattern, respectively. (Figures are taken from [95, 114])

From the application views, it is essential to control their location, alignment and packing density for the ZnO nanostructures, such as field emission. To realize these goals, some patterned technologies (such as template, lithographic and non-lithographic patterning techniques) are used to produce the shadow masks for the catalysts (Au, Ag etc.[95])

deposition. Among them, the common templates route include the hard template (anodized aluminum oxide, AAO[115]) and soft template, (Polystyrene, PS[116]).[117] Figure 2-5a shows the schematic of the fabrication process of the Au nanodots and ZnO NWs. After the CVD process, the self-assembled vertically aligned ZnO nanorod arrays are generated on the GaN, ZnO and UTAM (ultra-thin alumina membrane)[95, 114, 115] substrates with the gold dots pattern in figure2-5b, c, and d, respectively. In addition, these template methods combined with the electrochemical deposition or sol-gel method, well-ordered ZnO nanostructures can also be prepared.

2.2.4 Electrochemical deposition

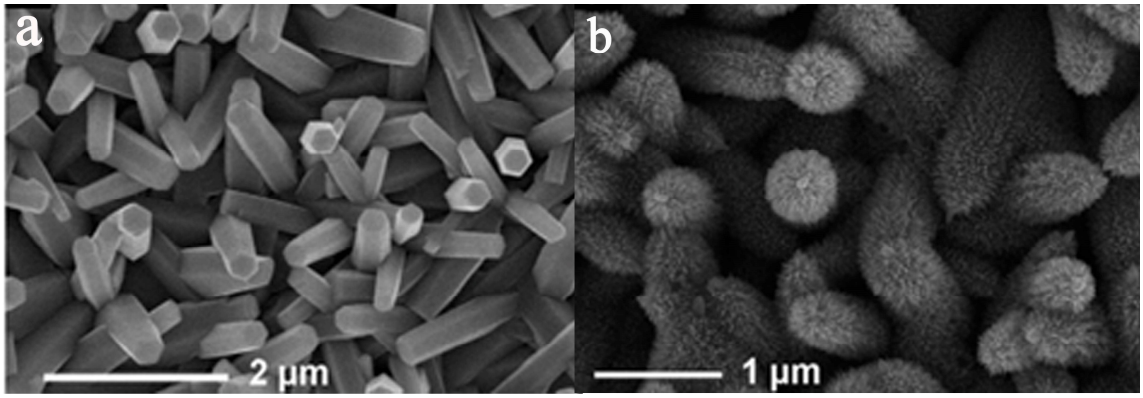

Figure 2-6 SEM images of the branched hierarchical ZnO NWs are synthesized by the two-step electrodeposition process, the first (a) and second-step (b).[102] (Figures are taken from[102])

Electrochemical deposition is a process that metal, oxide, or salt can be deposited onto the surface of a conductor substrate by the simple electrolysis of a solution containing the desired metal ion or its chemical complex[118]. For example, Ravi Chander has reported the electrodeposition of ZnO nanorods from aqueous solution.[104] The nanorods have a well-defined hexagonal morphology. Moreover, the branched hierarchical ZnO NWs are synthesized on the fluorine-doped tin oxide (FTO) substrate via a two-step electrochemical

deposition process in figure 2-6a and b. In addition, the NWs (mean diameters from 25 to 80 nm) with conical shape at the tip are obtained by modifying the $ZnCl_2$ concentration, which are very interesting in the area of field emission. But the disadvantage is the short length of the NWs.[102]

2.2.5 Other synthesis methods

Apart from the above process for the fabrication of the ZnO nanostructures, other methods such as the pulsed-laser deposition, sol-gel, molecular-beam epitaxy etc. have also been developed in parallel.[107-109]

2.3 Other morphologies of the ZnO nanostructures

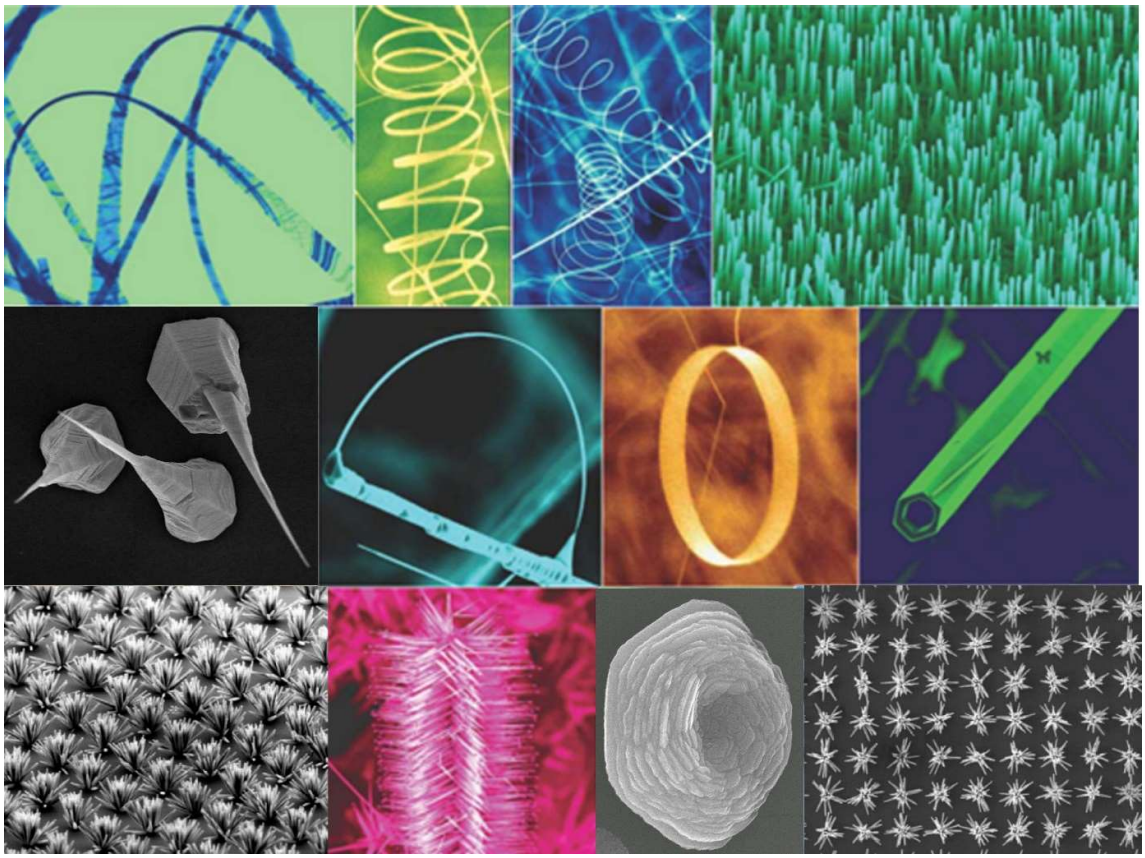

Figure 2-7 Several ZnO nanostructures (Figures are redrawn from [119-121]).

Here, the ZnO nanostructures are presented including nanobelts, nanohelixes, NWs, nanocombs, branched hierarchical structures, nanotubes and nanorings in figure2-7.[120] Apart from these, a rich family with related properties have been reported.[120, 122] The possible reasons for the ZnO wurtzite structure (as seen in section 2.2.1) are the noncentral symmetry, polar/nonpolar surfaces and the crystal planes with different growth rates. These novelty morphologies having its own features are beneficial for applications in the semiconductor field.

2.4 Applications

2.4.1 Field emission

Field emission (FE) is a process in which the electrons below or close to the emitter Fermi level escape from the emitter surface with the aid of a high electric field depressing the surface barrier.[123] Based on this theory, the development of nanomaterials with good field emission capability evoked the application of cold cathodes in vacuum devices, such as the field emission displays (FED) and field emission lighting. Figure 2-8a shows the development of the display technology, which move towards the lightweight, cheap and bright display from the cathode ray tube (CRT) to FED.[124] To realize the technology, emitter materials with high emitter density and stability have drawn much attention. Currently, those materials with the micro-and nano-fabrication technologies have been developed for enhanced FE-based devices, such as carbon nanotubes,[125, 126] In_2O_3,[127] Si NWs,[128] SnO_2,[129] WO_3[130] etc. Among all the oxide semiconductors, ZnO has been considered as one of the most promising materials for field emitters owing to its mechanical strength, thermal stability, high oxidation resistivity, low electron affinity and controllable morphologies.[3, 4, 100, 131-134]

Combined with the various pattern methods (template, electron beam lithography, nanolithographic), various ZnO nanostructures with controllable sizes and densities have been

investigated to obtain high-performance field emitter arrays, such as nanoneedle arrays,[3, 135] nanosheets,[5] NWs,[136, 137] tetrapod [138]and doping structures.[139, 140] For an analysis of the field emission properties of the different ZnO nanostructures, the following Fowler-Nordheim (F-N) equation would have to be used:[123]

$$J = \frac{A\beta^2 E^2}{\varphi} \exp\left(-\frac{B\phi^{3/2}}{\beta E}\right) \qquad 2\text{-}1$$

where J is the current density, E is the applied field strength, A and B are constants with the values of $1.56\times10^{-10}AV^{-2}$ eV and $6.83\times103V\ (eV)^{-3/2}\mu m^{-1}$, respectively, ϕ is the work function of the emitter which was taken as 5.4 eV for ZnO from the literature, and β is the so-called field-enhancement factor, which reflects the ability of the emitters to enhance the local electric field. The field-enhanced factors β can be calculated from the formula $\beta = -B\phi^{3/2}/S$, where S is the slope of the F-N plot.

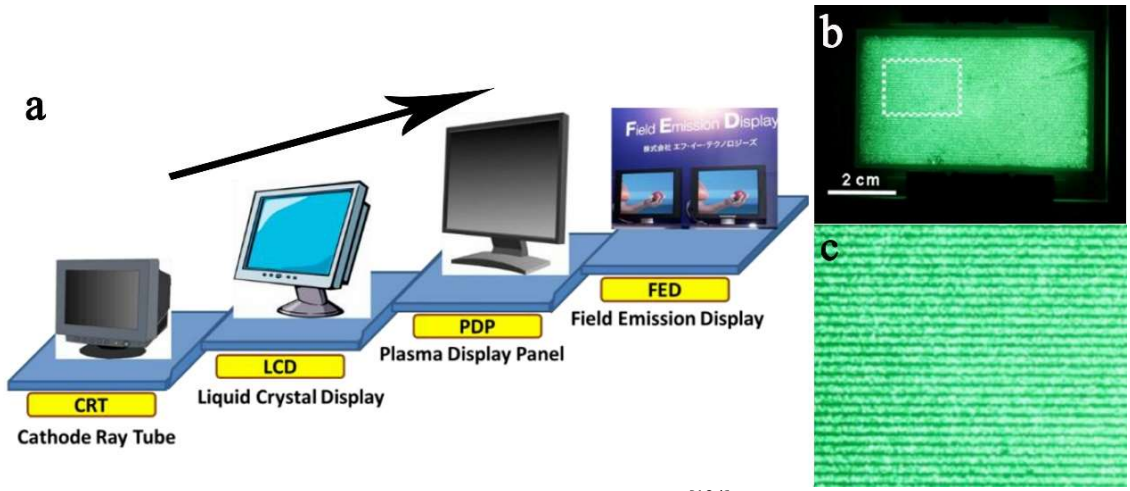

Figure 2-8. (a) Development of display technologies.[124] (b) The typical field emission image. (c) The enlarged field emission image from part of the fluorescent screen.[4] (Figures are redrawn from [4, 124])

As for field emission materials, their structural parameters such as high aspect ratios, small tip radius of curvature, defects, and doping, play an important role on the enhancement of the properties.[3, 4, 131, 134, 138, 140, 141] Fox example, C. X. Zhao reported that good alignment and

dense ZnO NWs could be grown on the silicon or glass substrates with tunable distribution density and morphology.[4, 133] Figure 2-8b shows a typical field emission image, which reveals that the emission image is extremely uniform, and almost all the parts of the patterns can emit electrons.[4]

2.4.2 Water splitting

Photoelectrochemical (PEC) water splitting is a highly-efficient and eco-friendly route to meet the human demand for directly converting solar energy into chemical energy in the form of hydrogen.[142] Nanometer-sized metal oxide semiconductors with higher surface-to-volume ratio and shorter transport paths for the carriers are particularly prevalent for water splitting applications.[13, 143, 144] Figure 2-9 shows the main mechanisms for explaining the enhanced PEC water slitting efficiency of the Au/branched-ZnO NW photoelectrode.[144]

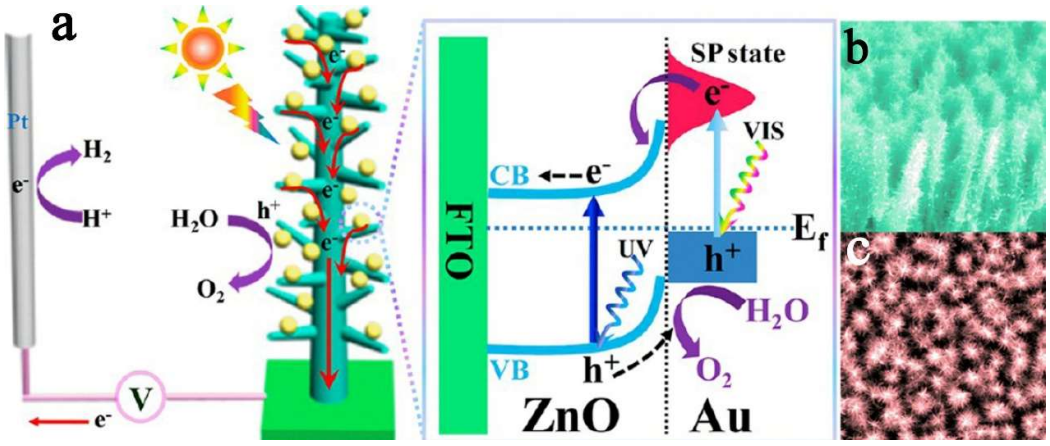

Figure 2-9. (a) Left panel: simplified schematic diagram of the PEC water splitting cell consisting of the Au/B-ZnO (branched-ZnO) NWs photoanode. Right panel: Energy level diagram for the Surface plasmon resonance (SPR)-mediated electron transfer process in the UV-Vis region. (b) Top and (c) cross-section view SEM images of the B-ZnO NWs with the Au NPs.[144] (Figures are taken from [144])

2.4.3 Piezotronic effect

Piezotronics is about the devices fabricated using the piezoelectric potential as a “gate” voltage to the tube/control charge carrier transport at a contact or junction.[8, 145] For wurtzite structure of ZnO NWs, because of their non-central symmetric crystal structure and polar/nonpolar surfaces, the piezoelectric effect is generated once the material is strained. If a stress is applied at an apex of the tetrahedron, the center of the cations and the center of the anions are relatively displaced resulting in a dipole moment in figure 2-10a. A constructive dipole moments created by all of the units in the crystal results in a macroscopic potential drop along the straining direction in the crystal, which produces the piezoelectric potential.[8, 145]

Figure 2-10b, c and d show the nanogenerator schematic that used aligned ZnO NWs for converting nanoscale mechanical energy into electric energy.[6] The mechanism of the nanogenerator depend on the piezoelectric and semiconducting properties of the ZnO NW. The Schottky-contact between the NWs and metal tip (as seen in Figure 2-10c) plays an important role on the energy conversion process. Furthermore, the Schottky-contact sensors are achieved by tuning the Schottky barrier height at the local metal-semiconductor interface, which dominates the carrier transport process through the whole device. Piezoelectric effect is a universal effect that provides an effective approach to improve the sensitivity, response time and general properties of the Schottky-contact NW sensors, including bio/chemical, gas, humidity, temperature sensing and others.[8, 146]

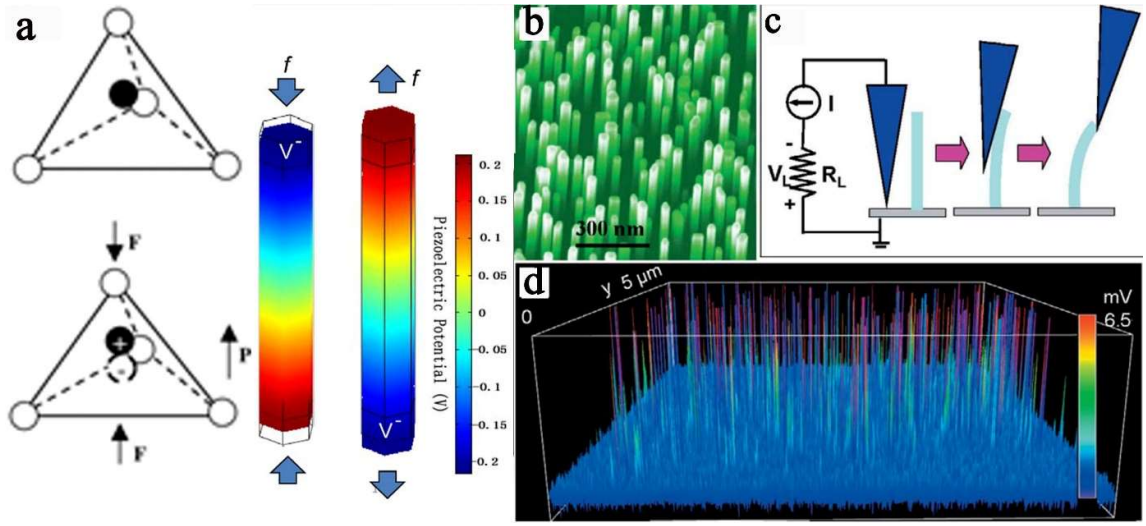

Figure 2-10 (a) Schematic diagrams showing the piezoelectric effect in a tetrahedrally coordinated cation-anion unit. Numerically calculated distribution of the piezoelectric potential along the ZnO NW under axial strain.[8] (b) SEM images of the aligned ZnO NWs. (c) Experimental setup for generating electricity through the deformation of a semiconducting and piezoelectric NW using a conductive AFM tip. The scanning process is in a contact mode. (d) An image of the output voltage (Figures are redrawn from [6, 8, 146]).

2.4.4 Other properties

Due to its low cost, environment friendly and unique optical-electric properties, ZnO is considered as an important material for applications, such as for photo-catalysis, gas sensor, light emitting diode, solar cells and so on.[8, 146]

3 Investigation of the ZnO NWs and properties

ZnO NWs with high surface area-to-volume ratio, aspect ratio, electron mobility, confinement effect, and easy fabrication are considered as important candidates in the electrical and optical devices applications. Remarkably, the performance of the ZnO NWs-based devices are intimately related to the structural parameters, such as sizes, and the native intrinsic or artificially induced defects and doping where these parameters can alter the optical and electrical properties. Therefore, it is necessary to insightfully study this area. The following section will introduce several characteristic techniques to investigate the structural parameters of the ZnO NWs and the performance of their devices as well as the relationship between them.

3.1 Characterization of ZnO NWs

Characterization techniques play an important role in the field of materials research.[131, 133, 134, 136, 140] Each of them has some advantages as well as some limitations. To systematically investigate the structural parameters of the ZnO NWs, the combined techniques including XRD, XPS, SEM, TEM, UV-Vis, PL, CPL, CTRPLS and Hall effect become necessary. For example, X-ray diffraction (XRD) technique[147] is extremely important not only to check the structural purity but also to identify the point defects, extended defects and dislocation-related disorder. Figure 3-1a shows the XRD patterns of the ultralong ZnO nanorod arrays annealed in air or a vacuum at various heat-treatment temperatures.[148] The diffraction peak of (002) plane of the ZnO nanorod array shifts to lower angles from 34.58° to 34.5° with increasing annealing temperature from 200 to 550 °C in air. It is attributed to the increase in the concentration of the oxygen-related defects in the ZnO nanorods, such as oxygen interstitials (O_i).[148]

Details of the surface chemistry and chemical binding states of the fabricated samples are studied by XPS. As shown in figure 3-1b of the XPS spectra, O1s peak shows an asymmetric

shape, which can be de-convoluted into three sub-peaks at binding energies of 530.83, 531.43, and 532.65 eV corresponding to the O^{2-} of Zn-O, oxygen deficient state, and chemically adsorbed oxygen, respectively. Similar results have also been reported by other groups.[149-153]

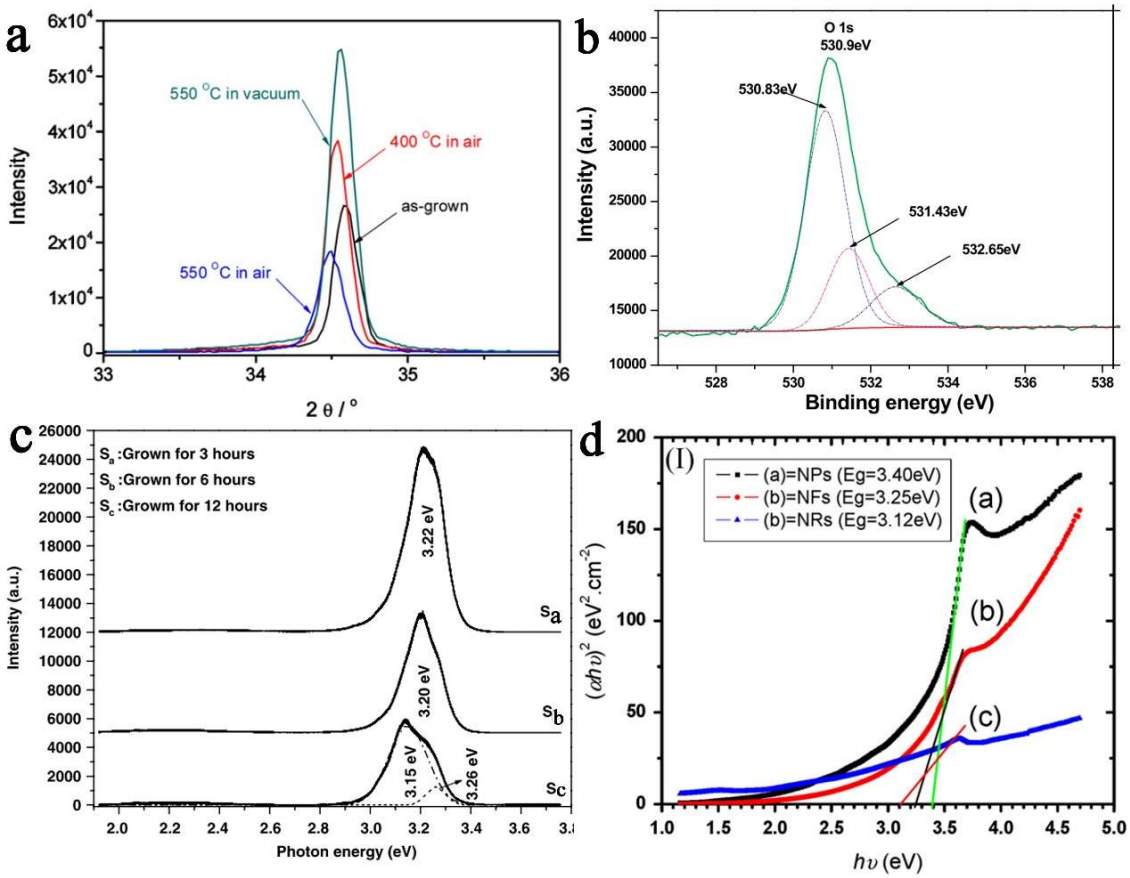

Figure 3-1. (a) The XRD patterns of the ZnO nanorod arrays at different temperatures.[148] (b) XPS spectra of the O 1s peaks ZnO nanoneedle.[153] (c) PL spectra of the Sa, Sb and Sc ZnO microrods.[150] (d) Plots of $(\alpha h\upsilon)^2$ against photon energy ($h\upsilon$) of the ZnO nanoparticles (NPs), nanoflowers (NFs) and nanorods (NRs), respectively.[151] (Figures are redrawn from[148, 150, 151, 153])

In figure 3-1c, the outstanding emission peaks of the Sa and Sb ZnO microrods center are at 3.22eV and 3.20eV, respectively. Compared with Sa and Sb, the UV emission band of the Sc microrods is broadened and weakened, which can be resolved into two peaks centering at 3.15eV and at 3.26eV, respectively.[150] These results indicate that the UV emission peaks of

the ZnO microrods have a redshift tendency with the increasing growth time, which can be ascribed to the degeneration of the (002) crystalline planes in the ZnO microrods. In addition, figure 3-1d show that the Plots of $(\alpha h\upsilon)^2$ against photon energy (hv) have a linear region and the extrapolation of the straight line to zero absorption give the energy gap (Eg) for various morphologies of the ZnO nanostructures [nanoparticles (NPs), nano-flowers (NFs) and nanorods (NRs)] from 3.40 eV to 3.12 eV.[151] The reason is that the difference of the optical Eg with the different morphologies is related to the variation of the stoichiometry of the ZnO samples and the concentration of the point defects.

Optical characterizations of the NWs are performed with the confocal photoluminescence (CPL) and confocal time-resolved photo-luminescence spectroscopy (CTRPLS) which is a contactless method for understanding the dynamics of the carriers involved in the optical processes such as the temporal information on the recombination lifetime as well as the optical emissions at specific wavelengths from the intrinsic defects in the ZnO NWs.

As shown in figure 3-2a, the PL spectra consisted of a dominant UV-Vis peak at 385 nm and a very weak deep level emission (green emission band) with a broad feature in the range of 500-600 nm.[154] The UV-Vis emission band is related to a near band-edge transition of ZnO namely, the recombination of the free excitons. While the deep level (DL) emission band is generally attributed to the DL defects[58] such as O vacancies (V_o), Zn vacancies (V_{Zn}), interstitial O (O_i), interstitial Zn (Zn_i), and extrinsic impurities such as substitutional Co, Eu, N, and C.[83, 87, 91, 93, 94]

Figure 3-2b[155] shows that the time-resolved PL detected at 383 nm from the ZnO nanorod arrays under different excitation fluences. When the excitation fluences ($133\mu J/cm^2$) is higher than the threshold, the transient PL is dominated by a 30 ps decay process. Below the threshold (116 $\mu J/cm^2$ excitation fluence), the decay fits well to a biexponential function with a fast time constant (τ_f) and a slow time constant (τ_s). By a least-square fitting, τ_f and τ_s and

the amplitude of τ_s are ~ 80 ps, 360 ps, and 50%, respectively. τ_f is attributed to the free exciton decay, and τ_s is thought to be due to the boundexciton decay.

Information on the surface recombination is of great importance to many applications, e.g. light-emitting diode (LED) and electrochemical sensors etc. Hence, it is important to study the surface recombination of the NWs possessing large surface-to-volume (S/V) ratio. The surface recombination is characterized by two parameters, i.e. surface recombination velocity S and carrier diffusion length. The influence of the surface recombination velocity S on the decay time is determined by the diffusion equation with the proper boundary conditions. As for the ZnO NWs grown by the chemical bath deposition (CBD) method, the decay curves can be fitted by two exponential decays:

$$I(t)=A_S\, e^{-t/\tau_s}+A_B\, e^{-t/\tau_B} \qquad 3\text{-}1$$

where I(t) represents the PL intensity as a function of time, while A_S and A_B are the relative weights of the two exponential decays with time constants τ_s and τ_B, respectively. τ_B is the decay time constant of bulk materials. The deduced value for time constant τ_s and the ratio of A_S/A_B are summarized in figure 3-2c and d. The decay lifetime is influenced by the surface recombination velocity when combined with the carrier diffusion length, resulting in a direct correlation with the size of the nanorod. The value of τ_s increases and the ratio of A_S/A_B decreases after the thermal treatment. This fact is consistent with an improvement of the surface properties after the thermal treatment, since the CBD grown ZnO NWs at low growth temperature (93 ^{o}C) is expected to have various chemicals attached to the surface. The mild thermal treatment will release the chemicals from the NW surfaces without changing the defect density inside the NWs.

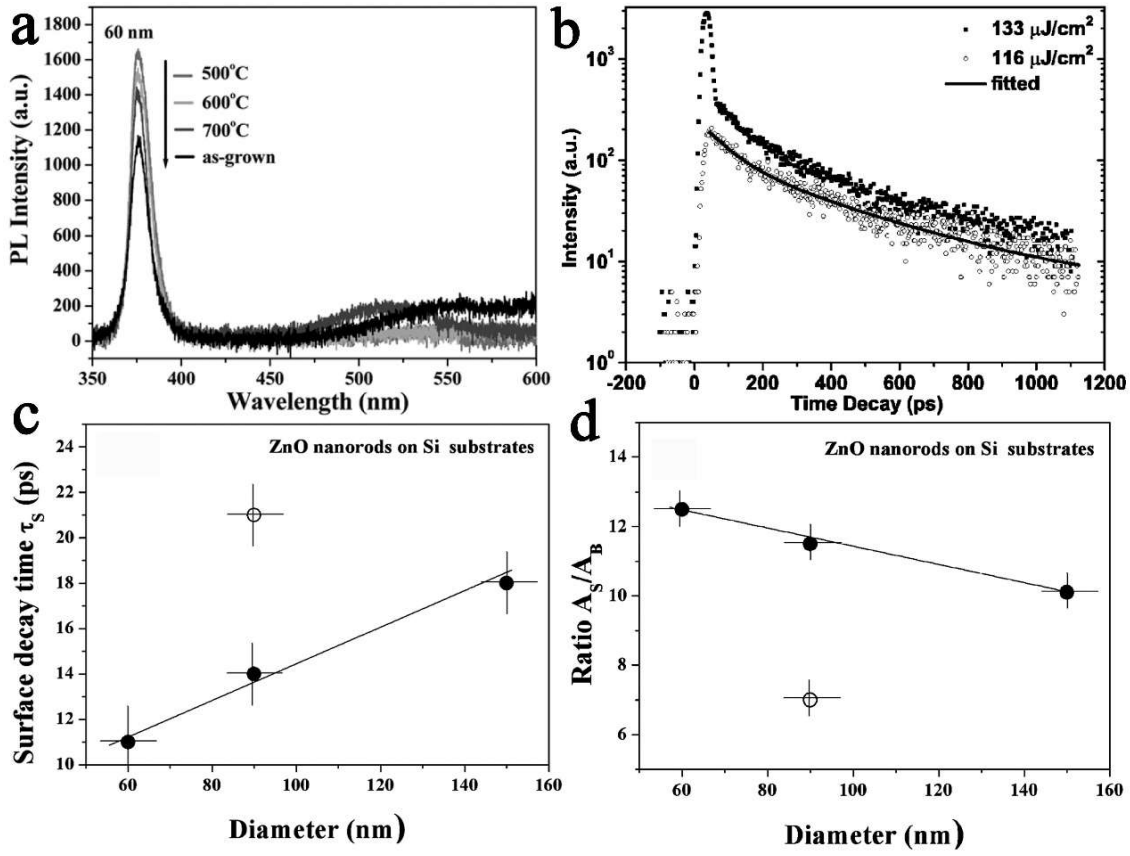

Figure 3-2. (a) PL spectrum of the ZnO NWs with different annealed temperatures.[154] (b) Time-resolved PL spectrum detected at 383 nm from the ZnO nanorod arrays at two excitation fluencies.[155] (c) The deduced surface recombination time τ_s. (d) The deduced ratio As /A_B versus diameter of the CBD grown ZnO NWs according to Eq.3-1. The corresponding data deduced from the annealed NWs (open circles) are also included for comparison.[154] (Figures are taken from[154, 155])

Another useful technique for studying the defect levels is the deep-level transient spectroscopy (DLTS), although the defect identity has not been conclusively established. This technique is applicable to not only thin-film but also single crystal samples.

Hall effect shows information regarding the concentration, mobility and the thermal activation energy of the free carriers in the system[156]. The validity of the analytical model and results is verified by the Hall measurements in the 5.3 section of this thesis.

Due to extreme complexity of the ZnO NW defects, it is necessary to use two or more techniques. Therefore, the combined analysis technique with the XRD, XPS, TEM, PL, CPL and CTRPLS etc. is a useful and comprehensive strategy to study the nanostructures. Understanding on the theoretical aspects of the defects in the ZnO NWs, methodology of the controlled defect creation in this system and proper choice of the characterization techniques, can meet the challenge of purposeful defects management in the ZnO NWs.

3.2 Investigation of the correlation between the structural parameters and properties of ZnO NWs

ZnO NW with a wide direct bandgap, high carrier mobility and non-central symmetric crystal structure is widely utilized in the optoelectronic and light harvesting,[13, 143, 157] piezoelectric, [8, 145] photo-catalysts,[158, 159] sensor,[8, 160] and energy storage devices[138, 161]. In these applications, defects and doping play an important role. Therefore, investigation of them become more and more imperative for optimizing the performance of the ZnO NW-based devices.

3.2.1 The action of defects: the optical and electrical applications of ZnO NWs

Like any other semiconductors, deep levels can affect the optical and electrical properties of the ZnO NWs. For example, the native or artificially induced defects are reported to severely degrade the potential barrier height and ideality factor of the metal-ZnO Schottky diodes, which acts as a conducting path for the charge carriers.

Figure 3-3A shows the morphological, optical, and electrical characterization of the individual ZnO NWs.[162] The results prove that the green emission and the carrier behaviors are related to the oxygen deficiencies. Photoluminescence and photoconductivity measurements of single crystal ZnO NWs show defect-related deep electronic states giving rise to green-red absorption and emission as reported by Z.Y. Fan et al.[163] Moreover, due to a slower oxygen

chemisorption process, the current decay time is significantly prolonged and the photoconductivity of the ZnO NWs is strongly polarized which is dependent on the incident light.

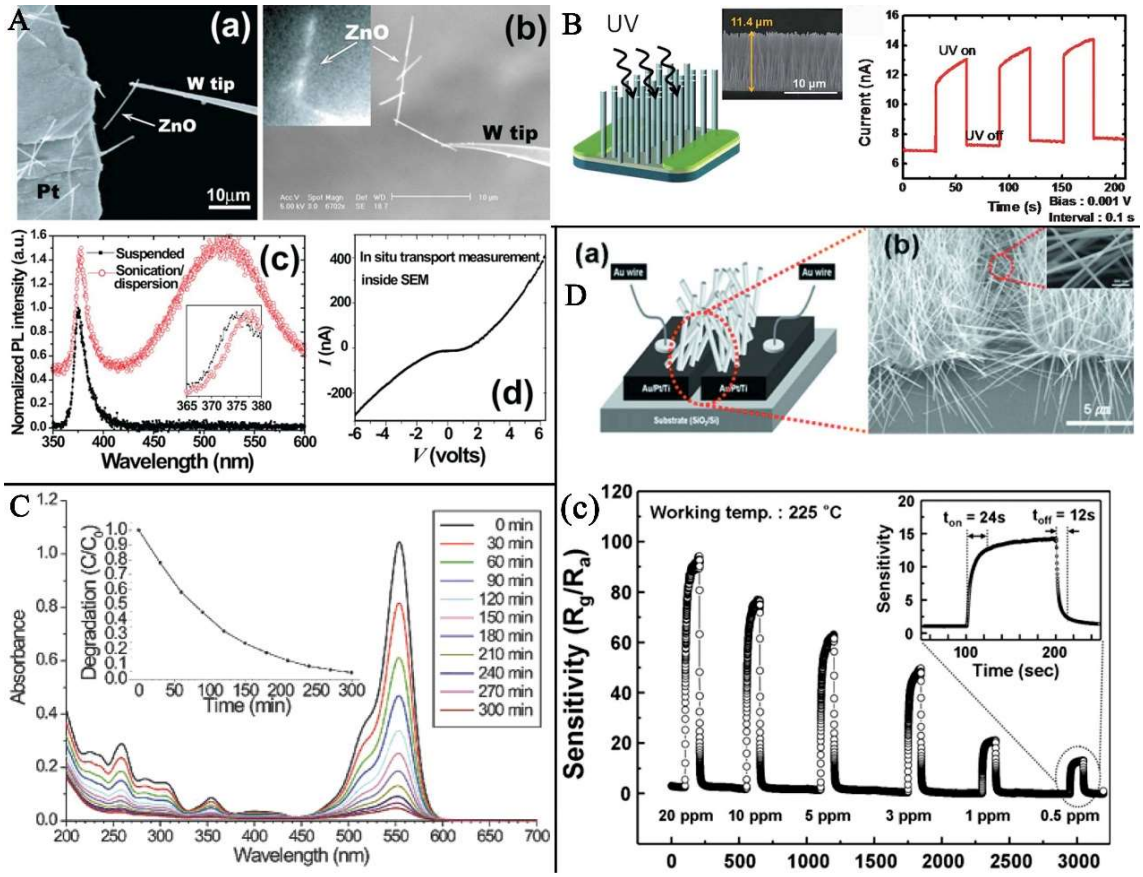

Figure 3-3. (Aa) SEM image illustrating the preparation of the suspended individual NWs. (Ab) SEM and optical (inset) images showing the same chain of the ZnO NWs glued to a W tip. (Ac) Micro-PL spectra of an individual ZnO NW (~50 nm) with the as-grown suspended and processed by the sonication/dispersion procedure, respectively. (Ad) A typical two-terminal I-V curve of the individual suspended ZnO NWs.[162] (B) Schematic illustration and SEM image of an aligned ZnO NWs array photodetector. Time-dependent photocurrent response of a ZnO NWs photodetector (at 365 nm UV-Vis with 1 mV bias).[164] (C) UV-Vis absorption spectra of rhodamine B corresponding to the irradiation time, respectively. Insets show the degradation value (C/C_0) with respect to

the irradiation time.[159] (Da) A schematic illustration and (Db) SEM images for the network-structured ZnO NW on the Si substrate. (Dc) Gas sensitivity curves of the ZnO NW gas sensor under exposure to the different concentrations of the NO_2 gas.[165] (Figures are redrawn from [159, 162, 164, 165])

Figure 3-3B [164] shows that the photo-responsivity measurements between a single ZnO NW and ZnO NW array devices. The ultrafast reset time are obtained in the ZnO NW array devices with a low bias. Since a very low bias effectively reduce the energy barrier of hole-trapping leading to easier migration of the hole. Thus, the highly sensitive photodetector with a low external electric field is attributed to the lower energy barrier of hole-trapping. These results offer an effective method to enhance the sensitivity of the ZnO nanostructure photodetector. Ultralong ZnO NWs which perform as effective and recyclable photocatalysts exhibit excellent photocatalytic activity under natural sunlight in figure 3-3C [159] where similar results were studied by Yu-Cheng Chang[158].

In the photochemical reaction process, the surface oxygen deficiencies acted as electron capture centers may be beneficial to their photocatalytic activity, which can be used to enhance the photocatalytic activity of the ZnO NWs by reducing the recombination rate of the electrons and holes.

In addition, owing to the electrons transfer between the ZnO surface and target gas molecules, such as O_2, H_2, CO, NO_2, and H_2S etc. the gas sensing can be measured by monitoring the changes in the surface electrical conductance of ZnO upon exposure to the gases.[8, 84, 165-168] Several works have indicated that the electrical response can be significantly improved in the ZnO NWs by controlling their structural parameters, such as morphologies, particle sizes, doping, and defects.[8, 84, 166] For example, M-W. Ahn[165] has reported that the effect of the oxygen-vacancy-related defects on the NO_2-sensing properties of the ZnO NWs. It displays fast response and recovery behavior with a maximum sensitivity to the NO_2 gas at 225 °C.

The reason is ascribed to V_o which act as preferential adsorption sites for the NO_2 molecules. Similar results have been explained by Wei An et al. using the density functional theory.[168] The results show that the adsorption energy (E_{ad}) of NO_2 on the oxygen-vacancy site is significantly increased to E_{ad} = -0.98 eV, which is three times larger than E_{ad} = -0.30 eV on the perfect site, This means that charge transfer from the oxygen-vacancy site to the NO_2 adsorbate is much larger than that from the perfect site to the NO_2 adsorbate. Meanwhile, V_o bind more tightly with the NO_2 molecules, thus attracting more charges from the ZnO surface as compared with the free oxygen vacancy on the ZnO surface, which is in good agreement with the close relationship between the concentration of the oxygen-vacancy-related defects and NO_2 sensitivity of the ZnO gas sensor.

3.2.2 The action of doping: the optical and electrical applications of ZnO NWs

Introducing impurities into an extremely pure intrinsic semiconductor (doping) is an important strategy in optimizing the optical and electrical properties of the ZnO nanostructures.[3, 12, 88, 131, 169] Fox example, the presence of copper in ZnO NWs could induce red-shift to lower energy[170] when the copper ions replace the zinc ions in the lattice parameters of the wurtzite hexagonal ZnO NW. These results show it is of great importance for further studies on the bandgap engineering of ZnO by doping, like color-tunable LED. Figure 3-5a, b and c clearly show a shift towards the violet wavelength range of the excitonic electroluminescence (EL) spectra from the Cu-doped ZnO device. This point is of interest for the efficient extraction of light from the devices.

Figure 3-4d and e show that the In-doped ZnO NWs (#3) exhibit better photocatalytic performance than the undoped NWs (#1).[90]. The reasons are that high concentration of the shallow Indium donors results in high concentration of the free electrons, which will significantly reduce the width of the surface depletion region. The narrowing of the surface

depletion region, would facilitate the electrons to transport to the surface, and enhance the photocatalytic performance.

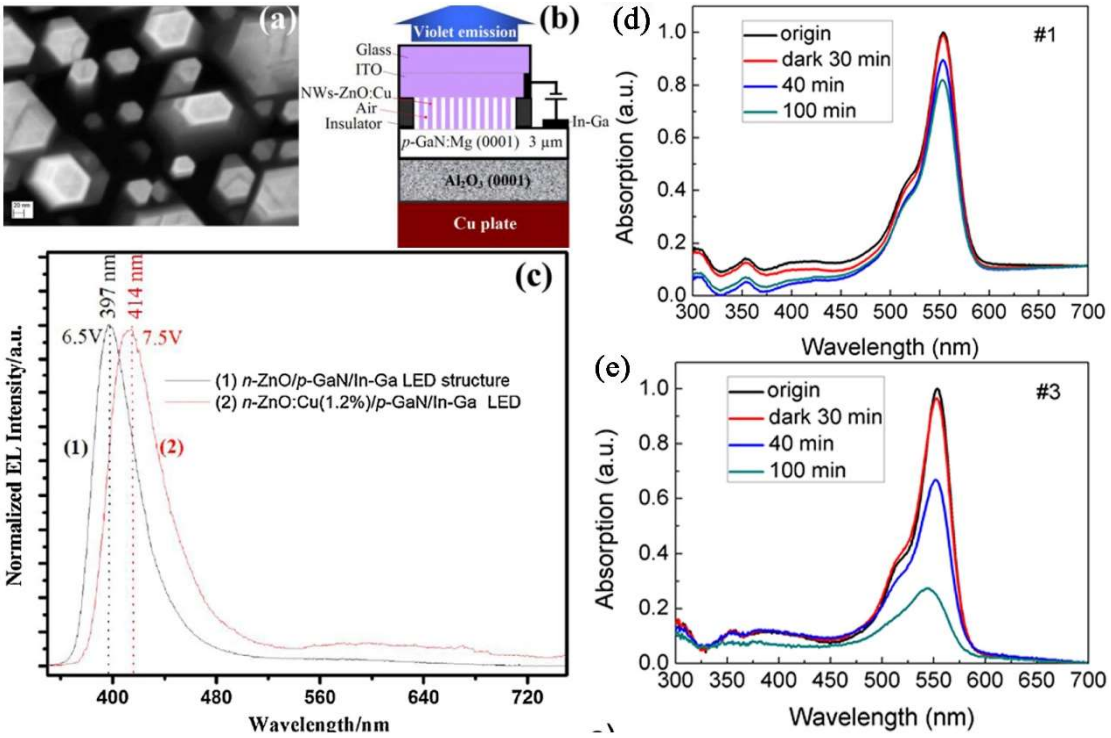

Figure 3-4. (a) SEM image of the Cu-doped n-ZnO NWs (1.2%) grown on p-GaN:Mg; (b) LED device structure; (c) electroluminescence spectra of the n-ZnO/p-GaN:Mg and n-ZnO:Cu (1.2%)/p-GaN:Mg NWs heterostructured LEDs at room-temperature under the forward bias of 6.5 and 7.5V, respectively.[170] UV-Vis absorption spectral variations of the RhB solution corresponding to (d) un-doped and (e) In-doped ZnO NWs.[90] (Figures are redrawn from[90, 170])

Khalid Mahmood and Seung Bin Park reported[92] that the N doping induced an increase of the carrier concentration and a decrease of the mobility, and thus the electrical resistivity is decreased. Figure 3-5b show that the current-voltage behavior of the devices with the ZnO and NZO nanorods demonstrates that annealing bring about 100-fold intensification in the current response for the ZnO and NZO nanorods due to the formation of oxygen vacancies

after the thermal treatment. The important point is that the current response of the NZO nanorods is still superior to that of the ZnO nanorod before and after the thermal treatment.

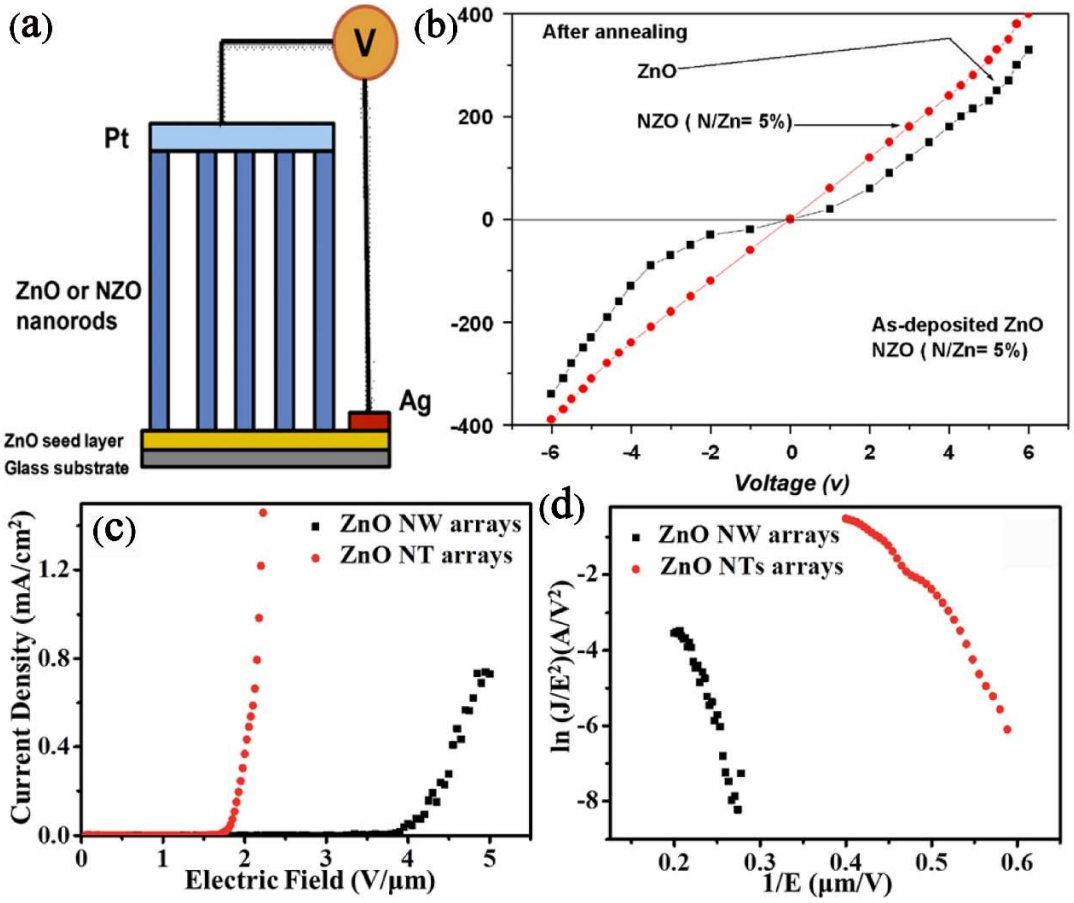

Figure 3-5. (a) The design of the ZnO and NZO nanorod arrays device; (b) The current–voltage curve for the ZnO and the NZO (N/Zn molar ratio of 5%) after annealing. (c) J-E characteristics of ZnO NWs and Ni-doped ZnO nanotowers. (d) Corresponding F-N plots. (Figures are redrawn from [88, 92])

In field emission, as shown figure 3-5c and d,[88] the Ni-doped ZnO nanotower arrays exhibit lower density and sharper tip, which results in the higher field enhancement factor and lower turn-on and threshold field as compared with the NWs (the turn-on and threshold field, and field-enhancement factor are 1.53V/μm, 1.88V/μm, and 2852, respectively).

3.3 The action of the structural parameters: the properties of ZnO field emission

Field emitters (ZnO) with nano-sized diameters, such as NWs[4, 137], nanosheets[5] and nanotetrapods [138, 141] have demonstrated higher emission efficiency than those with the micro-sized diameters or film field emitters. However, it is not enough for the field emitters. Deep investigation to dig much more advantages for the properties of field emission is urgently required to proceed.

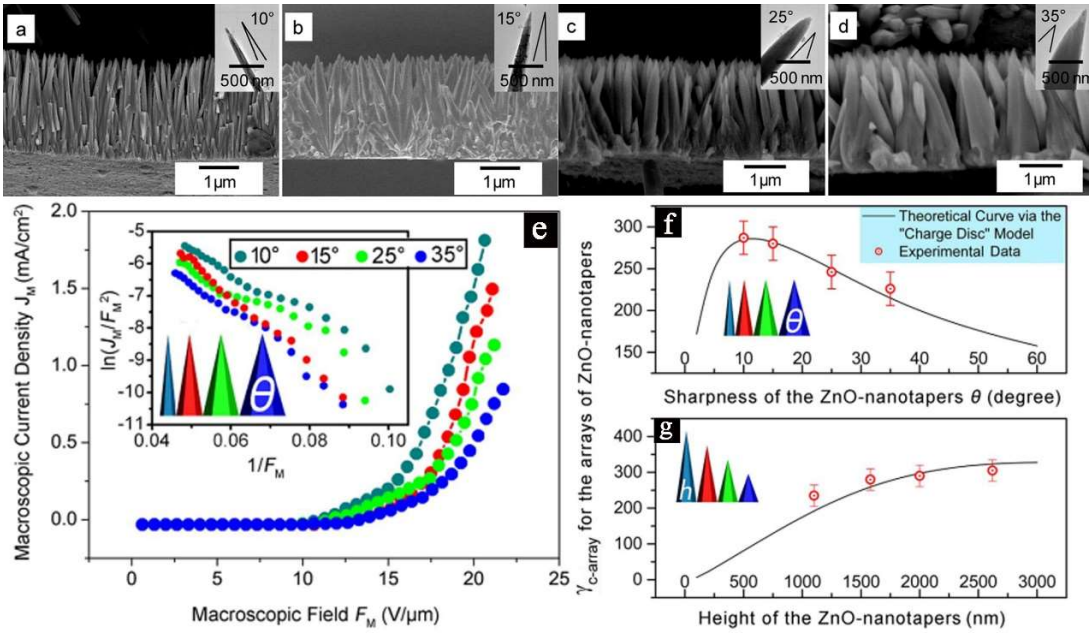

Figure 3-6.[3] Arrays of the ZnO nanotapers with the same height and different sharpness degrees (a to d) with corresponding to the TEM images, respectively. (e) J_M-F_M curves for the arrays of the ZnO nanotapers with the same height of 2 μm and different θ (10°, 15°, 25° and 35°). (f) $\gamma_{C\text{-array}}$ for the ZnO nanotapers arrays with different θ (upper) and height (lower), respectively. Error bars show the deviation of experimental accuracy. (Figures are redrawn from[3])

Zhuo Zhang et al.[3] has reported that large-area arrays of vertically aligned ZnO nanotapers with tailored taper angle. The sharpness (different angles: θ), height of the ZnO nanotapers and shielding effect as well as relationships among them are necessary parameters in the

properties of field emission. When the height of the nanotaper arrays is about 2 μm, the correlation between the sharpness and the shielding effect is as follows. When $0^o<\theta<16^o$ the shielding effect is stronger and dominant; when $\theta\approx16^o$, the shielding effect and the emission are nearly balanced; when $16^o<\theta<60^o$, the shielding effect is relatively weaker and decreases faster than that of the emission; when$\theta\geq60^o$, the shielding effect almost disappears and the emission decreases slowly. The results show that the field emission performance of the nanotaper arrays has improved with the increase of the sharpness (15°) at the height of ~2 μm in figure 3-6. Therefore, it is clearly demonstrated that how the sharpness to the top of 1D ZnO nanostructures can optimize FE properties.

Moreover, it is well known that the ZnO structural and internal lattice defects can impact on the field emission properties. Figure 3-7a, b, and c.[131] show that the lattice defects of the ZnO NW (stacking faults “W” and nano-sized fault areas “F” with the oxygen-deficient) using the TEM investigation with the aid of simulations. Nano-sized fault areas (region “F” in figure 3-7a), which are several nanometer, are observed around several stacking faults. The contrast of the HRTEM image in the fault areas is distinct from that in the wurtzite structure (region “W” in figure 3-7a). Also, the difference between them is clearly shown in their fast-Fourier transformed (FFT) diffractograms as indicated by the arrow in figure 3-7ab and ac. Figure 3-7b also demonstrates different lattice spacing using a line scan across region “F”. The corresponding simulation (figure 3-7c) is also in agreement with the experimental HRTEM images (region “W”) in figure 3-7a. The observed nano-sized fault area (region “F”) can be formed in the oxygen-deficient ZnO NWs (the ratio of O/Zn = 0). In addition, the F-N plots consist of two parts linearity as shown in figure 3-7d. The reasons are that the first emission from the electrons captured in the defect states is dominant in the lower electric field range; the second from the electrons near the Fermi level is the high electric field range. The former emission process is easier than the latter and is strongly dependent on the amount of defects.

While the latter emission process becomes dominant in the higher electric field ranges, resulting in a drop in the F-N plots as indicated by the arrow in the F-N plots of the ZNO2 in figure 3-7d.

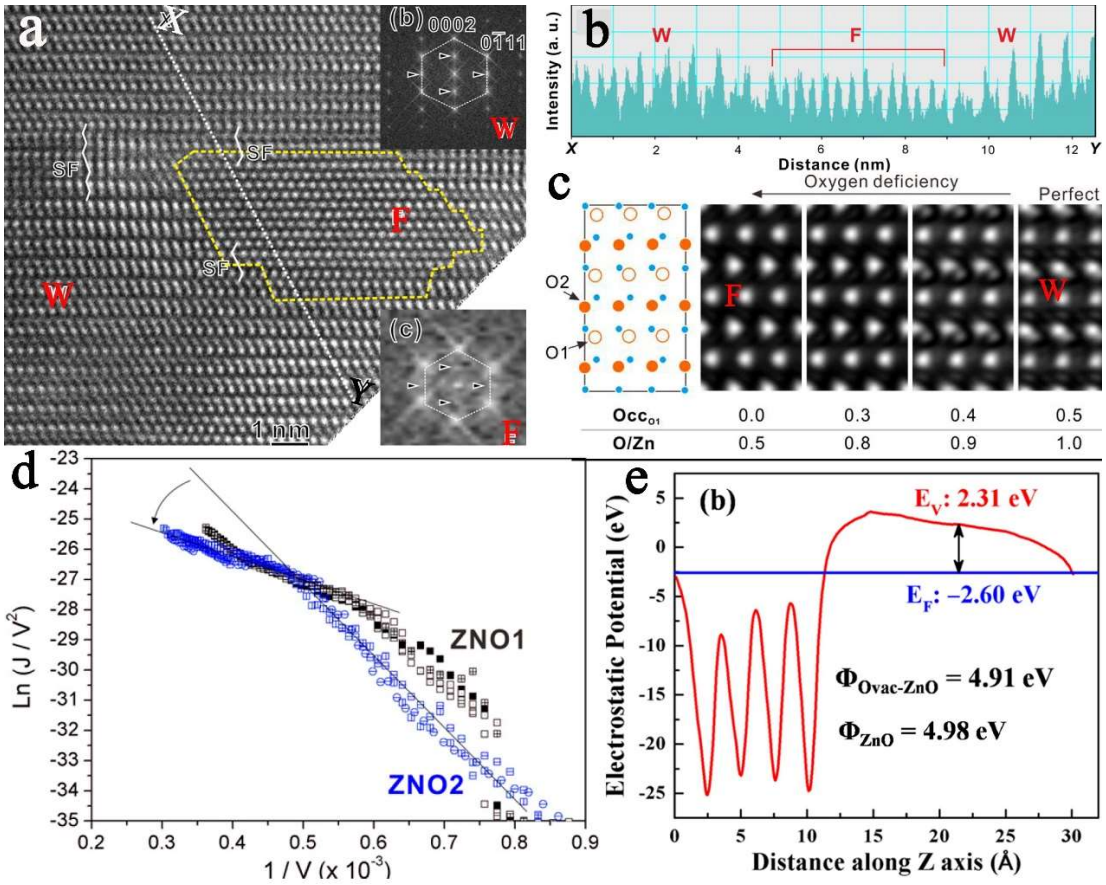

Figure 3-7. (a) HRTEM image of the stacking faults and nano-sized fault area; FFT diffractograms obtained from (ab) prefect area (region "W") and (ac) faulted area (region "F") in (aa); (b) Histogram of a line scan (X-Y) across region "F". (c) HRTEM simulation of the oxygen-deficient ZnO at a defocus of -400 Å and a thickness of 200 Å along [2$\bar{1}\bar{1}$0] direction according to the occupancy (Occ$_{O1}$) of oxygen site O1. (d) F-N plots of the ZnO NWs.[131] (e) Ovac-ZnO (0001)[171] (Figures are redrawn from [131, 171])

In addition, the presence of oxygen vacancies in the ZnO nanostructures (Ovac-ZnO) can improve the FE characteristics via lowering tunneling barrier i.e., reducing the work function (from 4.98 eV to 4.91eV) by shifting the Fermi level towards vacuum in figure 3-7e.[171] E_F

and E_V correspond to energy of the Fermi and vacuum level, respectively. Φ denotes the work function of the defined surface. Due to the vacancies, metal clusters of the unsaturated Zn atoms are trying to keep stable in the place of the point defects, which leads to an increase in the electron density around that vacancy sites (interaction increases). Therefore, the ZnO NWs with oxygen defects can show better FE characteristics.

Apart from the morphologies, doping and lattice defects, external conditions are also important factors for enhancing the field emission performance, e.g. the effect of x-ray irradiation on the optical, structural and field emission properties of ZnO NWs. With increase of the irradiation dose, the surface roughness with nano-protrusions is significantly increased, which are beneficial for achieving a larger field enhancement factor (β).[136]

In a word, the structural parameters (sizes, defects, and doping)[3, 91, 131, 140] of the ZnO NWs play an important role to alter the optical and electronic properties. Therefore, knowledge of the correlation and inter-relationship between the amount and type of the native intrinsic defects or doping present in the NWs as their size varies is an important step towards optimizing and tuning the performances of ZnO nanostructure-based devices.

4 Experiments and instrumentations

All experiments and methods throughout this thesis were performed and carried out according to the procedures described in this section. All the samples are fabricated using the CVD and hydrothermal solution. The microstructure and composition of the samples were investigated by the field emission scanning electron microscopy (FE-SEM), transmission electron microscopy (TEM), energy-dispersive X-ray spectroscopy (EDX), and X-ray photoelectron spectroscopy (XPS). The samples characterization and measurement were conducted with the ultraviolet-visible spectroscopy (UV-Vis), photoluminescence (PL), confocal photoluminescence (CPL), confocal time-resolved photoluminescence spectroscopy (CTRPLS), conductive atomic force microscopy (CAFM), Hall measurement system, and field emission system.

4.1 Synthesis methods of ZnO nanostrcures

4.1.1 Chemical vapor deposition

Chemical vapor deposition (CVD) technology is particularly interesting not only because it gives rise to high-quality nanostructures, but also because it is applicable to large-scale production.[110] This technique is widely used in the fabrication of 1D, 2D and 3D nanomaterials, such as wire-like and leaf-like ZnO.

4.1.2 CVD method for ultralong ZnO NWs

ZnO NWs were synthesized via a classical CVD process in a single-zone horizontal tube furnace. All chemical reagents were analytical grade and used without further purification. The n-Si (100) substrate with very low resistivity value of 0.006 to 0.008 Ωcm was first washed with absolute alcohol (99.7%) and then with acetone (99.5%) in an ultrasonic bath. Then it was etched in a mixed solution of 20 mL of ammonia hydroxide (25%), 20 mL of H_2O_2 (30%), and 100 mL of deionized water at 80 ^oC. An alcoholic solution of zinc acetate dehydrate (0.02 M) was spin-coated 5 to 7 times on the substrate followed by annealing in an

oven at 120 ºC for half an hour. This simple spin-coating method was used to obtain a film of ZnO crystal seed layers instead of the relatively costly deposition coating. The source material for the CVD was pure ZnO powder (0.5 g, 99.0%) mixed with graphite (0.5 g, 99.85%). After grinding, the mixtures were spread in an alumina boat which was placed at the center of the furnace tube. The substrate covered with a film of ZnO seed layers was placed above the source material and the distance between them was about 2-5 mm. Subsequently, 70 sccm (standard cubic centimeters per minute) of argon gas and 2 sccm of oxygen gas were introduced into the reactor and the pressure in the tube was adjusted to 200 mbar. The temperature was heated up to 950 ºC at a rate of 25 ºC/min and this temperature was held constant for 5 to 60 mins. After reaction, the furnace was cooled naturally to room temperature.

4.1.3 CVD method for leaf-like In-doped ZnO nanostructures

Leaf-like structures were prepared by a carbon thermal reduction process without any catalyst. After grinding, 0.45 g of ZnO (purity, 99.999%), 0.05 g of In_2O_3 (purity,> 99%), and 0.5 g of fine graphite powder were dispersed in a quartz boat placed in an alumina tube (length is 150 cm and inner diameter is 58 mm) at the center of the furnace. Silicon substrates (100) were washed by alcohol and acetone in an ultrasonic bath for half an hour, respectively, and then were located down-stream from the source (3 to 5 mm) in the quartz boat. Argon (80 sccm) and 2.5 sccm of oxygen were introduced into the chamber, and the system was pumped to a pressure of 400 mbar. Then the furnace temperature was set to ramp up to 950 °C at 25°C/min and kept for 5 to 30 mins under the same flow of mixed gas and vacuum condition. Finally, the system was naturally cooled to room temperature, and a film of light-yellow products on the substrates was prepared.

4.1.4 Hydrothermal method for ZnO NWs

An alcoholic solution of zinc acetate (0.02 M) was spin-coated 5 to 7 times on the cleaned Si substrate, followed by annealing in air at 120 ºC for 30 minutes. ZnO seed layers are thus formed on the substrate for the subsequent growth of the ZnO NWs. 1.85 g of zinc nitrate hexahydrate ($Zn(NO_3)_2 \cdot 6H_2O$, 98%) and 0.87 g of hexamethylenetetramine (HMTA, $C_6H_{12}N_4$, 98%) were dissolved into 250 mL of deionized water. Subsequently, the Si substrate with the ZnO seed layers was immersed (with the seed layers facing down) in the aqueous solution at 85 ºC for 3 h. Finally, the substrate was removed from the aqueous solution, rinsed with distilled water for several times, and dried at room temperature.

4.1.5 Hydrothermal method for needle-like ZnO NWs

The needle-like ZnO nanostructures were prepared by a modified low-temperature solution method. Zinc nitrate hexahydrate ($Zn(NO_3)_2 \cdot 6H_2O$, 98%, 1.85g) and 0.87 g of hexamethylenetetramine ($C_6H_{12}N_4$, 98%) were dissolved in 250 mL of deionized water under vigorous magnetic stirring. After a couple of minutes, ethylenediaminetetraacetic acid (EDTA)-2Na (1.16 g) and sodium citrate (0.91 g) were also put into the solution. Finally, the Si substrate coated with ZnO NWs (section 4.1.2) was immersed upside-down in the solution and heated at 80°C for 3 h. After that, the top part of the ZnO NWs were etched and evolved into needle-like structure.

4.2 Characterization and analysis for ZnO nanostructures

4.2.1 Analysis for intrinsic defects in size-controlled ZnO NWs

A combined experimental approach is investigated to understand the important role of the native intrinsic defects in influencing the properties of the ZnO NWs. Such as XPS and EDX measurements are utilized to study the chemical state and composition of the ZnO NWs and understand the important function of certain native defects such as oxygen vacancies (V_o) and

zinc interstitials (Zn_i). On the other hand, the optical characterizations of the NWs are performed with confocal photoluminescence (CPL) and confocal time-resolved photoluminescence spectroscopy (CTRPLS) which is a contactless method for understanding the dynamics of the carriers involved in optical processes. PL intensities and radiative lifetimes are investigated the concentration of native intrinsic defects and their spatial location on and beneath the surface of the NWs with different S/V ratios and lengths. CAFM is a viable method for obtaining the current-voltage (I-V) characteristics of the ZnO NWs. Hence by considering the conduction mechanism of the reverse biased I-V characteristics in the NWs, an analytical equation (with the use of Pàde approximations) is derived for obtaining the donor concentration of the ZnO NWs with different lengths directly from its corresponding I-V characteristics.

4.2.2 Field emission analysis of ZnO nanostructures

The FE properties of ZnO nanostructures (ultralong NWs, needle-like NWs and In-doped leaf-like nanostructure) are studied via field emission system, such as turn-on field, threshold field and the field-enhancement factors (β).

4.3 Analysis instruments

4.3.1 Field emission scanning electron microscopy (FESEM)

Field emission (FE) is the emission of electrons from the surface of a conductor caused by a strong electric field.[123] An extremely thin and sharp tungsten needle (tip diameter 10-100 nm) works as a cathode. The FE source reasonably combines with scanning electron microscopes (SEMs) whose development has been supported by advances in secondary electron detector technology. The acceleration voltage between the cathode and anode is common in the order of magnitude of 0.5 to 30 kV, and the apparatus requires an extreme vacuum (~10^{-6} Pa) in the column of the microscope. Because the electron beam produced by

the FE source is about 1000 times smaller than that in a standard microscope with a thermal electron gun, the image quality will be markedly improved. Therefore, the FE scanning electron microscope (FESEM) is a very useful tool for high resolution surface characteristic in the fields of nanomaterials.[172] The Nova Nano SEM™ 230 scanning electron microscope has a high resolution imaging with up to 30 kV, which delivers best in class imaging and analytical performance for this dissertation samples.

4.3.2 Energy-dispersive X-ray spectroscopy (EDX)

Energy-dispersive X-ray spectroscopy (EDX) is an analytical technique used for the elemental analysis and chemical characterization of a sample.[173] It relies on an interaction of some source of X-ray excitation and the sample. The fundamental principle is that each element has a unique atomic structure allowing unique set of peaks on its X-ray emission spectrum. Therefore, X-ray spectra can be used to collect and analyze, yielding quantitative elemental information from the sample. The EDX detector is equipped on the Nova Nano SEM™ 230 scanning electron microscope.

4.3.3 Transmission electron microscopy (TEM)

TEM is a microscopy technique in which a beam of electrons is transmitted through an ultra-thin sample, interacting with the specimen. TEM image is formed from the interaction of the electrons transmitted through the specimen and then magnified and focused on an imaging device.[174] The high-resolution TEM (HRTEM) images are taken with a JEOL JEM-2010 F microscope (JEOL, Japan) at an acceleration voltage of 200 kV. The HRTEM specimens are prepared by drop casting the sample dispersion onto a carbon-coated 300-mesh copper grid and are dried under room temperature.

4.3.4 X-ray powder diffraction (XRD)

X-ray powder diffraction (XRD) is a rapid analytical technique mainly used for phase identification of a crystalline material. In this thesis, XRD patterns were obtained using a D/MAX-2550 diffractometer (Rigaku, Tokyo, Japan) equipped with a rotating anode and a CuK a radiation source (λ= 1.54178 Å).

4.3.5 X-ray photoelectron spectroscopy (XPS)

XPS is a surface-sensitive quantitative spectroscopic technique that measures the elemental composition, chemical state and electronic state of the elements.[175] The sample is illuminated from the surface with x-rays-monochromatic or unfiltered Al Kα or Mg Kα-and photoelectrons. XPS spectra are obtained by irradiating a material with a beam of X-rays. The position and intensity of the peaks in an energy spectrum provide the desired chemical state and quantitative information. The surface chemical compositions of the samples in this thesis were analyzed by a PHI-5000C ESCA system with Mg Kα x-ray radiation source (where $h\upsilon$ = 1253.6 eV).

4.3.6 Photoluminescence (PL)

Photoluminescence is light emission from any form of matter after the absorption of photons (electromagnetic radiation).[176] It is one of many forms of luminescence (light emission) and is initiated by photoexcitation (excitation by photons). PL performance of the samples in this thesis was investigated by Hitachi F-7000 Fluorescence Spectrophotometer.

4.3.7 Ultraviolet-visible spectroscopy (UV-Vis)

UV-Vis refers to absorption spectroscopy or reflectance spectroscopy in the ultraviolet-visible spectral region, which means it uses light in the visible and adjacent (near-UV-Vis and near-infrared) ranges.[177] This technique is complementary to fluorescence spectroscopy,

in which fluorescence deals with transitions from the excited state to the ground state, while absorption measures transitions from the ground state to the excited state.

4.3.8 Confocal photoluminescence (CPL) and confocal time-resolved photoluminescence spectroscopy (CTRPLS)

Confocal microscopy is an optical imaging technique for increasing optical resolution and contrast of a micrograph by means of adding a spatial pinhole placed at the confocal plane of the lens to eliminate out-of-focus light.[178] This technique is popularly applied in life sciences, semiconductor inspection and material science. In this thesis, the CPL intensity mapping on the submicrometre scale and temporal decay of CPL were performed using a PicoQuant MicroTime 200 confocal microscope. CPL measurements were carried out at room temperature and the luminescence of the ZnO NWs samples was excited with a pulsed diode laser at 375 nm and at a constant intensity.

Time-resolved spectroscopy is the study of dynamic processes in materials or chemical compounds by means of spectroscopic techniques.[179] Most often, processes are studied after the illumination of a material occurs, but in principle, the technique can be applied to any process that leads to a change in properties of a material. With the help of pulsed lasers, it is possible to study processes that occur on time scales as short as 10^{-16} seconds.

4.3.9 Conductive atomic force microscopy (CAFM)

CAFM is a variation of atomic force microscopy (AFM) and scanning tunneling microscopy (STM), which uses electrical current to construct the surface profile of a sample.[180] The current is flowing through the metal-coated tip of the microscope and the conducting sample. Usual AFM topography, obtained by vibrating the tip, is acquired simultaneously with the current. This enables to correlate a spatial feature on the sample with its conductivity. CAFM microscope uses conventional silicon tips coated with a metal or

metallic alloy, for example, Pt-Ir alloy. In this thesis, the I-V measurements on the ZnO NWs were conducted using a Veeco DI 3100 multimode scanning probe system (SPM) with conductivity measurement capability.

4.3.10 Hall measurement system

The Hall measurements on the ZnO NWs arrays were carried out at room temperature by using the Van der Pauw four probe technique with a square configuration utilizing an Accent HL5500 system. The process of electrodes fabrication was that a thin aluminum (Al) foil (same size as the ZnO NWs arrays sample) with a circular hole (radius is about 0.1 cm) very close to each of the four corners was used as a mask, for the subsequent physical vapour deposition of a mixture of gold-zinc (Au-Zn) powder for the formation of the Au-Zn electrodes on top of the ZnO NWs arrays. After the Au-Zn alloy electrodes were deposited at the four corners of the ZnO NWs arrays sample, the Al foil was removed where the sample area consisting of the ZnO NWs arrays is about 1 x 1 cm^2 and the area of each Au-Zn electrode is about 0.03 cm^2. Subsequently, annealing of the ZnO NWs arrays sample with the four Au-Zn electrodes was performed in nitrogen gas at the temperature of 500 ^oC for 1 minute. This annealing step was performed as the Au-Zn contacts would become ohmic with a low resistivity value when annealed at 500 ^oC in nitrogen ambient.[181] Moreover, good ohmic contacts between the electrodes and the ZnO NWs were confirmed before the Hall measurements. Therefore the carrier concentration obtained from the Hall measurements refers to the ensembles of as-synthesized ZnO NWs arrays which is assumed to be the same for each individual ZnO NW.

4.3.11 Field emission system.

FE measurements of the as-prepared samples were carried out in a conventional parallel-plate field emission configuration (self-supported) with an anode-to-sample spacing of

approximately 150 μm (using glass fibers as spacers for all tests) under a vacuum of 5×10^{-5} Pa.

5 Results and discussions

The properties and performance of the ZnO nanostructures based devices are intimately related to the structural parameters (size, defect and doping).[15-17, 182-186] However, there are few profound studies about the correlation between the native intrinsic defects distribution and the size-dependent ZnO NWs (length and surface-to-volume (S/V) ratio). In addition, due to the extreme complex defects in the ZnO NW, it is necessary to simultaneously investigate them using two or more techniques, for example, the combined spectroscopic techniques including XRD, XPS, UV-Vis, PL, CAFM, CPL, and CTPRLS. This comparative analysis and understanding of these aspects would be helpful to understand the function of defects and doping in the ZnO NWs.

In this section, the combined spectroscopic techniques are used to systematically understand the important role of the native intrinsic defects for adjusting the properties of the ZnO NWs. For example, the applications of the field emission with different ZnO nanostructures (ultralong NW, needle-like NW and leaf-like In-doped ZnO) are investigated (the details are shown as following).

In section 5.1, ZnO NWs with different lengths and sizes are synthesized by both the aqueous solution method and the CVD process. The length and corresponding surface-to-volume (S/V) ratio of the ZnO NW on the concentration and variation of the different types of the native intrinsic defects in the ZnO NWs as well as the correlations between them are investigated via the combined spectroscopic techniques. XRD, Raman, XPS and EDX measurements show that the surfaces of the longest ZnO NWs with a low S/V ratio possess the highest concentration of V_o or Zn_i.

In section 5.2, the room-temperature CPL are used to investigate the spatial distribution of the shallow and deep V_o concentrations on the polar (0001) and non-polar ($10\bar{1}0$) surfaces of ZnO NWs. The green emission at different spatial locations on the ZnO NW polar (0001) and non-

polar $(10\bar{1}0)$ surfaces is found to have maximum intensity near the NW edges, and the intensity decreases from the edges to the center of NW. In addition, understanding the dynamics of the carriers involved in the optical processes are implemented by the CPL and CTRPLS, such as the temporal information on the recombination lifetime as well as the optical emissions at specific wavelengths of the intrinsic defects in the different S/V ratios and lengths of the ZnO NWs. With the length of the ZnO NWs increasing, the corresponding decreasing S/V ratio could lead to a decrease (slowing) of the scattering rate of the excitons with the surface of ZnO NWs, and increase the radiative lifetime due to some surface recombination processes.

In section 5.3, the conductive atomic force microscopy (CAFM) is a method to obtain the current-voltage (I-V) characteristics of the ZnO NWs. Hence, considering the conduction mechanism of the reverse biased I-V characteristics in the NWs, an analytical equation (with the use of Padé approximations) is derived for obtaining the donor concentration of the ZnO NWs with different lengths directly from their corresponding I-V characteristics. The validity of the analytical model is verified by the Hall measurements and the donor concentration is positively correlated with the increase in the concentration of V_o and Zn_i.

Field emission (FE) properties with different ZnO nanoostructures, including the ultralong NW, needle-like NW and In-doped leak-like ZnO are measured in the section 5.4. The different enhanced parameters of the FE properties are discussed, such as high aspect ratios, defects, and indium incorporation. Finally, the leaf-like In-doped ZnO nanostructures are suitable for a field emitter in the microelectronic devices, which can be ascribed to the lowest turn-on and threshold field as well as its relatively high β value.

5.1 Investigation of assorted analytical techniques for ZnO NWs (defects)

5.1.1 Background

The performance of the 1D ZnO NWs arrays based devices are intimately related to morphologies and the native intrinsic defects or artificially incorporated defects which can optimize the optical and electrical properties of the semiconductor.[15, 17, 18, 182, 187-189] Here, ZnO NWs with different lengths and sizes are synthesized via the CVD process and aqueous solution method. Due to the extreme complexity of the ZnO defect structures, it is always necessary to use two or more techniques simultaneously for investigation, for example, XRD, Raman, EDX, and XPS. XPS and EDX measurements are utilized to study the chemical state and composition of the ZnO NWs and understand the important function of certain native defects. The V_o defects are not only spatially located on the surface of the NW but an increasing concentration of the V_o defects ascribed to the green emission is also located in the annulus region beneath the surface for the longer NWs as compared to the shorter NWs due to the decreasing (surface-to-volume) S/V ratio for the longer NWs. The increase/decrease of the various parameters due to the incorporation of the intrinsic defects is related to the increase/decrease in the S/V ratio of the synthesized NWs. Corresponding results could possibly provide a deeper understanding of the relationships between the defects and size changes in the ZnO NWs.

5.1.2 Morphologies

As shown in figure 5-1, the SEM images showing the side view of the as-synthesized ZnO NWs with different lengths. The length of the vertical ZnO NWs is around 2 μm (Figure5-1a) and 150 μm (Figure 5-1d) as prepared by the solution method and CVD process for 20 minutes, respectively. Figure 1e and f show the typical 45^o tilted view of SEM image showing the morphology of the as-prepared vertical ZnO NWs by the aqueous solution method and the

CVD process, respectively. It was visibly observed that the ZnO NWs grown by the two methods are dense and the height of the NWs in the array is rather uniformly long. Moreover, these NWs in figure 5-1a to -1d also are uniformly distributed on the surface of the Si substrate where most of the NWs are vertically quasi-aligned with an inclination towards the Si surface.

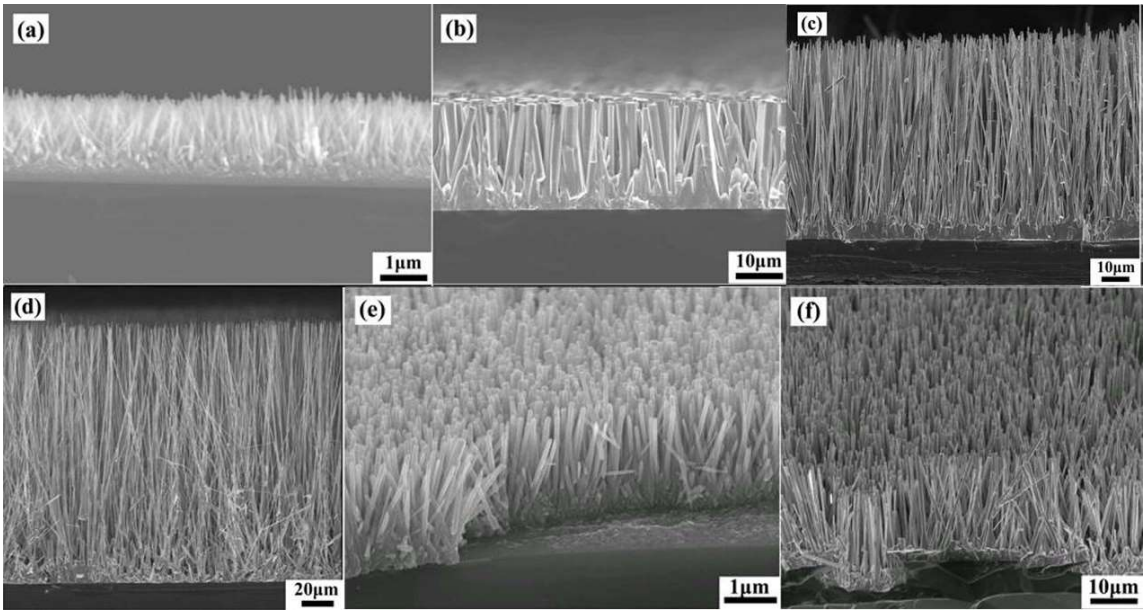

Figure 5-1. Side view of the ZnO NWs with different lengths (a) aqueous solution method. CVD process for (b) 5 min, (c) 11 min and (d) 20 min. The typical 45° tilted view SEM image showing the distribution of the NWs prepared by the (e) aqueous solution method and by the (f) CVD process.

For a better examination of the surface morphology of the ZnO NWs, the close-up, higher magnification top view SEM images of the vertical ZnO NWs in the four samples are displayed in figure 5-2. From the images, it can be deduced that the shape of the NWs is hexagonal and the diameter of the solution prepared NWs is an average value of 100 nm while the diameter of the CVD prepared NWs is larger in the range of hundreds of nm or in the micrometre range. The average NW diameter of the four samples is around 100 nm, 500 nm, 1 µm and 1.5 µm named as sample A, B, C and D, respectively.

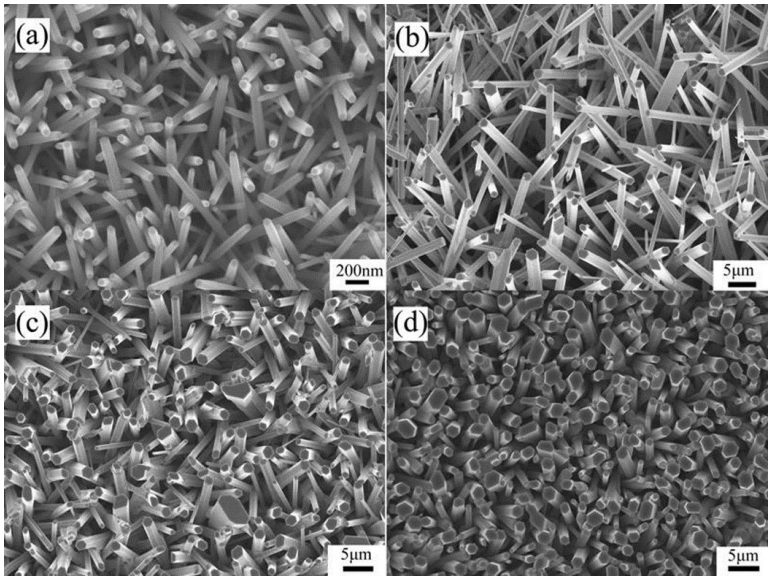

Figure 5-2. Typical top view SEM image of the vertical ZnO NWs in sample (a) A, (b) B, (c) C and (d) D.

Figure 5-2 also shows that the reaction growth time can affect the diameter of the ZnO NWs during the CVD process. With increasing reaction time, the ZnO NWs can grow in both the vertical (c-axis direction) and radial direction. Hence, this may lead to more NWs in sample D having a slightly larger diameter with a small resultant increase in the average diameter of the NWs. However, it must be stressed that the length of the NW increased at a much faster rate as compared to the small increase of the diameter by comparing Figure 5-1 and 5-2.

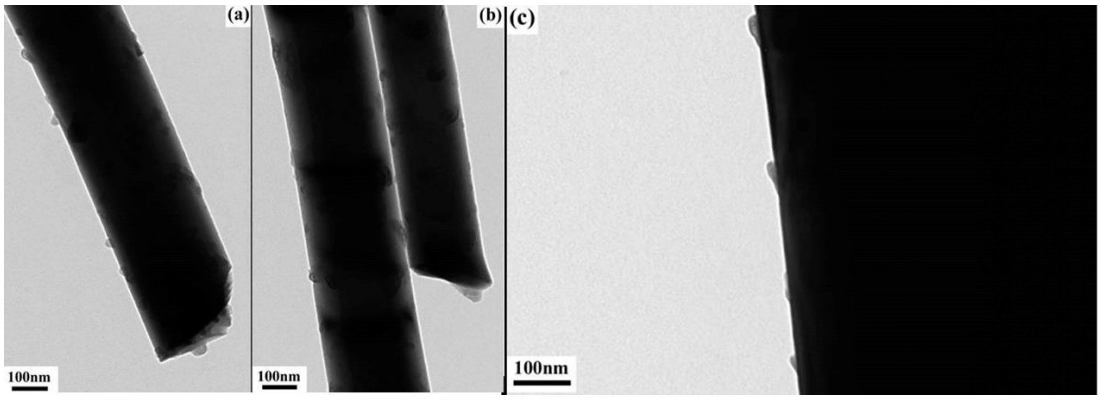

Figure 5-3. TEM images of the ZnO NWs in sample (a) B, (b) A and (c) D.

In addition, Figure 5-3 shows the TEM images with the diameter of a single NW from sample B (Figure 5-3a) is about 350 nm which is in good agreement with the SEM image in figure 5-2b. The importance information from TEM images show a rough surface morphology which suggests the presence of a high density of surface states.

5.1.3 XRD analysis

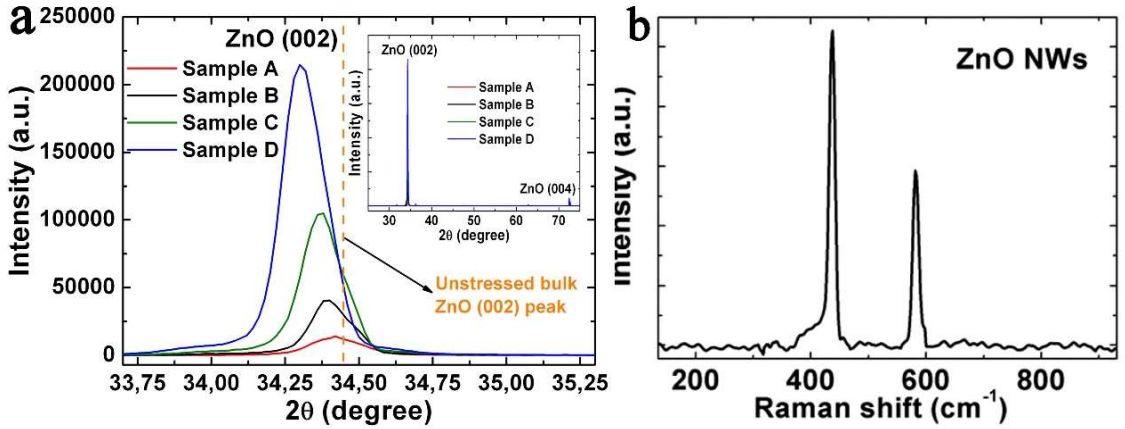

Figure 5-4. (a) XRD pattern of the ZnO NWs in the four samples A to D. The inset shows the spectra over a wider range of 2θ. (b) Raman spectrum of the ZnO NW arrays (Sample D).

To obtain samples structure information, x-ray diffraction has been investigated the crystalline quality of the ZnO NWs. The inset in figure 5-4a shows the XRD pattern for the as-prepared ZnO NWs arrays in all the four samples. There are being only two diffraction peaks where the peak of the stronger diffraction corresponds to the plane (002) and the weaker diffraction peak to the (004) plane. In the XRD pattern, the strongest peak corresponding to the (002) plane may indicate a preferential growth orientation of the ZnO NWs along the [0001] direction.

In addition, from the longest ZnO NWs arrays (sample D), the angular position of the ZnO (002) peak is located at 2θ =34.29° while it shifts towards 2θ = 34.40° for the shortest ZnO NWs (sample A). This implies that there is some relaxation of the residual stress in the crystal

lattice of the shortest NWs as the (002) peak for unstressed bulk ZnO is located at 2θ =34.44°.[190] The origin of the main component of the residual stress has been attributed to the intrinsic stress due to the presence of intrinsic point defects (e.g. V_o, Zn_i) incorporated in the crystal lattice during the growth process and has been shown to be compressive in nature.[191, 192] The other component of the residual stress is attributed to the thermal stress due to the difference in the thermal expansion coefficient of ZnO ($4.75\chi10^{-6}K^{-1}$) and the Si substrate ($2.60\chi10^{-6}K^{-1}$), however it is much smaller in magnitude as compared to the intrinsic stress.[193] This shift of the ZnO (002) peak towards smaller values of 2θ = 34.30° (away from 2θ= 34.44°) for the NWs in sample D implies that the longer ZnO NWs contain a higher concentration of zinc interstitials or oxygen vacancies. This could be possibly due to a larger incorporation of the zinc atoms into the NWs during the longer synthesis time required for the NWs using the CVD process hence leading to a higher concentration of Zn_i and compressive stress stemming from them.[192]

5.1.4 Raman spectra analysis

Raman spectra have been used to identify the crystal orientation of wurtzite ZnO NWs.[194] ZnO belongs to the C_{6v} symmetry group, and from group theory prediction the optical modes at the C point of the Brillion zone are given by $\Gamma = A_1+B_2+ E_1+E_2$.[195] The A_1 and E_1 modes represent the vibration of atoms parallel and perpendicular to the hexagonal c-axis, respectively. They are both infrared and Raman-active, which further divided into longitudinal optical (LO) and transverse optical (TO) components. The Raman peak at 331 cm^{-1} is assigned to the A_1 (acoustic overtone). The low and high frequencies of the E_2 mode (E_2 (low), E_2 (high)) are exclusively Raman-active and correspond to the vibration of the Zn and O sublattice, respectively. The B_1 modes, however, are silent and inactive. Importantly, it is experimentally observed that the presence of both the A_1 (acoustic overtone) and A_1 (TO)

bands centered at 331 and 380 cm^{-1}, respectively, is associated with the orientation of the ZnO nanostructure perpendicular to the c-axis, while the absence of both of these modes is associated with the orientation of the ZnO nanostructure parallel to the c-axis.[194] As shown in figure 5-4b, observing the Raman spectra of sample D, the negligible signal of both the A_1 (acoustic overtone) and A_1 (TO) bands indicates that ZnO NWs are oriented preferentially along the c-axis. This is in agreement with XRD spectrum, which confirms the ZnO NW growth along the c-axis. Raman spectra are also sensitive to the structural defects in the synthesized ZnO NWs, and the presence of the E_1 (LO) peak at around 582 cm^{-1} is associated with V_o defects.[196]

5.1.5 XPS analysis

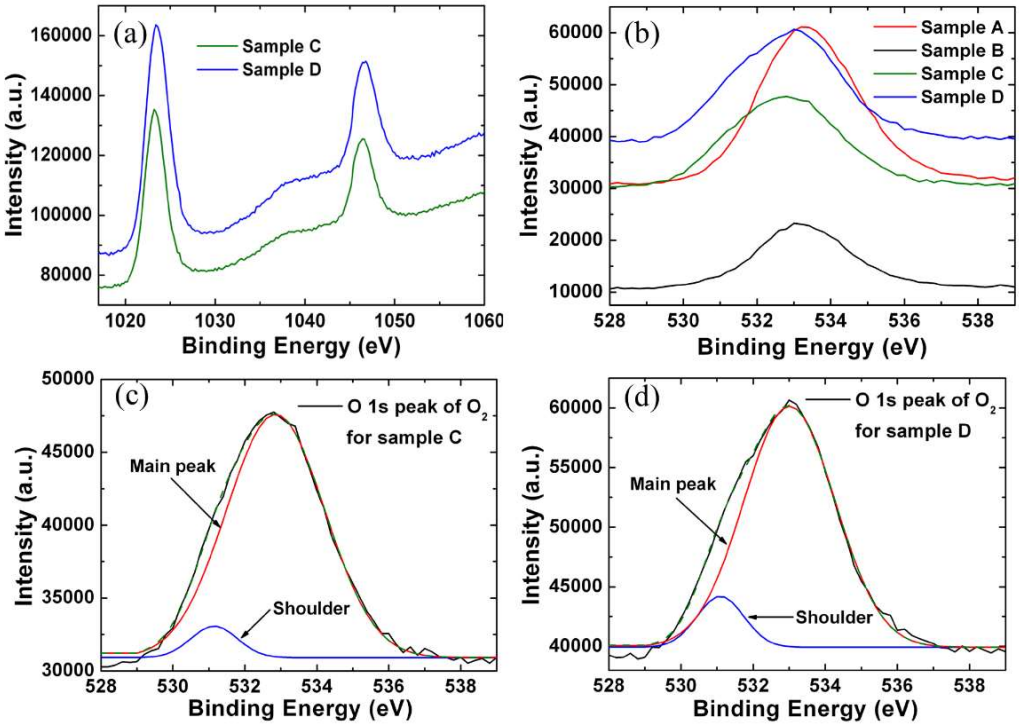

Figure 5-5 (a) XPS spectra of the Zn 2p peak. (b) XPS spectra of the oxygen 1s peak corresponding to the ZnO NWs in the four samples A to D. The fitting of the oxygen 1s peak by Gaussian functions corresponding to (c) sample C and (d) sample D, respectively.

To understand the surface chemical state of the synthesized ZnO NWs, XPS analysis is utilized. Figure 5-5a and 5b display the XPS spectra spectrum of the ZnO NWs from sample A to D, respectively. In figure 5-5a, the two peaks with Zn spectrum centered at 1022.7 and 1045.8 eV with a spin energy separation of 23.1 eV can be assigned to Zn $2p_{3/2}$ and Zn $2p_{1/2}$, respectively. To get further information for O 1s, Figure 5-5c and d show more details of the XPS high resolution spectra with samples C and D, respectively. The O 1s main peaks in sample C and D can be centered at 533.0 eV and a shoulder peaks centered at 531.2 eV after using a Gaussian fitting method. The lower binding energy component at around 531.2 eV has been attributed to oxygen deficiencies or vacancies within the ZnO matrix[197] whereas the higher binding energy component is probably due to some surface hydroxide species on the NWs.[150, 151] In addition, it is observed that the intensity of the shoulder peak O1s component at 531.2 eV is lower for sample C and the intensity of this component is related to the concentration of V_o.[197] On the other hand, Figure 5-5b shows the shift of the O 1s peak to higher energy for sample A which implies the increase of oxygen atoms on the surface of the NWs (reduction in the concentrations of V_o) prepared by the aqueous solution method.[150-152, 198] This indicates that the ZnO NWs prepared by the CVD process (samples B to D) contain more oxygen-deficient states as compared to sample A. Hence the analysis of the O 1s peak suggests that the surfaces of the longest ZnO NWs in sample D possess the highest concentration of oxygen vacancies.

5.1.6 The surface stoichiometry of ZnO NWs

From figure 5-1, -2, and -3 information, ZnO NWs can approximate as a cylinder and from a purely geometric viewpoint the surface to volume ratios of the NWs are given by：

$$\frac{S}{V} = \frac{2\pi r_{NW}^2 + 2\pi\, r_{NW} l_{NW}}{\pi\, r_{NW}^2 l_{NW}} = 2\left(\frac{1}{r_{NW}} + \frac{1}{l_{NW}}\right) \qquad 5\text{-}1$$

Where l_{NW} and r_{NW} is the average length and radius of the NW, respectively. From eqn. (5-1) and figure 5-1 and 5-2, it was seen that the S/V ratio of the synthesized NWs decreases from sample A to D. [The S/V ratio of the NWs taking into consideration the surface recombination layer of a finite thickness is given in ref.] [199] In addition, for a more quantitative analysis of the surface stoichiometry of the ZnO NWs to confirm the above observation, the relative ratio of Zn/O can be obtained using the XPS peak area of Zn and O and their elemental sensitivity factor given by, [200]

$$\frac{\mathrm{n(Zn)}}{\mathrm{n(O)}} = \frac{\mathrm{A(Zn)/S(Zn)}}{\mathrm{A(O)/S(O)}} \qquad 5\text{-}2$$

where n(Zn)and n(O) are the atomic numbers of the Zn and O elements, A(Zn) and A(O) are the areas under the Zn 2p and O 1s peaks and S(Zn) and S(O) are the elemental sensitivity factors of Zn and O at 4.8 and 0.66, respectively.[200]

Since the XPS spectroscopy can only probe up to about 10 nm beneath the surface of the NWs, while the X-ray in the energy-dispersive X-ray spectroscopy (EDX) measurements can penetrate to a deeper depth of about 1 to 2 μm, the bulk stoichiometry of the ZnO NWs could be obtained from the EDX measurements. Quantitative analysis of the results shows that the surface and bulk atomic ratios of Zn to O (Zn/O) corresponding to the 4 sets of samples (tabulated in Table 5-1) are all greater than unity and are likewise positively correlated with the increase in the length (and corresponding decrease of the S/V ratio) of the synthesized ZnO NWs. Hence the XPS and EDX analysis implies that there are oxygen deficiencies in the ZnO NWs and the native intrinsic defects vary distinctly with the length of the NWs (the same results have been previously observed in ref.[201, 202]). Conversely, as there is an easier formation of Zni due to dissociation under high temperature conditions,[203] the extended growth time for the longer NWs during the CVD process may have led to a surplus concentration of Zni incorporated in the NWs. The excess zinc atoms in the ZnO crystal

lattice become ionized and preferably diffuse and then accumulate at interstitial positions in the ZnO crystal lattice which results in an increase of interstitial Zn atoms and Zn_i defects as well as a decrease in the concentration of zinc vacancies, V_{Zn} (the concentration of V_{Zn} should be reduced in Zn rich conditions).[204] Therefore the concentration of the V_o jointly with Zn_i defects as well as the V_{Zn} defects increases and decreases, respectively, on the surface and in the bulk for the longer synthesized ZnO NWs.

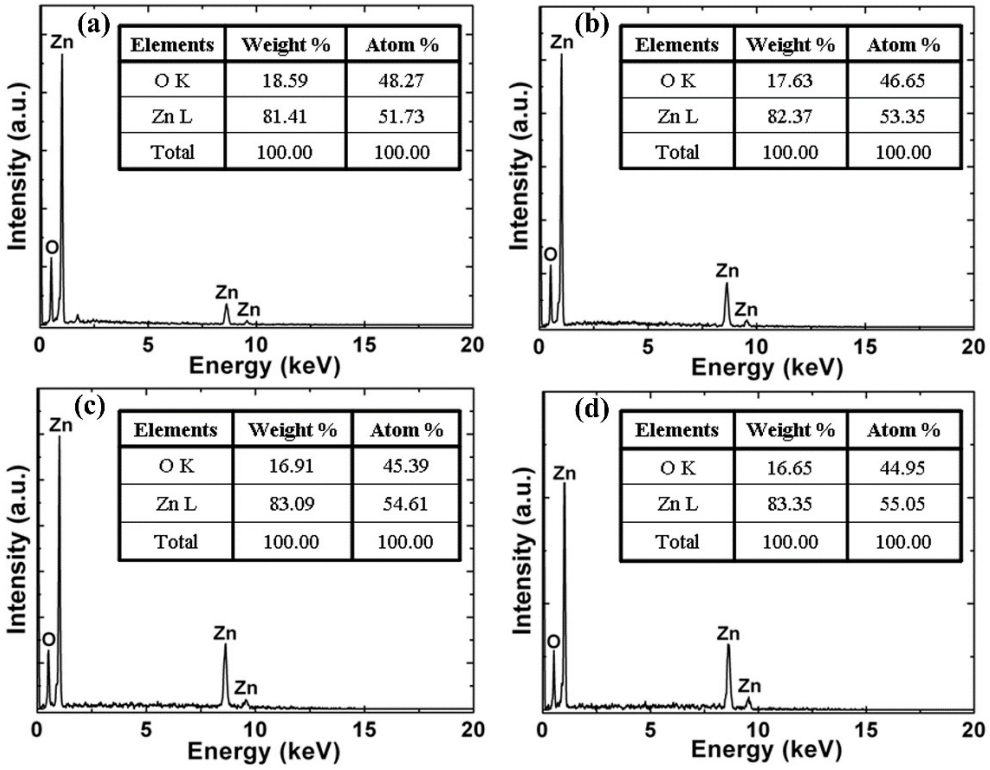

Figure 5-6. EDX spectra of the ZnO NWs in the sample (a) A, (b) B, (c) C and (d) D.

Table 5-1 Length, S/V ratio as calculated from eqn. (5-1) and the weight and atomic percentages of the zinc and oxygen elements from the analysis by EDX of the samples. The surface and bulk atomic ratios of Zn to O from the XPS and EDX measurements, respectively, are also included in the table.

Sample	Length /μm	S/V ratio /μm^{-1}	Element Zn wt%	Element O wt%	Element Zn atomic%	Element O atomic%	Surface Zn/O ratio from XPS	Bulk Zn/O ratio from EDX
A	2	21	81.41	18.59	51.73	48.27	1.06	1.07
B	20	4.1	82.37	17.63	53.35	46.65	1.12	1.14
C	68	2.03	83.09	16.91	54.61	45.39	1.19	1.20
D	150	1.35	83.35	16.65	55.05	44.95	1.24	1.22

5.2 Investigation of the assorted analytical and spectroscopic techniques for ZnO NWs (defects)

5.2.1 Background

It is well known that the surface and deep bulk of the ZnO nanostructures contain a large amount of intrinsic defects such as oxygen deficiencies or vacancies (V_o), which will influence their optical and electrical properties as well as their performance in device applications.[205, 206] Therefore, it is essential to investigate the distribution of the defects (such as V_o) in the size-dependent NWs to optimize the performance of the devices. Recently, though the effects of V_o on the optical and electrical properties of the bulk and nanoscale ZnO structures have been extensively investigated,[15, 17, 18, 56, 57, 182, 183, 187-189, 207, 208] the spatial distribution of the V_o concentration in size-dependent ZnO NWs surfaces has not yet been evaluated. Therefore, the spatial electronic profile of the surface and deep V_o concentrations in the size-dependent ZnO NWs are analyzed using the combined spectroscopic techniques in this section. In addition, the connection between the PL intensities and radiative lifetimes with the concentration of the native intrinsic defects and their spatial distribution on and beneath the surface of the NWs with different S/V ratios and lengths is investigated. Qualitative understanding of the spatial distribution of the surface defects in size-dependent NW are studied, which leads to a more efficient functionalization and integration of the ZnO NW-based devices for improved performance.

5.2.2 CPL and PL emission spectra for ZnO nanoostructures

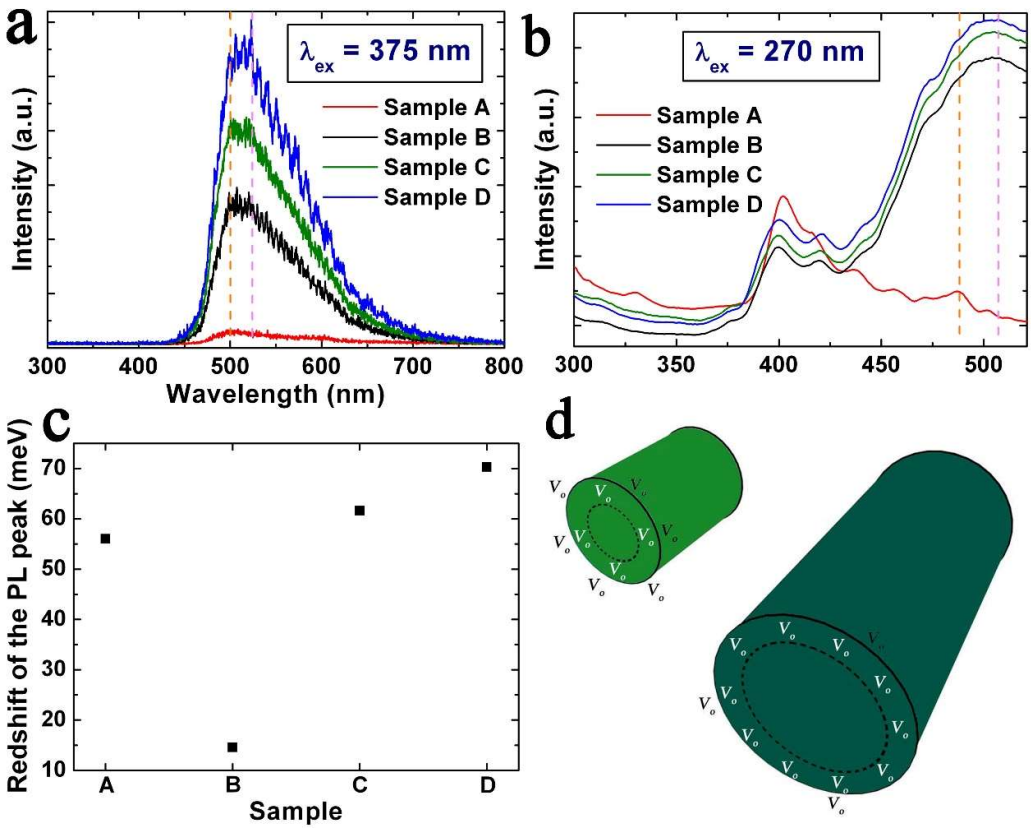

Figure 5-7 (a) CPL spectra obtained with a pulsed diode laser (λ_{ex} = 375 nm) and (b) PL spectra obtained with a Xe lamp (λ_{ex} = 270 nm) corresponding to the four samples A to D. (c) The redshift of the green band in meV between the PL and CPL spectra corresponding to the four samples with the change in the excitation wavelength from 270 nm to 375 nm. (d) Illustrative diagram which shows the different distribution of V_o defects on the surface and in the annulus region beneath the surface of the NW for ZnO NWs of different lengths and S/V ratios.

In Figs. 5-7b and a, PL spectrum show a smoother curve than the CPL spectra. Because the PL intensity represents an average value over a larger number of NWs, while the CPL intensity shows only individual NW over the excitation laser spot area, which increase the signal noise. On the other hand, the disappearance of the CPL band centered at 400 nm and

420 nm (figure5-7a) could be due to the cut-off filter used in the CPL measurements to remove the laser light where the filter also removes all emission between 400 nm and 420 nm. The room temperature CPL spectra of the NWs around the excitation spot for the 4 samples consist of a dominant green band centered at around 510 nm and an extremely weak and broad UV-Vis emission at 380 nm where the yellow-orange (590-640 nm) PL band usually ascribed to excess oxygen (oxygen interstitials)[209, 210] is not observed in the CPL spectrum as shown in figure5-7(a). The UV-Vis emission arises due to the band to band transition from the direct electron-hole pair recombination between the conduction and valence band.[210] In addition, the dominant visible PL band also suggests that there is a high concentration of surface defects and this is corroborated by the rough surface morphology observed in the TEM image, as shown in figure 5-3.

As for the CPL measurements, the lowest excitation wavelength λ_{ex} is 375 nm. By utilizing a xenon (Xe) lamp where the wavelength of excitation could be varied, ensembles of NWs in samples A to D could be excited at a lower wavelength (λ_{ex} =270 nm) for additional PL measurements. Figure 5-7(b) shows that two new PL bands centered at around 400 nm and 420 nm could be observed in the PL spectrum for sample A to D where the UV-Vis band at 380 nm is still very weak. Conversely, the luminescence peak at 400 nm has been suggested to be due to the recombination of free excitons through an exciton-exciton collision process[211] while the peak at 420 and 510 nm has been attributed to the interstitial Zn ions and V_o in the ZnO lattice, respectively.[211, 212] For instance, the increase of the PL intensity at 510 nm (in figure 5-7b) can be correlated to a higher concentration of V_o defects with the increase of the NW length from sample A to D, and this is in agreement with the results from the XPS and EDX measurements.

5.2.3 Redshift of the CPL and PL emission spectra in the size-controlled ZnO NWs

Under the same excitation wavelength of 375 nm in figure 5-7a, besides the difference in the relative intensity, the peak positions of the 4 peaks also exhibit a small red shift of about 23 nm (from about 499 nm to 522 nm) among themselves. This red-shift of 109 meV as observed in figure 5-7a suggests that the energy of the electronic transitions for the green PL emission is slightly reduced. Similarly, a redshift of the emission spectra is also observed in figure 5-7b for the four samples with excitation wavelength of 270 nm for PL spectrum. Generally, two mechanism which could account for the observed red shift are the variation of the oxygen-vacancy concentration in the NWs[213] or the build-up of generated internal stress due to the presence of intrinsic defects in the NWs, where it could lead to a reduction of the bandgap.[214] If the ZnO NW is approximated as a solid cylinder then from Lamé's equations, both the circumferential stress (hoop stress) and radial stress are constant throughout the interior of the NW.[215] Furthermore, since the amount of internal stress can lead to a narrowing of the bandgap,[214] if there is no significant shift of the energy levels of the deep level defects such as V_o with respect to the band edge, then the sample will respond optically by emitting at lower energy due to the narrowing of the bandgap. Although the amount of intrinsic residual stress in the NW is constant in an individual sample (from the above approximation), this residual stress level can change between samples. Some evidence in support of this is indicated in the XRD result in figure 5-4a which shows that there is some intrinsic residual stress present in the synthesized NWs due to the point defects. In addition, the amount of intrinsic residual stress is correlated with the concentration of intrinsic defects in the ZnO NWs (from figure 5-4a). For example, sample D possesses the largest amount of intrinsic residual stress (due to the largest concentration of intrinsic defects, figure 5-4a) displays the biggest red-shift in the green band PL as shown in figure5-7b. Hence, the redshift of the PL and CPL spectra in Figs. 5-7a and b, respectively, at the same excitation wavelength could be

probably due to the different constant level of intrinsic residual stress in the different samples. From the XRD analysis, the red-shift of the green CPL and PL emission spectra band between the different samples could be due to some bandgap narrowing effects as a result of the intrinsic stress in the NW from the incorporation of the native intrinsic defects in the NWs or could be due to the spatial variation of the V_o defects in the NWs.

From the above EDX, XPS, CPL and PL measurements, it is observed that sample A (synthesis by the hydrothermal method) contains a lower concentration of defects (e.g. V_o and Zn_i) as compared to samples B to D (synthesized by CVD method), resulting in the variation of the defect concentration in the ZnO NWs. Likewise, it has been observed that the size and corresponding S/V ratio increases and decreases, respectively, from sample A to D. Importantly, this is well correlated with the corresponding increase of the concentration of defects from sample A to D and hence I propose that a comparison of the subsequent results can also be made concurrently between the different samples according to the difference in their sizes or morphologies.

5.2.4 Variation of the concentration of V_o defects in the ZnO NW of different sizes and lengths

Although the nature of the defect responsible for the green emission is still not fully clear and many hypotheses have been proposed to explain the emission originating from intrinsic defects or impurities,[216] this emission, however, is typically and widely accepted to be associated with oxygen vacancies.[210, 217-219] However, there is still some uncertainty on the exact recombination model of the green emission involving the oxygen vacancies. In addition, density functional calculations have also shown that V_o is a deep donor and is also the dominant intrinsic defect under both Zn-rich and O-rich conditions.[220] From figure 5-7a and b, a good correlation is observed between the increase of the intensity of the observed green PL and CPL band with the increase of the NWs length (samples A to D) and consequently

with the increase of the V_o defects concentration from the XPS and EDX measurements. Such a trend has also been observed earlier by other researchers in this field.[219] On the other hand, the penetration depth of the excitation light (at 270 and 375 nm) used in the PL and CPL measurements is in the range of tens to hundreds of nm. For instance, the penetration depth of the excitation light at 325 nm for ZnO is about 60 to 120 nm.[221] Therefore, I believe that the defects responsible for the green luminescence in the ZnO NW samples might originate from the oxygen vacancies that are located not only on the NW surface but also in an annulus region in the NW beneath the ZnO NW surface (figure 5-7d). In support of this hypothesis, the decrease of the S/V ratio for the longer NWs indicates that there exist lesser surface states[218] per volume for the longer NWs. However, the increase of the green PL and CPL intensity correlates directly with the increase of the concentration of V_o (figure 5-7a and b) as the NWs elongate, which is in agreement with the XPS measurements. To reconcile these two observations, besides the V_o defects existing on the surface of the NW, it is also necessary that a larger portion of the total concentrations of the oxygen vacancies are located in an annulus region which is beneath the ZnO NW surface as the length of the NWs increases. This is substantiated by the quantitative analysis of the EDX measurements where the increasing bulk atomic Zn/O ratio in Table 5-1 implies that the concentration of the V_o defects beneath the surface of the NWs similarly increases as the NWs elongate.

Furthermore, this viewpoint is supported by the PL measurements in figure 5-7b where a shorter excitation wavelength (higher photon energy) is used for the measurements, which corresponds to a slightly deeper penetration depth in the samples. It is observed that at spatial locations deeper beneath the surface of the NWs, the increase of the green PL intensity (between 488 nm and 510 nm) is similarly correlated with the increase of the length of the NWs (and corresponding decrease of the S/V ratio). This signifies that V_o defects exist at a spatial location deeper in the NW and a higher concentration of V_o exists in the interior of the

longer NWs as compared to the shorter NWs (figure 5-7d). Hence from the results, I infer that a larger fraction of the oxygen vacancies should exist in an annulus region beneath the surface of the synthesized NW as its length and S/V ratio increases and decreases, respectively.

5.2.5 The concentration of V_o defects spatial distribution at the (0001) surface of ZnO NWs

To investigate the spatial distribution of V_o of ZnO NWs, I choose sample D for an investigation with the confocal microscopy. Figure 5-8a shows the scanned images which map the CPL emission intensity from the ZnO NWs obtained using a Pico Quant Micro Time 200 confocal microscope. These images are obtained by scanning an area of 16.8×17.1μm. Most of the ZnO NWs are hexagonal-shaped with a diameter of 2-3 μm. This is quite similar to the NW shapes and sizes observed in the SEM image of the figure 5-2d. In addition, due to the difference in the NW heights, where the NWs with a distinct emission intensity outline in the focal plane, the spatially resolved CPL emission intensity of the ZnO NWs is inhomogeneously distributed. This could be the case, in confocal microscopy, because light emitted above or below the focal plane is not complete efficiently collected. Also, the NWs with weaker emission intensity are longer or shorter. The SEM image (figure 5-2d) shows that the (0001) surface of the NW is relatively flat. Therefore, it is worth pointing out that for the (0001) surface of one NW, the variation of the CPL intensity at the surface is not significantly affected by the presence of other NWs in its vicinity.

To clearly understand the spatial of distribution of V_o, I set different locations on the (0001) surface on the top of some of the NWs as shown in the figure 5-8a. This is indicated by the slanted blue guide lines on the Zn-terminated (0001) surface on some of the NWs in the figure 5-8a. The spatial variation of the spectral intensity along each of the blue lines on the top of the ZnO NW [i.e. (0001) surface] in figure 5-8a is plotted in figure 5-8b. To visualize the various spatial locations along the blue line on the (0001) surface of the ZnO NW, the

midpoint between the center of the two innermost spots where the excitation laser beam hits is taken as the origin (d=0 μm) and the spatial distances of the center of each of the six lateral spots, d_x (where x = 1, 2, 3, 4, 5, and 6, in the inset) are calculated from this origin point. For example, the distances from the origin of the center of the two innermost locations where the excitation laser beam hits are indicated as d_3 and d_4. It is worth pointing out that there are slight variations in the peak values at d_x (where x = 1, 2, 3, 4, 5, and 6, in the inset) for each of the four different NWs because the origin point for each blue line is located at a different spot on the (0001) plane as shown in 4 different ZnO NWs in figure 5-8a. The six spatial locations along each of the blue lines represent the confocal volumes of the CPL measurements that are taken along the top (0001) cross-section of the NW like the inset.

In figure 5-8b, each CPL spectrum plotted is obtained at different spatial locations [d_x (where x = 1, 2, 3, 4, 5, and 6), in the inset] on the top (0001) surface of a ZnO NW. The magnitude of the green luminescence peak in each individual CPL spectra at a particular location on the (0001) surface of the ZnO NW can be correlated with the concentration of V_o at that particular spatial location. Furthermore, the shape and peak position of each green luminescence peak at each spatial location remain essentially the same ($\lambda \approx 519$ nm),[219] which reinforces the viewpoint that the magnitude of each CPL peak at $\lambda \approx 519$ nm can be used as a measure of the amount of oxygen vacancies at that particular spatial location. The overall CPL spectra are a function of different spatial locations on the top (0001) surface of the ZnO NW and, in other words, are dependent upon the different spatial locations from which the emission occurred. However, the magnitude of each individual CPL spectra shown in figure 5-8b is a function of the emission from a specific spatial location and, because ZnO luminescence is very sensitive to the surface state of ZnO,[219] the green PL peak at $\lambda \approx 519$ nm can therefore be correlated to the amount of V_o at that spatial location.

Therefore, changes in the maxima of the CPL spectra at different spatial locations along the blue lines in figure 5-8a are therefore most likely due to variation in the spatial distribution of V_o defects. It is visible that the emission intensity of CPL spectra gradually reduce from the edge to the center on the top surface of ZnO as shown in the CPL spectrum in figure 5-8b.

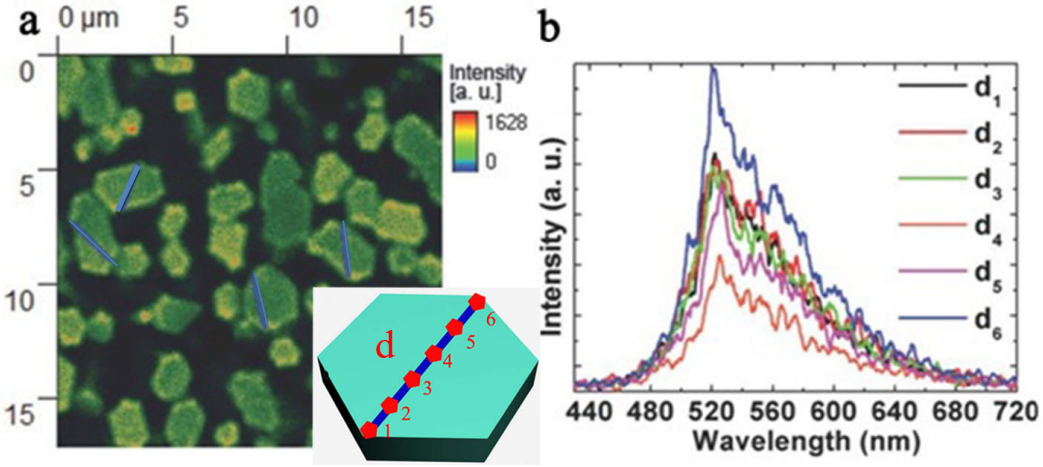

Figure. 5-8. (a) Spatially resolved CPL intensity microscope image of the ZnO NWs. The blue lines represent locations where the CPL spectra are taken at different spatial locations. (b) Plot of several CPL spectra of the green luminescence taken at different spatial locations d_x (where x = 1, 2, 3, 4, 5, and 6, in the inset) along the blue guide line across the top cross sectional surface (0001) of one laterally elongated ZnO NW.

5.2.6 The concentration of V_o defects spatial distribution at the $(10\bar{1}0)$ surface of the ZnO NWs

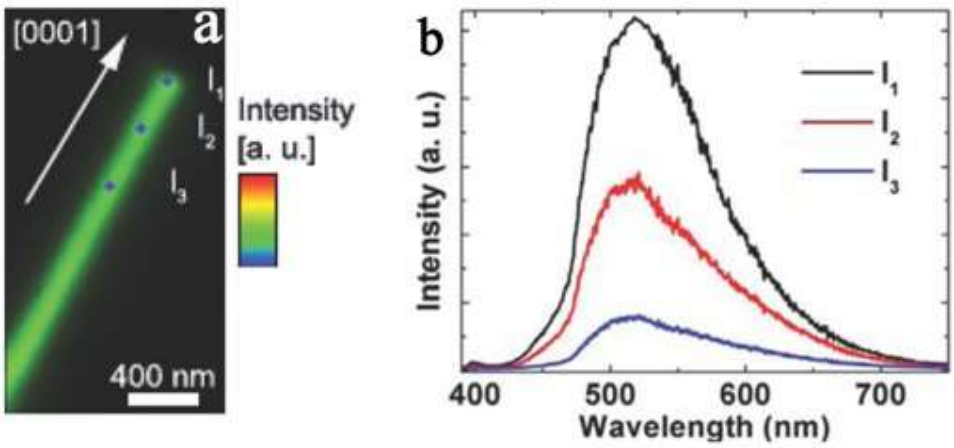

Figure 5-9. (a) CPL intensity microscope image of a thin ZnO NW lying on its side along the [0001] direction. (b) The CPL spectra at three different spatial locations along the [0001] direction, which corresponds to a NW that is lying on its side.

Figure 5-9a shows the CPL emission intensity of an individual thin ZnO NW lying on a side composed of the $(10\bar{1}0)$ surface along the [0001] direction (i.e. the c-axis). The spatial location of the center of the three spots where the measurements are taken, I_x (where x= 1, 2, 3), is calculated in relation to the slanted top edge where the (0001) and $(10\bar{1}0)$ surfaces meet each other (located near the upper right corner of the NW in the figure 5-9a). The CPL spectra taken at these three positions are along a path parallel to the wurtzite c-axis. This corresponds to a vertical cross section of the $(10\bar{1}0)$ surface along the [0001] growth direction of the NW that is lying on its side, as shown in figure 5-9a. Figure 5-9b shows the green CPL spectra acquired at the three different spatial locations (I_1, I_2, and I_3), where it can be seen that the shape and location of the peaks remain approximately unchanged and only the peak intensity of the CPL spectra changes, decreasing in the $[000\bar{1}]$ direction along the vertical cross section of the NW. In addition, the different spatial locations, designated as I_1, I_2, and I_3, are taken along the vertical [0001] growth direction near the top end of the NW below the ZnO NW $(10\bar{1}0)$ surface and are referenced with respect to the slanted top edge where the (0001) and $(10\bar{1}0)$ surfaces meet each other. Therefore using the spectral intensity variation of the

confocal photoluminescence of the green emission at different spatial locations on the surface, the V_o concentrations distribution of the NW can be obtained. The green emission at different spatial locations on the ZnO NW (0001) and $(10\bar{1}0)$ surfaces is found to have maximum intensity near the NW edges, decreasing to a minimum near the NW center.

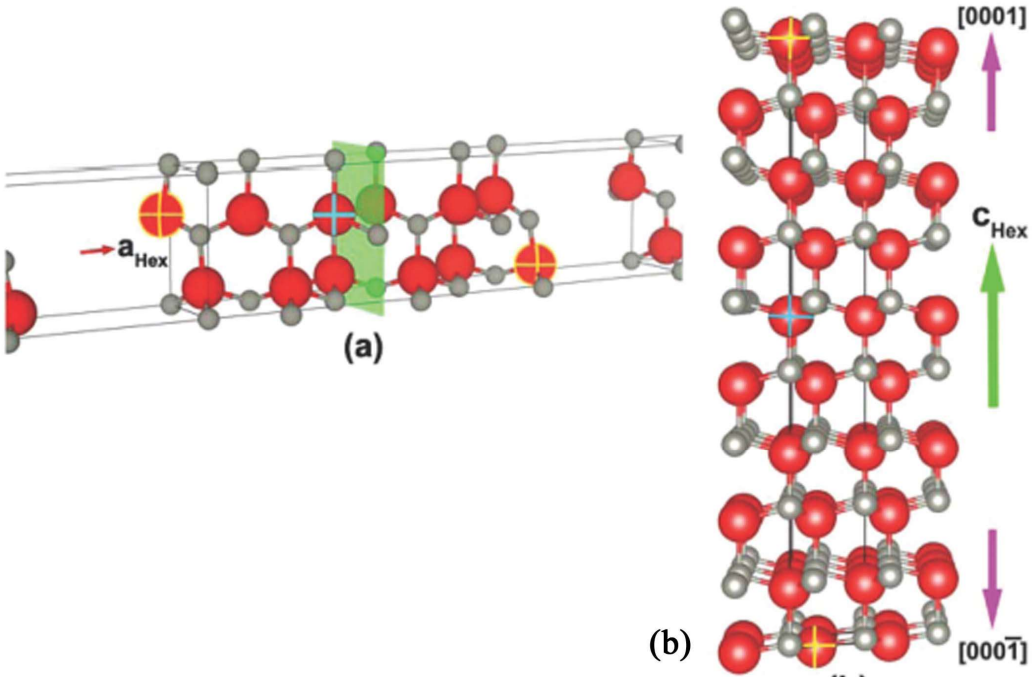

Figure 5-10. (a) Side view of the 6 × 1× 1 SS used for approximating the horizontal cross section of the ZnO NW, and the vacuum region used to decouple the interactions between the consecutive SSs. The green plane represents the center of the 6× 1 × 1 SS. (b) Side view of the 1 × 1× 5 SS used in the approximation of the vertical cross section of the ZnO NW. The O, Zn, surface O-vacancy, and deep O-vacancy atoms are represented by the large red, small grey, yellow-crossed, and blue-crossed spheres, respectively. The 6×1× 1 and 1× 1 ×5 SSs are obtained by stacking the ZnO primitive unit cells along the a_{Hex} and c_{Hex} directions, respectively.

To better understand the spatial profile of the ZnO NW luminescence intensity by the CPL measurements, supercell-slab (SS) models are used in the surface simulations as an approximation of the ZnO NW cross sections from where the confocal measurements are

taken.[222, 223] The SSs used to replicate the polar [(0001)/(000$\bar{1}$)] and non-polar [(10$\bar{1}$0) /($\bar{1}$010)] surfaces has been constructed by stacking the ZnO primitive unit cells along the c-axis and a-axis of the hexagonal lattice, followed by a vacuum region of several Å along these two axes to decouple the interactions between the SSs.[222] Figure 5-10a shows the graphical representation of the horizontal 6 ×1 ×1 (24 atoms) SS that is repeated infinitely along the hexagonal b- and c-axes to model the [(10$\bar{1}$0)/($\bar{1}$010)] surfaces. Figure 5-10b shows the graphical representation of the vertical 1×1×5 (20 atoms) SS that is repeated infinitely along the hexagonal a- and b-axes to model the [(0001)/(000$\bar{1}$)] surfaces. Subsequently, the first principle calculations/simulations using the WIEN2k code is performed solely by Dr. Kin Mun Wong[222, 223] (His personal e-mail addresses are : km2002wong@gmail.com, km2002wong@yahoo.com.sg, kmwong@kinmunwong.me) to simulate the spatial distribution of the oxygen vacancies defect formation energies on the various ZnO NWs surfaces with different crystallographic orientations. This first principles calculations together with the CPL measurements on the ZnO NWs surfaces that are performed exclusively by Dr. Kin Mun Wong[222, 223], consequently lead to a unifying and important theoretical understanding of the spatial variation of the concentration of the V_o defects on the different [(0001)/(000$\bar{1}$)] surfaces of the ZnO NWs, which is beyond the scope of this thesis.

5.2.7 Luminescence lifetimes

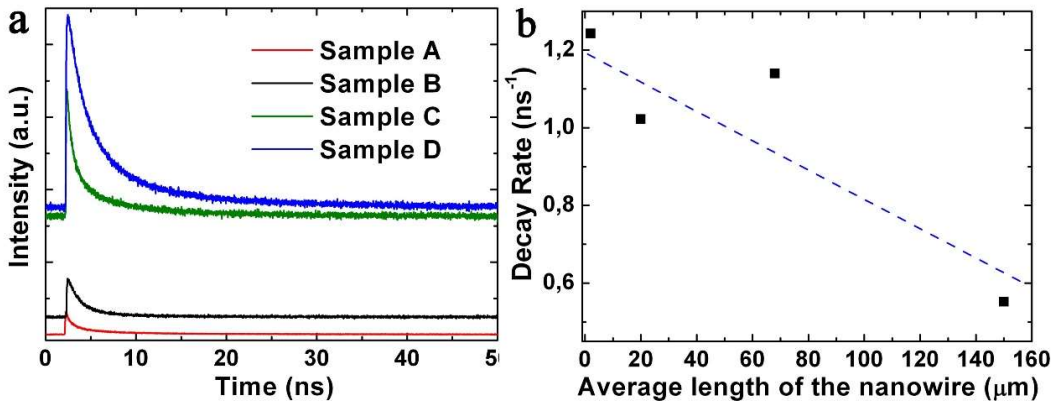

Figure 5-11. (a) Room temperature normalized TRPL spectra for four samples A to D. (b) CPL decay rate versus the length of the ZnO NWs where the linear fitting (dashed line) is also plotted in the figure.

In order to obtain more insight into the luminescence behavior of the ZnO NWs, the CTRPLS measurements has been performed on the ZnO NWs. Figure 5-11a shows the temporal decay curves of PL intensity where a rapid decrease of the PL intensity for samples A to D is observed during the first few ns. The experimental decay curves of the ZnO NWs samples can be fitted with a biexponential function, with a fast and slow time constant with a relationship given by

$$R(t)=A_1 e^{-t/\tau 1} + A_2 e^{-t/\tau 2} \qquad 5\text{-}5$$

where τ_1 and τ_2 are the time constants of the fast and slow radiative decay, respectively. Similarly, $A_1$and A_2 are the constants which determine the contributions of the fast and slow decay components, respectively.

The lifetime parameters upon excitation at 375 nm, obtained by fitting the experimental curves of samples A to D to the biexponential function, are summarized in Table 5-2. On the other hand, the measured PL decay will be strongly dependent on the interplay and relative value of $\tau_1$and τ_2 as well as their relative contributions (calculated as $(A_1)/(A_1+ A_2)$ and $(A_2)/(A_1+ A_2)$) to the PL intensities. These values are shown in Table 5-2 where the weighted average relative contribution of τ_1 and τ_2 is about 67% and 33%, respectively. Both components refer to a radiative decay process which implies that there are two different emissive centers or luminescent states. The two different radiative decay pathways for the synthesized ZnO NWs could be due to the oxygen vacancies located at the surface or at spatial locations deeper in the NW (e.g. V_o in the annulus region in figure 5-7d). According to a recombination model proposed for the green PL emission, the rate of the tunneling recombination between a surface-trapped hole with an electron in an oxygen vacancy defect

decreases for deeper spatial locations beneath the surface.[218] Hence, the fast radiative decay could be due to the oxygen vacancies on the surface of the NW. Conversely, the slow radiative decay may be due to the V_o defects located in spatial locations deeper in the NW due to the decrease of the recombination probability for the V_o defects away from the surface, which will lengthen the lifetime of the radiative decay process.

Table 5-2 Length, S/V ratio as calculated from eqn. (5-1) and the surface and bulk Zn/O composition ratios of the ZnO NWs. The fast (τ_1) and slow (τ_2) time constants from the fit to the biexponential function in eqn. (5-5), the average lifetime ($\tau_{average}$) as well as the relative contributions of the fast decay component (WA_1) and slow decay component (WA_2) to the luminescent from the NWs are also included in the table

Sample	Length /μm	S/V ratio /μm^{-1}	Surface Zn/O ratio from XPS	Bulk Zn/O ratio from EDX	τ_1 /ns	W A_1 (%)	τ_2 /ns	W A_2 (%)	$\tau_{average}$ /ns
A	2	21	1.06	1.07	0.93	70.23	6.15	29.77	2.07
B	20	4.1	1.12	1.14	1.16	64.43	6.23	35.57	2.48
C	68	2.03	1.19	1.20	1.01	63.77	6.88	36.23	3.14
D	150	1.35	1.24	1.22	2.23	69.64	9.58	30.36	4.46

On the other hand, in Table 5-2, both components of the luminescence lifetime decay are smaller for the shorter ZnO NWs (i.e. sample A) as compared to the longer. The shorter radiative lifetime associated with the shorter ZnO NWs implies that the non-radiative processes become more predominant where the photo-generated carriers will have a higher probability of following a non-radiative decay pathway instead of radiative recombination. The non-radiative processes are solely governed by certain point defects incorporated with V_{Zn}, forming the V_{Zn}-X complexes[224] where they function as dominant non-radiative recombination centers (NRCs),[224] as the influence by the single point defects is minimized because according to A. F. Kohan et al., a single point defect may not serve as an NRC.[225]

This is in agreement with the stoichiometry imbalance in our samples as the surface and bulk Zn/O composition ratios (reproduced in Table 5-2) can be used as a measure of the concentration of V_{Zn} defects. A good correlation is observed between the increasing radiative lifetime (fast and slow component) and the increasing surface and bulk Zn/O composition ratio which implies that the concentration of V_{Zn} defects (see Section 5.1.5) and hence the density of the V_{Zn}-X-related defect complexes (NRCs) decreases from sample A to D. Similarly, this will also lead to a decrease of the non-radiative recombination processes (hence an increase of the radiative lifetime) from sample A to D. This shows that the non-radiative decay process may be related to the carrier trapping at V_{Zn} and their complexes in the ZnO bandgap. On the other hand, it is also observed that as the length of the synthesized ZnO NWs increases, the corresponding decreasing S/V ratio could lead to a decrease (slowing) of the scattering rate of the excitons with the surface of the ZnO NWs, which may increase the radiative lifetime due to some surface recombination process.[226]

5.2.8 Influence of the S/V ratio on the radiative lifetime of the ZnO NWs

It has been observed in experimental studies that the radiative lifetime in ZnO NWs exhibits size dependence where the exciton radiative lifetime increases with the size of the ZnO nanostructures and is related to the exciton-polariton effects.[227] It is also theorized that the quantization of the wave vector in the vertical direction inside a nanostructure would decrease the number of possible wave vectors, thus leading to an increase of the radiative recombination time.[228]

Recently, it has been suggested that the radiative lifetime of ZnO nanostructures could be related to the radiative lifetime of the free excitons.[229] For as-synthesized ZnO NWs, the top view of the SEM images in figure 5-2 show that the average size of the NWs increases when its length increases and as calculated from eqn. (5-1), this results in a decreasing S/V ratio (Table 5-2). Consequently, for the synthesized ZnO NWs as its length increases, the

corresponding decreasing S/V ratio could lead to a decrease of the scattering rate of the excitons with the surface of the ZnO NWs, which would then increase the radiative life time due to some surface recombination process.[226] To exemplify this point, by fitting a straight line through the data points in figure 5-11b, a comparison of the slope of the decay rate between the synthesized samples and with the NWs (with diameter between 29 nm to 40 nm) from Hong et al. (Ref.[227]) can be made. The comparison shows that the slope of the decay rate for the synthesized samples is comparatively much smaller (by two orders of magnitude), which indicates a slower scattering rate with the surface. Hence the correlation between the increases of the radiative lifetime with the increase of the length of our ZnO NWs (Table 5-2) could be possibly due to the decrease of the S/V ratio which induces a lower scattering rate with the surface. However, the above mentioned mechanism is surface related which is different from the quantum confinement effect (QCE) which does not have a pronounced effect on the synthesized samples. It is known that QCE also lead to size dependent oscillator strength which increases the radiative lifetime of ZnO nanostructures as its size increases.[230] However, for the synthesized samples, the QCE is negligible as the range of diameters of our synthesized ZnO NWs are much bigger than the Bohr radius of exciton in ZnO (1.8 nm).[231] Interestingly, a decrease in the radiative lifetime depending on the observed increase of the CPL intensity (due to the increase of the concentrations of the oxygen vacancies), corresponding to the longer ZnO NWs was not observed. This could probably be due to the trade-off between the higher concentration of the oxygen vacancies and the decrease of the scattering rate of the excitons due to the smaller S/V ratio corresponding to the longer ZnO NWs, since the former will decrease while the later will increase the radiative lifetime. On the other hand, the relatively long radiative lifetime of the as-synthesized ZnO NWs (in the range of ns) could be due to the localization of the excitons bound to the surface which could result in some elimination of the faster radiative channels.[232]

Based on the above analysis, the combined approach involved different analytical spectroscopic techniques and from the correlation between the different measurements, the concentration of the oxygen vacancies jointly with the zinc interstitials defects and the zinc vacancy defects has been observed to be positively or negatively correlated, respectively, with the magnitude of the photoluminescence intensity and radiative lifetimes. Furthermore, the oxygen vacancy defects are not only spatially located on the surface of the NW but an increasing fraction of the total oxygen vacancy defects connected with the green emission is also located in an annulus region beneath the surface as the ZnO NWs elongate.

5.3 CAFM measurements and the derivation of the analytical model for ZnO NWs

Conductive atomic force microscopy (CAFM) is a viable method for obtaining the current-voltage (I-V) characteristics of the ZnO NW arrays without the prior metallization requirement of the ZnO NW arrays. Hence by considering the conduction mechanism of the reverse biased I-V characteristics in the NWs, an analytical equation (with the use of Padé approximations) is derived for obtaining the donor concentration of the ZnO NW arrays with different lengths directly from its corresponding I-V characteristics.

The Fig 5-12a shows a schematic diagram illustrating the experimental setup of a square configuration for the Hall measurement. The measurements on the ZnO NW arrays has been carried out at room temperature by using the Van der Pauw four probe technique with a square configuration utilizing an Accent HL5500 system. The schematic diagram in figure 5-12b illustrates the I-V measurement setup. The measurements of the ZnO NWs are performed by selecting an appropriate NW from the surface topography image first acquired in the AFM mode. Subsequently, the I-V curves are obtained by applying an external voltage bias (from +5 V to -5 V) between the 50 nm Pt-coated Si probe tip placed on top of the ZnO NW and the sample stage (where the Si substrate rests upon). A Schottky barrier is formed between the Pt-coated probe tip and the ZnO NW at the contact interface[6] where the current will flow

vertically through the probe tip-ZnO NW Schottky interface. Silver paste is applied on the edge and underside of the sample to ensure better electrical connectivity of the bottom of the ZnO NWs on the Si substrate surface with the measurement circuit as well as to ensure that the sample is well grounded.[6] The typical I-V curves corresponding to the ZnO NWs of different lengths measured at room temperature are shown in figure 5-12c where the current in both the forward and reverse bias region for the longer ZnO NW is smaller as compared to the shorter ZnO NW. This could be due to the increased resistance for charge transport as the increased resistivity of the longer NWs is due to higher donor concentration (from the Hall measurements).

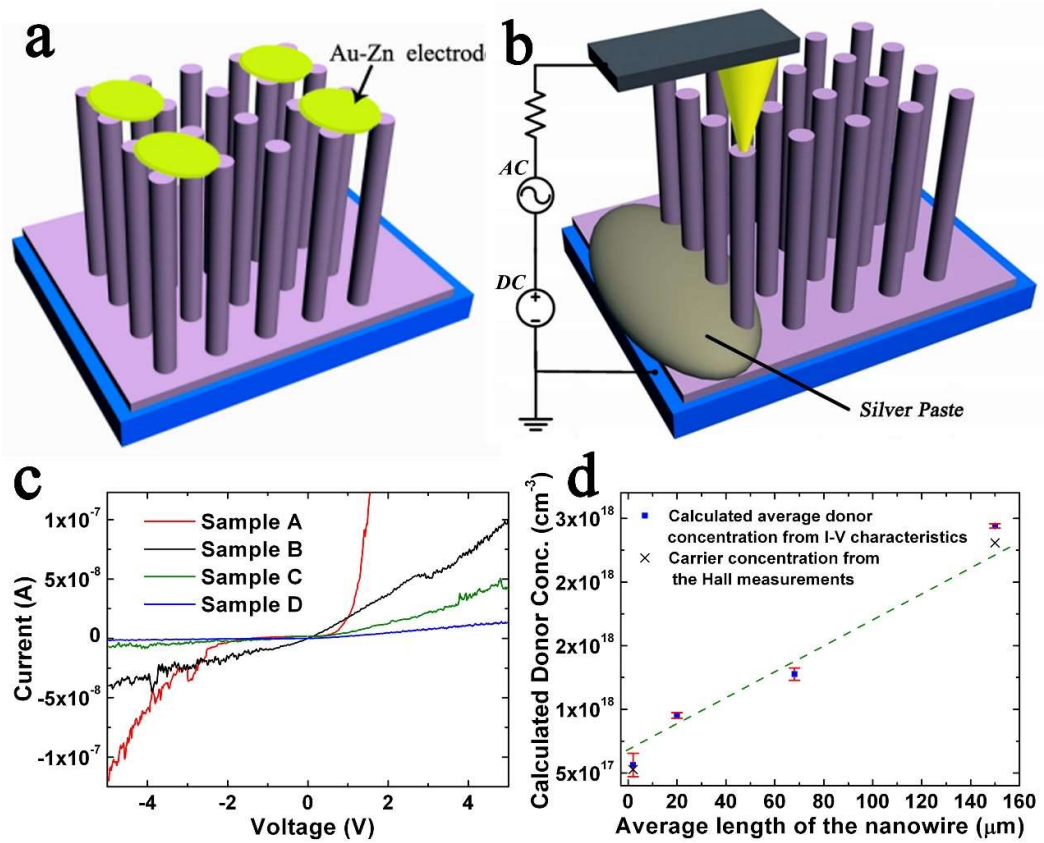

Figure 5-12. (a) Schematic diagram of the ZnO NWs arrays sample with the Au-Zn electrodes for the Hall measurements. (b) Schematic diagram showing the use of an

AFM probe to measure the I-V characteristics corresponding to an individual ZnO NW in a vertical NW array. (c) I-V characteristics from a vertical ZnO NW corresponding to samples A to D with a conductive AFM probe. (d) Comparison of the calculated donor concentration as a function of the average NW length with the carrier concentration obtained from the Hall measurements. The error bars indicate the standard deviations of the donor concentration calculated from the I-V characteristics corresponding to the ZnO NW using eq. (5-11)

On the other hand, the I-V characteristics in figure. 5-12c also display a rectifying behavior in the negative voltage region with a low rectification ratio I_F/I_R (ratio of forward to reverse current measured at V= ± 4 V) between 3 and 10 for the four different nanowires. As the rectification ratio depends on the interface between the probe tip and the ZnO NW, this observation could be correlated to the prevalence and non-negligible effects of interface states between the probe tip and ZnO which originates from surface imperfections such as defects on the ZnO NW surface (evident from the TEM images in figure 5-3).[233] From the determination of the saturation current, $I_{S,Pt-NW}$, by extrapolating the logarithmic plot of the I-V characteristics in figure 5-12c under forward bias to V= 0 V, the barrier height of the Schottky potential barrier at the probe tip-ZnO NW interface, $\emptyset_{Pt-NW}$ for sample A to D can be determined and is given by[2]

$$\emptyset_{Pt-NW} = \left(\frac{KT}{q}\right)\ln\frac{A_{\text{Pt-NW}}A^{*}T^{2}}{I_{S,Pt-NW}} \qquad 5\text{-}6$$

where $A_{\text{Pt-NW}} = \pi r^2_{\text{NW,average}}$ is the effective contact area at the probe tip-ZnO NW interface which is assumed (for simplicity) to be equal to the average cross-sectional area of the NWs and $r_{NW,average}$ is the average radius of ZnO NW as estimated from the SEM images in figure 2-2. q is the elementary charge, k is the Boltzmann's constant, and T is the absolute temperature in Kelvin. $A^* = 4\pi q\, m_e^* k^2/h^3$ is the effective Richardson constant (without

considering the effects of quantum mechanical reflection and optical phonon scattering) with a theoretical value of $32AK^{-2}cm^{-2}$ for $m_e^* = 0.27m_o$[2] where h, and m_e^* and m_o are the Planck's constant, electron effective mass and rest mass respectively.

The donor concentration of the ZnO NW indirectly affects many of its electrical properties, hence a simple way of obtaining the donor concentration directly from the I-V characteristics will be very useful for characterization purposes. Under reverse bias and in low-dimensional nanostructures, the Schottky potential barrier at the probe tip-ZnO NW interface, $\emptyset_{\mathrm{Pt-NW}}$ becomes narrower and the tunneling current of electrons from the probe tip to ZnO through the reverse biased Schottky barrier becomes more significant. At room temperature and for reverse bias voltage, the tunneling current is predominantly due to the thermionic field emission current[2, 234]and the current density through $\emptyset_{\mathrm{Pt-NW}}$ is given by[2]

$$J_{Pt-NW} = \frac{A^{**}T}{K}\sqrt{\pi E_{00} q[V_R + \frac{\emptyset_{Pt-N}}{cosh^2(E_{00}/KT)}}]\exp(\frac{-q\emptyset_{Pt-NW}}{E_0})\exp(\frac{qV_R}{\varepsilon'}) \qquad 5\text{-}7$$

$$\text{where } \varepsilon' = \frac{E_{00}}{(E_{00}/KT) - \tan\ (E_{00}/KT)} \text{ and } E_0 = E_{00}\coth(\frac{E_{00}}{KT}) \qquad 5\text{-}8$$

where E_{00} is the characteristic energy relating to the tunnelling probability

$$E_{00} = \frac{qh}{4\pi}\sqrt{\frac{N_d}{\varepsilon_s m_e^*}} \qquad 5\text{-}9$$

In Eq. 5-7, A^{**} is the reduced effective Richardson constant which takes into account of the effects of optical-phonon scattering and quantum mechanical reflection.[2] $\varepsilon_s = \varepsilon_r\varepsilon_o$ is the permittivity of the ZnO NW, $\varepsilon_r = 8.36$[234] is the relative permittivity of the ZnO NW used in this study (corresponding to thin ZnO film as the quantum confinement effects in the synthesized ZnO NW is not significant because r_{NW} is larger than the ZnO exciton Bohr radius 27) and ε_o is the permittivity of free space. Firstly, eq. (5-8) is substituted into the $\exp(\frac{qV_R}{\varepsilon'})$ term of eq. (5-7) and the result is simplified followed by taking the natural

logarithms on both sides of the resultant equation. After a series of algebraic manipulations, it is realized that in order to obtain a mathematical expression which permits further algebraic evaluation, the Padé approximant technique[235] would have to be used to express one of the algebraic terms by an approximate rational expression. Subsequently, a long and complicated expression is obtained where the terms with the variable ''V_R'' and ''ln I_R'' can be grouped together. Therefore the donor concentration can be obtained directly from the slope of the reverse bias ln I_R-V_R characteristics corresponding to the ZnO NW (denoted as G_R) given by

$$G_R = \frac{cosh^2(1)}{8\emptyset_{Pt-N}} + \frac{q}{KT} - \frac{q}{E_{00}coth(1)} \qquad 5\text{-}10$$

and by rearranging the above equation and using the definition of E_{oo}, the donor concentration of a single ZnO NW is given by

$$N_d = \frac{16\pi^2 m_e^* \varepsilon_r \varepsilon_o}{h^2 coth^2(1)[\frac{cosh^2(1)}{8\emptyset_{Pt-N}} + \frac{q}{KT} - G_R]^2} \qquad 5\text{-}11$$

It should be noted that the unit of N_d in eq. (5-11) is in m^{-3} and multiplying by a factor of 1 x 10^{-6} is needed to convert the doping concentration to cm^{-3} (m^{-3} = 1 x 10^{-6} cm^{-3}). From the reverse I_R-V_R characteristics in figure 9-12d, an almost linear variation of the reverse current is observed for the semi-log reverse bias ln I_R-V_R characteristics corresponding to the four sets of ZnO NW arrays. From the slope of the plots and eq. (5-11), the donor concentration of the ZnO NW from samples A to D is shown in figure 9-12d. The donor concentration calculated from the analytical model is in good agreement with the carrier concentration obtained from the Hall measurements for samples A and D which verifies the validity of the assumptions used in the analytical model. On the other hand, the concentration of V_o and Zn_i defects (from the stoichiometric analysis 5.1) is also positively correlated with the increase in the length and donor concentration of the synthesized ZnO NWs. This could be possibly due

to the attractive force between the V_o and Zn_i defects present in the NWs,[236] which function as a source of donors for the n-type conductivity in the NWs.[237]

5.4 Synthesis and field emission properties of different ZnO nanostructures

5.4.1 Background

According to the Fowler-Nordheim theory, the FE characteristics are strongly influenced by two parameters. One is the field enhancement factor (β) that is defined by the ratio of the local to the applied field, which is associated with the composition, tip diameter, and aspect ratio[3, 136, 138, 171, 238] and the other is the work function (Φ) of the emitters, which is associated with the external conditions (for example doping).[131, 136, 171, 239] Compared with other FE materials, such as carbon nanotubes,[126] WO_3,[130] SnO_2,[129] Si NW,[128] and In_2O_3,[127] ZnO nanostructures are much easier to realize a high aspect ratio and small tip radius.[120] In addition, owing to their negative electron affinity, high mechanical strength, and chemical stability in high vacuum environment, hence the properties of the ZnO nanostructures have been extensively investigated in the field emission domain. In these applications, the structural parameters (sizes, defects and doping of the ZnO nanostructures) can optimize the properties of FE. For example, a high aspect ratio is in favor of the electron emission and the presence of oxygen vacancies or impurities incorporation could reduce the work function.[3, 136, 140, 141]

In this section, the self-assembly of the ultralong ZnO nanowire arrays without any catalyst on a silicon (100) substrate are fabricated by the CVD method where the length of the nanowires is about 310 μm after a reaction time of 60 mins. The needle-like ZnO nanostructures are prepared by the two step methods: the first is the CVD process and the second is a modified low-temperature solution. In addition, there are few reports about the ZnO superlattice phenomenon at the presence of Indium to date. Here, without the use of catalysts (such as Sn

and In),[240-242] the modulated structures of the $In_2O_3(ZnO)_m$ by In doping are realized by the CVD process.

5.4.2 Morphologies for ZnO NWs

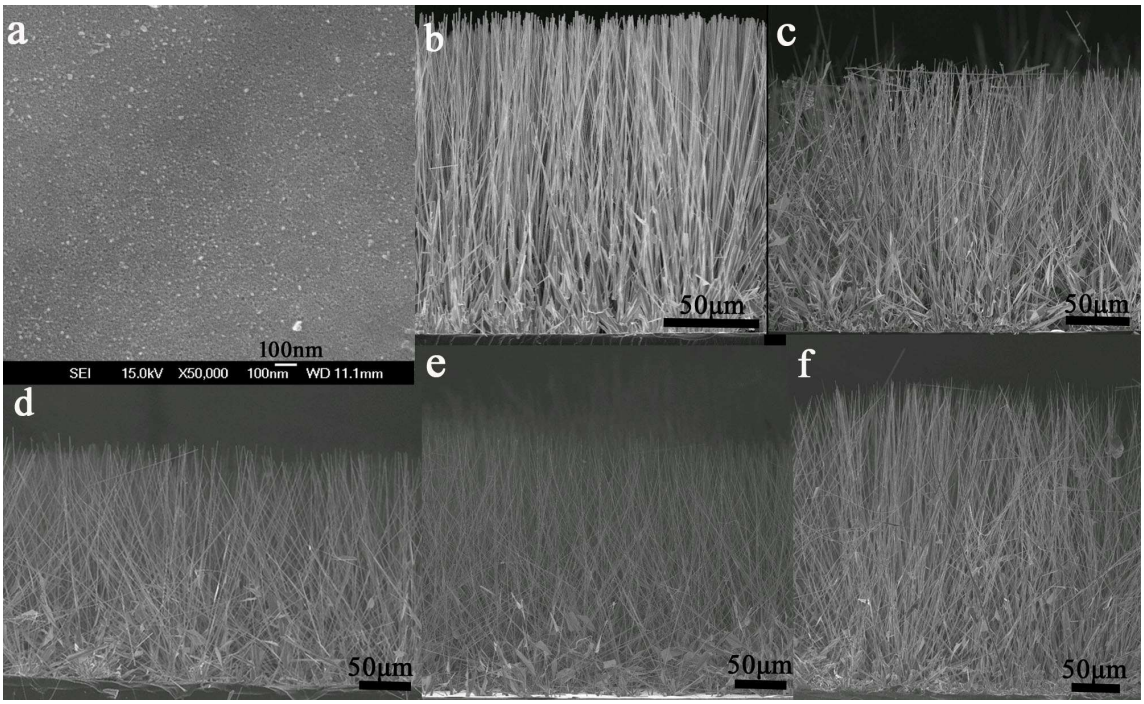

Figure 5-13 SEM images of the synthesized arrays of ultralong ZnO NWs by the CVD process. The image in (a) shows a film of ZnO seed layers. The SEM images in (b), (c), (d), (e), and (f) display the length and distribution of the ZnO NWs. The ZnO NWs with length of 150, 185, 220, 250, and 310 μm correspond to the reaction times of 22, 30, 40, 50, and 60 min, respectively.

Figure 5-13 shows the SEM images of the synthesized arrays of ultralong ZnO NWs by the CVD process, and the length of the NW array is in the range of 150 to 310 μm and gradually increases with the reaction time increasing. In figure 5-13b, c, d, e, and f, it is seen that when the length of the ZnO NWs increases beyond 185 μm (after a reaction time of 30 min, Figure 5-13c), the regularity of the vertical alignment of the NWs with respect to the Si substrate becomes poorer.

5.4.3 Growth mechanism of ZnO NWs

The growth mechanism of nanostructures is usually explained by the vapor-liquid-solid (VLS) and vapor-solid (VS) processes,[117] where according to the VLS growth mechanism, a droplet of the liquid alloy is a key role in the reaction process, and hence, the VLS mechanism is also known as catalysis growth.[117] In this work, catalyst is not used in the synthesis of ZnO NWs by the CVD route; hence, the VS mechanism is appropriate for the explanation of the growth process of ZnO NWs.

In reaction process, with the reaction temperature increasing, ZnO seed layers are generated via $Zn(AC)_2$ thermolysis and new ZnO vapors are generated by the carbothermal reduction of ZnO (s). The reaction processes are as followed:

$$C(s) + 1/2O_2(v) \rightarrow CO(v); \quad 5\text{-}12$$

$$ZnO(s) + C(s) \rightarrow Zn(v) + CO(v); \quad 5\text{-}13$$

$$ZnO(s) + CO(v) \rightarrow Zn(v) + CO_2(v); \quad 5\text{-}14$$

$$2Zn(v) + O_2(v) \rightarrow 2ZnO(s); \quad 5\text{-}15$$

$$ZnO(s) + CO(v) \rightarrow ZnOx(s) + CO_2(v)。 \quad 5\text{-}16$$

The Si substrate lies at a zone where the temperature is high for the CVD process and is close to the source materials with a high concentration of ZnO vapor for deposition. Since the ZnO seed layers have a same or well-matched lattice structure with ZnO vapor. The growth of the deposited crystal is oriented by the seed layers, which keeps the system at a lower surface energy. Therefore, with the reaction going on, ZnO vapor that deposited on the seed layers of the Si substrate grow along (0001) direction (the lattice orientation of the seed layers).

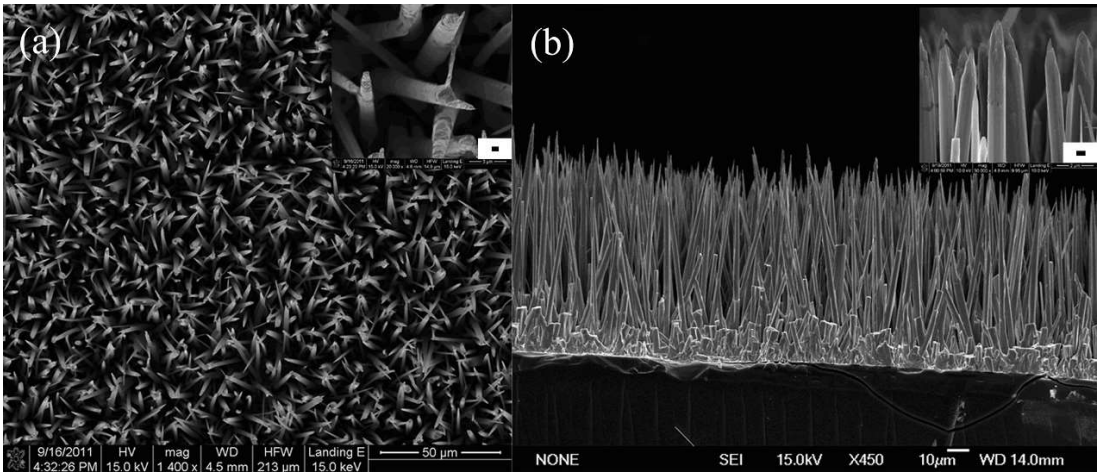

Figure 5-14. Typical SEM images of the needle-like ZnO arrays. (a) SEM image of the needle-like ZnO NWs; the scale bar in the inset is 500 nm. (b) Side-view SEM image of the needle-like ZnO NWs; the inset shows the top parts of the NWs.

5.4.4 Morphologies for needle-like ZnO NWs

Figure 5-14 shows the typical SEM image of the needle-like ZnO arrays first prepared by synthesizing arrays of long ZnO NWs followed by chemical etching in the reaction solution. The diameter at the top part of the etched NWs is about 100 nm. As the needle-like NWs are obtained by the chemical etching of the NWs previously prepared by the modified CVD process, hence, the synthesized NWs are also longer than those prepared by other methods. In addition, surfactants play a key role in the reaction process of ZnO needle-like arrays. In the presence of EDTA-2Na and trisodium citrate, which may preferentially adsorb onto certain surfaces of the ZnO NWs and thus induce the morphology change in the NWs? Hence, I propose that the formation of the needle-like structure may result from the strong chelation reaction of negatively charged EDTA and citrate ions with positively charged Zn^{2+} ions in the (0001) plane. Moreover, under the joint action of Zn^{2+} and surfactants, the concentration of Zn-EDTA and $[C_6H_5O_7]_2Zn_3$ is much more than $Zn(OH)_X$, and they are soluble in solution (Eq.5-17 and 5-18). Therefore, with the increase of the reaction time, the top part of the ZnO

NWs will be etched to needle-like structures under the surfactants action. With further reaction, as more of the complexes begin to form and dissolve into the reaction solution, the top part of the ZnO NWs were modified to be tapering in shape.

$$EDTA\text{-}2Na + Zn^{2+} \leftrightarrow Zn\text{-}EDTA + 2Na^{+} \qquad 5\text{-}17$$

$$2[C_6H_5O_7]\text{-}3Na + 3Zn^{2+} \leftrightarrow [C_6H_5O_7]_2Zn_3 + 6Na^{+} \qquad 5\text{-}18$$

5.4.5 Leaf-like In-doped ZnO nanostructures

The crystal structures of the leaf-like indium (In)-doped ZnO nanostructures are investigated by XRD measurements. As shown in figure 5-15a, the main diffraction peaks corresponding to wurtzite ZnO where a = b =3.24982 Å, c = 5.20661 Å (the red lines: JCPDS Card No.36-1451) and the blue lines: cubic In_2O_3 (the blue lines: JCPDS Card No.06-0416) are observed in the spectrum. Figure 5-15a also shows that the (101,100) diffraction peaks are much stronger than the other peaks, which indicates that the crystal facets may be the main growth plane of the as-prepared structures. On the other hand, SEM photographs of the indium-doped ZnO nanostructures in figure 5-15b, c, d, e, and f are prepared with the reaction time of 5, 10, 15, 20, and 30 mins, respectively. These figures show that, with increasing reaction time, the leaf-like structures become more apparent, where self-assembly flower-like structures composed of nanoparticles and nanobelts are observed on the seed layers as shown in figure 5-15d and 5-15e at a longer reaction time of 15 and 20 mins (initially in figure 1b, the film is consisted of microparticles). The width and length of the belt-like structures are around 300 to 600 nm and several micrometers, respectively, as shown in the figure 5-15e. Finally, after a reaction time of 30 mins, large-scale leaf-like structures are self-assembled on the seed layers as shown in figure 5-15f where the thickness of the leaf-like branches is about 100 nm.

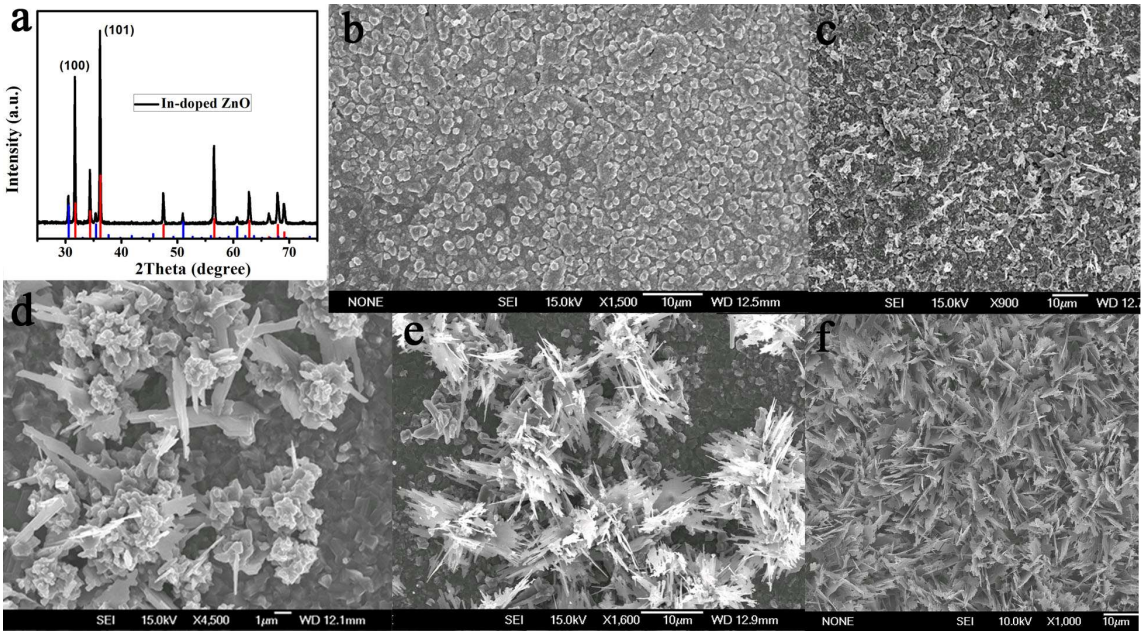

Figure 5-15. (a) XRD pattern of the leaf-like In-doped ZnO nanostructures (the red lines are ZnO with JCPDS Card No.36-1451 and the blue lines are In_2O_3 with JCPDS Card No.06-0416). (b), (c), (d) (e), and (f) SEM images of the leaf-like nanostructures at different reaction times of 5, 10, 15, 20, and 30 mins, respectively.

In order to obtain more details about the structures and compositions of the leaf-like nanostructures, HRTEM and EDX measurements are applied for further characterization. Figure 5-16a shows that TEM image is consisted of the bright field and the dark field. As shown in figure 5-16b, HRTEM image taken from the junction between the bright field and dark field parts (Figure 5-16a, square region) indicates different lattice fringes of the modulated and single-phase structures, respectively. Importantly, the lattice spacing of 0.283 nm between adjacent lattice planes is consistent with the interplanar spacing of $(10\bar{1}0)$ plane of ZnO wurtzite hexagonal phase. It is also demonstrated that the top and bottom surfaces of the leaf-like structures are the ± (0001) planes, and the growth orientation is along the a/b axis of the ZnO wurtzite hexagonal phase (along $[10\bar{1}0]$ direction). For the periodic wide crystal fringes (the modulated structures), it could be possibly due to the reason that the Zn sites in

the Zn-O slab are randomly replaced by the In atoms, and thus local lattice distortions are produced. On the other hand, Zn, In, and O elements are observed in the energy dispersive X-ray spectroscopy (EDX) spectrums corresponding to the bright field (Figure 5-16c) and dark field (Figure 5-16d) parts, respectively. In the small and big circles, the element indium is also observed in the bright field part (small circle) as shown in figure 5-16c. In addition, the EDX results indicate that a close value of molar ratio Zn and In is around 3.5:1 in the bright field part.

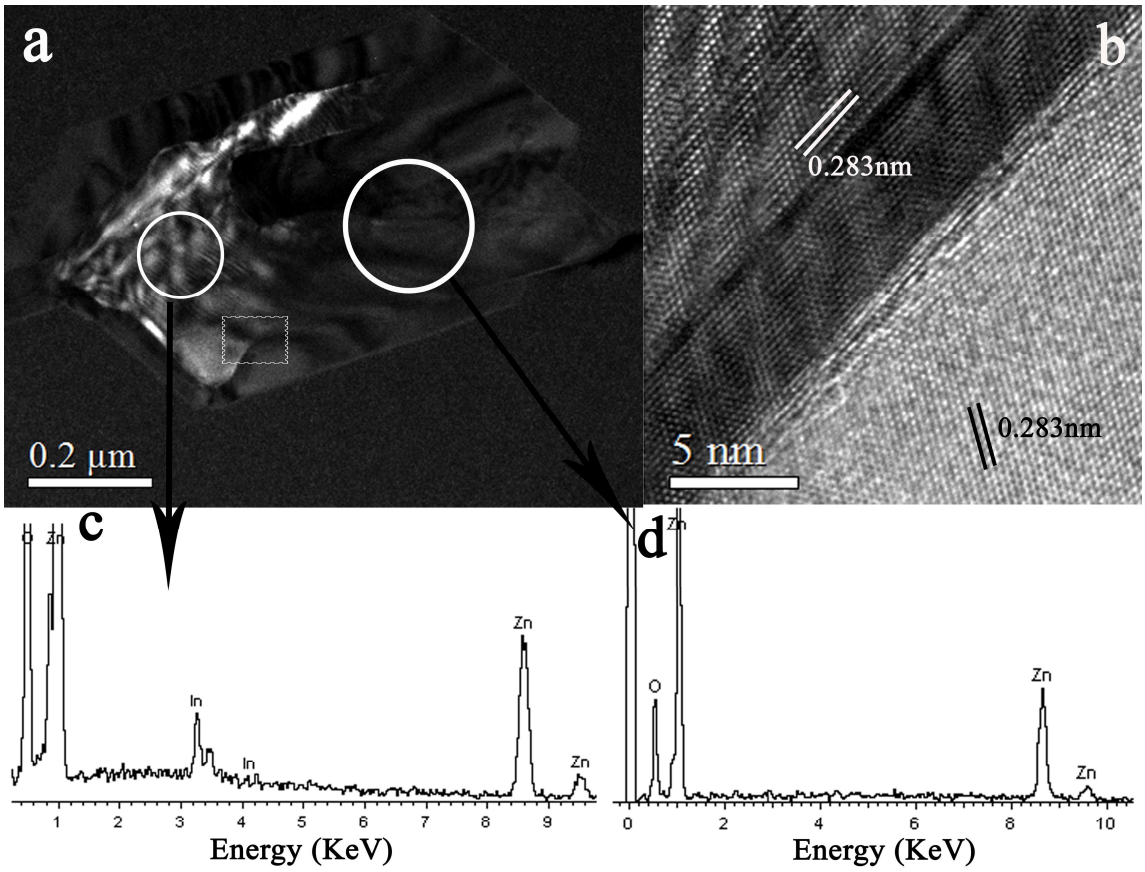

Figure 5-16. (a) TEM images of the bright field and dark field parts of the leaf-like nanostructures. (b) HRTEM image corresponding to the square in (a); EDX patterns (c) and (d) corresponding to the bright field (small circle) and the dark field regions (big circle), respectively, in figure (a).

To further characterize the modulated structures, figure 5-17a shows the HRTEM image of the modulated structures in the bright field part where the wide white and narrow white lines with a width of 0.28 nm correspond to the In-O layers and In/Zn-O layers, respectively, where the growth direction of the In/Zn-O layers is along the $[10\bar{1}0]$ direction (crystal ZnO growth direction), as indicated in the figure 5-16b and 5-17a[240]. However, due to some significant changes to the structures of the leaf-like indium-doped ZnO nanostructures, the stacking layers (wide crystal lattice lines) do not grow along the $[10\bar{1}0]$ orientation but at an angle about 30°, as indicated by the arrow in the HRTEM image. The results are different from previous reports.[240]

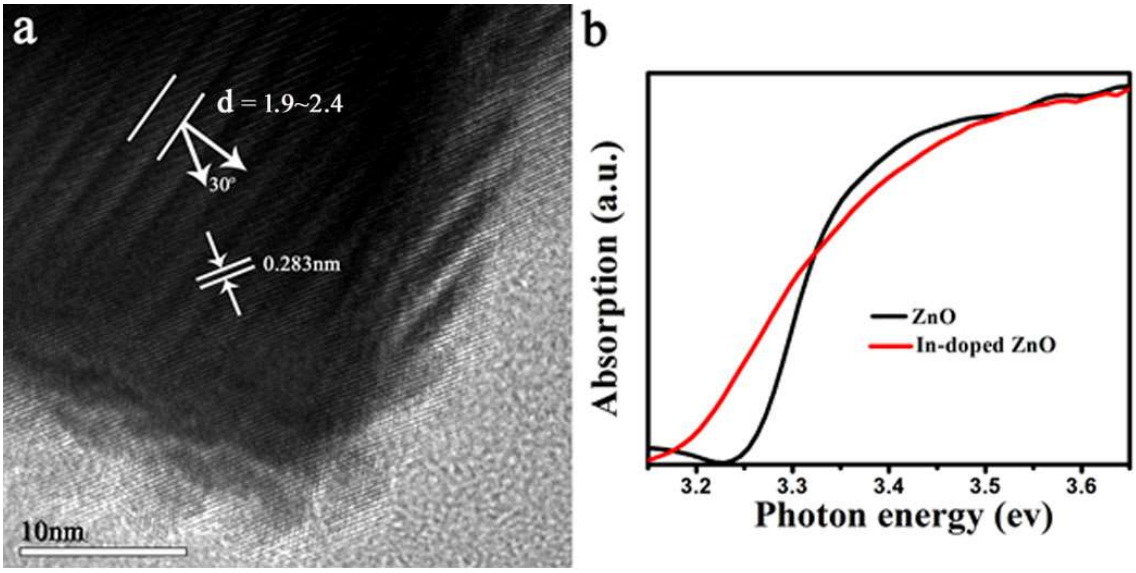

Figure 5-17. (a) HRTEM image of the superlattice/modulated structure (the bright field). (b) Room temperature UV-Vis of the (red line) leaf-like and wire-like (black line) ZnO nanostructures.

In addition, Figure 5-17a illustrates that the wide white lines corresponds to the In-O layers consist of about seven or eight In/Zn-O layers (the narrow white lines, 0.283 nm). For the $In_2O_3(ZnO)_m$ compounds, there is a linear relationship for the width, d of the In-O layer (the wide white lines), given by[243]:

$$d = \text{Cos } 30^{o} \times (6.349 + 2.602m)\ \text{Å} \qquad 5\text{-}19$$

where m is the subscript in the chemical formula of the $In_2O_3(ZnO)_m$ compound. From the HRTEM image in figure 5-17a, the average value of d is about 19 to 24 Å (width of the white line), and hence, the value of "m" as calculated from Equation 5-19 is between 7 to 8. Thus, the composition of the synthesized leaf-like structures in the bright field part is estimated as $In_2O_3(ZnO)_7$ or $In_2O_3(ZnO)_8$. The results of the EDX spectrum are also applied to detect the component ratios of Zn and In, which shows a close value of the molar ratio of Zn: In at approximately 3.5:1 or 4:1. Therefore, the dark field part of as-synthesized leaf-like nanostructure is pure ZnO, and the bright field part is consisted of a modulated structure with $In_2O_3(ZnO)_7$ and $In_2O_3(ZnO)_8$.

5.4.7 UV-Vis spectra for doped/un-doped ZnO nanostructures

Figure 5-17b shows the room temperature UV-Vis spectra for leaf-like In-doped (red line) and wire-like (black line) ZnO nanostructures. UV-Vis band of In-doped ZnO structures shifts to a lower energy. According to the theory of semiconductor-metal transition, the bandgap energy Eg decreases when the impurity is more than the Mott critical density;[244] hence, In doping leads to an obvious narrowing of Eg.

5.4.8 Growth mechanism of leaf-like In-doped ZnO nanostructures

In addition, the growth process of leaf-like ZnO structures is given as follows: the Si substrate in the furnace is close to the source materials and lies at a zone where the temperature is high for the CVD process. Therefore, there is a higher distribution of vapor concentration near the substrate. In the reaction process, with increasing the reaction temperature, indium and zinc vapor are generated by the carbo thermal reduction of In_2O_3 and ZnO, respectively. Hence, a small binucleus structure is firstly synthesized on the substrate by the Zn and In mixture vapor atoms. At this condition where there is a combination of the high vapor concentration and

temperature, the Zn-In diphase will be supersaturated, and the seed layers gradually form. With the increase of the reaction time, newly formed In/Zn atoms continue to deposit on the seed layers and result in the morphologic evolvement from nanoparticles to belt-like and to leaf-like structures on the seed layers, respectively. In addition, to keep the system at a lower surface energy, the new arriving In/Zn atoms will react with the pumped-in oxygen gas and are adsorbed on the initial particle-like surfaces. Then, they tend to grow along the longitudinal and transverse growth directions at the same time, which forms belt-like and then leaf-like structures as well as keeps the system at a lower surface energy.

As for the different lengths and widths of the leaf-like branches, it is possible that there is some influence of some thermal or strain instability at the gas-solid interface state which does not involve much energy since the free energy is the same for the equivalent $[10\bar{1}0]$ planes. In addition, the doped In atoms are obtained by the process of substituting the Zn atoms with the In atoms in the ZnO structures so that the system can be held at a lower energy[33]. By doping ZnO with In, the growth orientations of the resultant nanostructures varied from the highest-energy, low-index planes, and a fast growth along [0001] to the sideway growth $[10\bar{1}0]$ direction is observed.[25, 244] In addition, the new arriving In and Zn atoms in the vapor directly deposit on the surface of In-doped ZnO belt-like structure, and this direct deposition induces the growth of the side faces and thus further leads to the formation of leaf-like structures by epitaxial growth.

5.4.9 Field emission properties of the different ZnO nanostructures

For an analysis of the field emission properties of the different ZnO nanostructures, the following Fowler-Nordheim (F-N) equation would have to be used:

$$J = \frac{A\beta^2 E^2}{\phi} \exp\left(-\frac{B\phi^{3/2}}{\beta E}\right) \qquad 2\text{-}1$$

where J is the current density, E is the applied field strength, A and B are constants with the values of $1.56\times10^{-10}AV^{-2}$ eV and 6.83×103 $V(eV)^{-3/2}\mu m^{-1}$, respectively, ϕ is the work function of the emitter which is taken as 5.4 eV for ZnO from the literature,[245] and β is the so-called field-enhancement factor, which reflects the ability of the emitters to enhance the local electric field. The field-enhanced factors β can be calculated from the formula $\beta= -B\phi^{3/2}/S$, where S is the slope of the F-N plot.

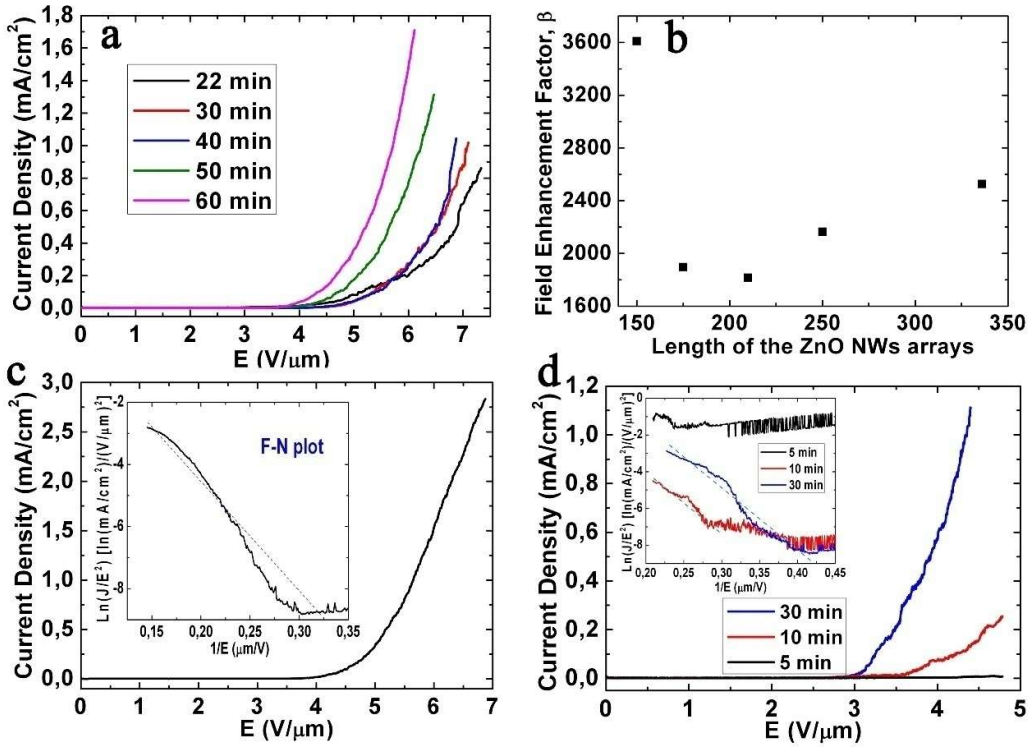

Figure 5-18. (a) J-E curves of the long ZnO NWs at different reaction times, (b) Field-enhanced factors of the long ZnO NWs of different lengths. (c) Field emission current density as a function of the applied field for the needle-like sample. The inset in the figure c shows the corresponding Fowler-Nordheim (F-N) plot. (d) J-E curves of the leaf-like ZnO nanostructures at different reaction time (5, 10, and 30 min). The inset in the figure d shows the corresponding F-N plots.

Figures 5-18a and b show the plot of the emission current density versus the electric field of the long ZnO NWs at different reaction time and their corresponding field-enhancement factors, respectively. When the reaction time increases from 22 to 60 mins, the turn-on field (defined as the applied field at the emission current density of 10 μA/cm^2) decreases from 4.56 to 3.69 V/μm, respectively. In addition, the emission current density of the curves also decreases from 7.09 to 5.72 mA/cm^2 at the threshold field. Hence, the 60-min sample possesses better field emission properties as compared to the others (22- to 50-min samples). Based on the formula in Eq. 2-1, the experimental β values for the 22- to 60-min samples are plotted in figure 5-18b showing a turning point in the plot of β value.

The turning point of the field-enhancement factors versus the length of ZnO NWs can be explained as follows. To the first approximation, the field-enhancement factor, β can be given by $\beta = h/r$[246] where h is the length or height and r is the radius of the NWs, respectively. As a result, as the length of the NWs increases, this will increase the value of β. On the other hand, it is also experimentally observed (section 5.3) that the concentration of the oxygen vacancies (V_o) is positively correlated with the increase in the length of the ZnO NWs. This increase of the concentration of V_o corresponding to the longer ZnO NWs will then lead to an increased barrier for electrons emission,[138] thus leading to a decrease of the corresponding experimentally observed β value for the longer ZnO NWs. Therefore, these two contrasting mechanism which result in the increase and decrease of the value of β, respectively, will lead to a turning point in figure 5-18b as the length of the ZnO NWs varies.

Figure 5-18c shows the current density-electric field (J-E) plot corresponding to the needle-like ZnO arrays. The turn-on electric field of the ZnO needle-like arrays is about 3.87 V/μm at a current density of 10 μA/cm^2, while the electric field corresponding to the current density of 1 mA/cm^2 is 5.65 V/μm (the β value for the needle-like arrays is about 2,284), and these results are close to the 60-min ZnO NWs sample. However, although the smaller diameter at

the top part of the needle-like structures could easily induce much more electrons emission, the needle-like ZnO NWs are densely packed. Hence, the screening effect between the neighboring emitters and a lower h/r would decrease the experimentally observed value of β corresponding to the needle-like ZnO NWs[245] as compared to the long ZnO NWs.

Figure 5-18d shows the typical leaf-like ZnO nanostructure field emission current density versus the applied field (J-E) curves and the corresponding F-N plots (the inset) at different reaction time, respectively. In this figure, when the reaction time increases from 5 to 30 mins, the turn-on field (defined as the applied field at the emission current density of 10 $\mu A/cm^2$) is decreased to 2.94 V/μm (which is lower than the previous reports[25, 244, 247]). On the other hand, the emission current density of the curve corresponding to the reaction time of 30 mins is about 1 mA/cm^2 at an applied field of about 4.35 V/μm (so-called threshold field); thus, the 30-min sample possesses better field emission properties as compared to the 5- and 10-min samples. One possible reason could be that the 30-min leaf-like ZnO nanostructure is comprised of much more rod-shaped structures (or tips) as compared to the other two samples. On the other hand, the increased indium doping in the 30-min sample as compared to others could lead to further band gap narrowing and the moving closer of the Fermi level towards the bottom of the conduction band. Hence, the increased carrier concentration in the 30-min leaf-like ZnO nanostructure could have led to the increase of the field emission current and better field emission properties as observed in figure 5-18d. Based on Eq. 2-1, the experimental β value for both the 30- and 10-min leaf-like ZnO nanostructure samples is close to 2,800. Conversely for the 5-min sample, the corresponding J-E curve in figure 5-18d is observed to be nonlinear, and it could be possibly due to the reason that the sample is consisted of microparticles, thus leading to a relatively high turn-on field and a nonlinear relationship. F-N plots are consisted of two parts linearity as shown in the inset of figure 5-18d. The possible reasons are that the first emission from electrons captured in the defect

states is dominant in the lower electric field range; the second from electrons near the Fermi level is in the high electric field range with Indium doping. The former emission process is easier than the latter and are strongly dependent on the amount of lattice defects. While the latter emission process becomes dominant in higher electric field ranges, resulting in a drop in the F-N plots.

Table 5-3 summarizes the field emission properties of the three different synthesized ZnO nanostructures, and it shows that the leaf-like ZnO nanostructures are most suitable for field emission due to its lowest turn-on and threshold field as well as its relatively high field-enhancement factor. Hence, the synthesized leaf-like structures will be promising in the applications of electron sources or flat panel displays. In addition, the use of this chemical etching route provides a simple, convenient, and low-cost method of obtaining the needle-like NWs. Therefore, this fabrication technique will offer a method to prepare well-aligned, longer, and sharper NWs with applications in the promising devices.

Table 5-3 Comparison of the field emission properties between the different ZnO nanostructures

Type of ZnO nanostructures	Turn-onfield (V/μm)	Threshold field (V/μm)	β
Long NWs arrays (60 mins)	3.69	5.72	2,526
Needle-like	3.87	5.65	2,284
Leaf-like (30 mins)	2.94	4.35	2,800

6 Summary and outlook

In this thesis, ZnO nanostructures (including ultralong NWs, needle-like NWs, and leak-like In-doped ZnO) and their applications on field emission are investigated. The main contributions can be summarized as followed:

(1) ZnO NWs of different lengths from 2 μm to 310 μm and sizes are prepared by the aqueous solution method and CVD process without the assistance of a catalyst. Subsequently, using chemical etching process, needle-like NW arrays can be obtained, which is a relatively low-cost and convenient method.

(2) The SEM images show that the average diameter and length of the NWs increases with the reaction time increasing, thus resulting in a decreasing S/V ratio for the longer NWs. XPS, EDX, CPL and PL measurements exhibit a clear correlation of the increase of the V_o, Zn_i, PL intensity and decrease of the zinc vacancies, respectively, with the increase of the length of the ZnO NWs. In addition, the V_o defects are not only spatially located on the surface of the NW but also in the annulus region beneath the surface.

(3) The green emission at different spatial locations on the ZnO NW polar (0001) and non-polar ($10\bar{1}0$) surfaces is found to have maximum intensity near the NW edges, decreasing to a minimum near the NW center. CTRPL decay curves of the ZnO NWs could be well fitted by a biexponential function where the fast and slow decay lifetime of the PL radiative emission are most likely due to the V_o located on the surface and deeper in the ZnO NWs, respectively.

(4) An analytical model verified by the Hall measurements is derived which can directly calculate the donor concentration of the NWs from the reverse biased I-V characteristics. Similarly, the correlation between the increasing concentration of V_o and Zn_i defects with the increase of the donor concentration and the length of the NW has been observed.

(5) From the field emission properties corresponding to the different kinds of ZnO nanostructures, the leaf-like ZnO nanostructures are most suitable for field emission due to its lowest turn-on and threshold field as well as its relatively high field-enhancement factor.

Based on the above investigation and analysis, the knowledge of the correlation and inter-relationship between the amount and type of native intrinsic defects or doping present in the NWs as their sizes varies is a crucial step towards optimizing and tuning the performances of the ZnO NW based devices. Besides ZnO nanostructures, other nanomaterials also possess these features. Therefore, investigation of the structural parameter with the related devices will be a hot area of research.

7 Extended Works

7.1 Y. G. Fang, C.L. Wang, R. Xu, M. Peterlechner, L.Y. Wen, Y. Mi, G. Wilde, Y. Lei*, Three-dimensional ZnO/$NiMoO_4$ core-shell nanostructures for high-performance supercapacitor. (Submitted)

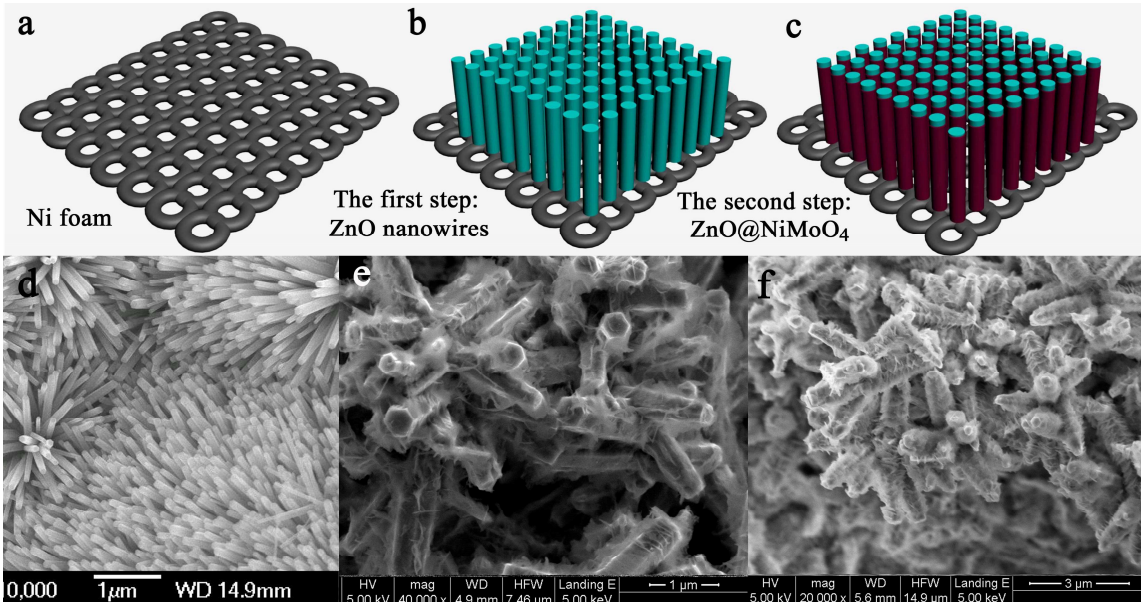

Figure 7.1.1 (a) Schematic illustration of the growth mechanism for ZnO/$NiMoO_4$ core-shell nanostructures. The first step for ZnO nanowires (figure d) and the second step is for ZnO/$NiMoO_4$ core-shell structures via hydrthermal method (figure e and f). (d) ZnO nanowires grown on Ni foam. SEM images of ZnO/$NiMoO_4$ core-shell nanostructures (figure e-f) after different reaction time (1h and 2h).

Compared with other energy storage systems such as batteries and fuel cells, supercapacitors (SCs) are superior in the areas of high power density, fast charge/discharge process, long lifetime, environmental friendliness, and safety. In general, according to the mechanism of the charge storage, SCs can be classified into two kinds: one is electrical double-layer capacitors (EDLCs), whose charges are electrostatically adsorbed at the electrode/electrolyte interface; the other is Faradaic pseudocapacitors that stored energy in electrode materials by redox reactions. Compared with EDLCs, Faradaic pseudocapacitors exhibit higher specific

capacitance via fast and reversible redox reactions.[248] Therefore, much attention have been focused on improving the performance of pseudocapacitors.

In the last few decades, various pseudocapacitive electrode materials, such as transition metal oxides, conducting polymers and binary metal oxides, including MnO_2, NiO, Co_3O_4, $Ni(OH)_2$, $Co(OH)_2$, Polyaniline, Polypyrrole, $NiMoO_4$, $CoMoO_4$, and $MnCo_2O_4$ have been developed to achieve high specific capacitance and energy density.[249-257] The results show that the poor electrical conductivity of transition metal oxides has limited their technological viability and the poor stability of conducting polymers during the charge-discharge cycling has hindered their applications. However, binary metal oxides are considered to be potential materials for high-performance SCs recently because of their feasible oxidation state, high electrical conductivity and stability. Among them, $NiMoO_4$ possesses higher specific capacitance because of its excellent electrochemical performance, low cost, and environmental friendliness. For example, it has been demonstrated that the specific capacitance of $NiMoO_4$ could be as high as 1221.2 F g^{-1} at a current density of 1 A g^{-1}. Daoping Cai and his co-workers[258] synthesized ultrathin mesoporous $NiMoO_4$ nanosheets, which exhibited specific capacitance of 974.4 F g^{-1} at a current density of 1 A g^{-1}. But the cycling stability may be limited due to the work electrode coated carbon black and poly (vinylidene difluoride). Mao-Cheng Liu[253] reported that $CoMoO_4$-$NiMoO_4 \cdot H_2O$ bundles electrode material by a facile chemical co-precipitation method showed higher specific capacitance (1039 Fg^{-1}) than $CoMoO_4$ and a better rate capability than $NiMoO_4 \cdot H_2O$, respectively. However, the conductivity of $CoMoO_4$-$NiMoO_4 \cdot H_2O$ electrode need to be further enhanced. Therefore, it is still a big room to optimize $NiMoO_4$ nanostructures, such as a larger specific area, higher electrical conductivity, and cycle performance on binder-free electrodes.

Research shows that the diffusion distance of electrolytes into the pseudocapacitor electrodes is around 20 nm.[259] In another word, the energy storage mechanism of SCs is widely considered to be a surface phenomenon. Therefore, in order to enhance the electrochemical energy storage properties of SCs, nanostructure engineering is one of the most effective way, because it has advantages of short ion transport pathways and large active surface area. Especially, due to the short ion diffusion distance and low conductivity, rational design of electrode materials, such as three-dimensional (3D) core-shell structure will be an effective strategy for further improving the electrochemical performance. Such a 3D core-shell structure can not only facilitate the electron transport but also the ion diffusion from the electrolyte into the inner active materials by using conductive material as the "core" and active material as the "shell". The thin active material layer makes it possible to fully utilize the active materials and shorten the electron transport distance from the surface to the current collector (the core). However, till now, most of the reports about $NiMoO_4$ were nanowire or nanoflake structures.[260-263] In some literatures, $NiMoO_4$ was even used as the sacrificed conductive core for enhancing the electrochemical performance of other active materials.[264] Similarly, another active material (e.g. Co_3O_4, $NiCo_2O_4$ and $CoMoO_4$ etc.)[250, 253, 254] adopted as the core and $NiMoO_4$ acted as the shell were also reported with view of combining the advantages of the both active materials. Such architectures couldn't fully utilize the advantages of $NiMoO_4$ because of the relative low conductivity and detrimental ionic transport. Here, by using conductive ZnO NWs as the core and $NiMoO_4$ nanoflakes as the active shell material, we will demonstrate that the electrochemical performance of $NiMoO_4$ could be further improved, which could be ascribed to the improvement of the electron transport and ion diffusion between the ZnO NWs core and the thin $NiMoO_4$ shell. The experimental details are shown in figure 7.1.1. 3D ZnO/$NiMoO_4$ nanostructures are fabricated via two-step hydrothermal method in figure 7.1.1e and f.

Figure 7.1.2a shows the typical CV curves of the hierarchical ZnO/$NiMoO_4$ electrodes within the range of -0.10 and 0.65 V (vs. SCE) at the scan rates of 5, 10, 20, 50, and 100 mV s^{-1}, respectively. All of them show a pair of redox peaks, demonstrating that the capacitance characteristics are mainly controlled by Faradaic redox mechanism and the reaction is based on the reversible redox reactions of Ni(II)↔Ni(III) + e^-.

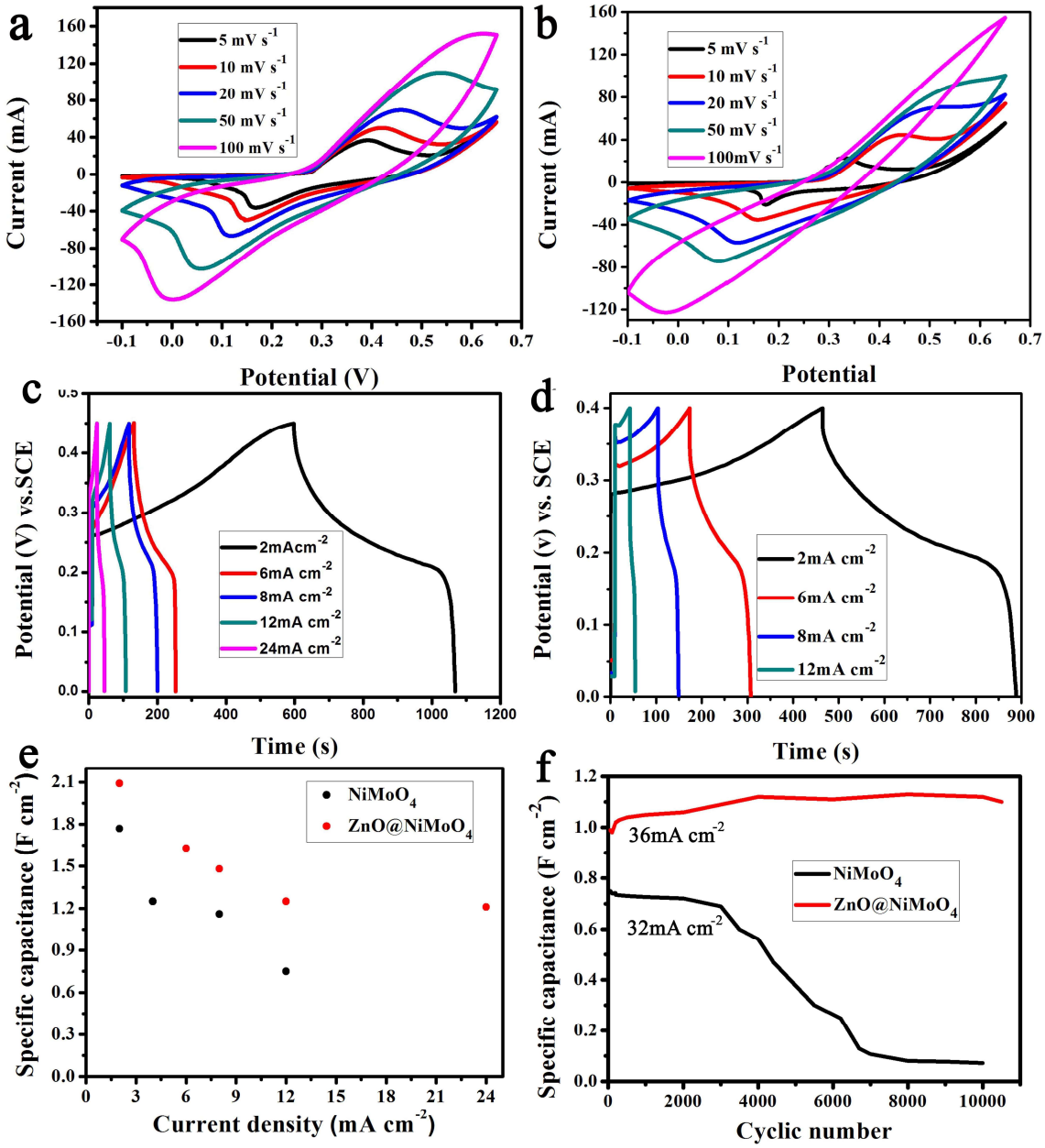

Figure 7.1.2. Cyclic voltammograms of (a) ZnO/$NiMoO_4$ core-shell nanostructures and (b) $NiMoO_4$ nanowires on Ni foam electrode in 2 M NaOH aqueous electrolyte at a scan rate of 5 to 100 mVs^{-1}. Galvanostatic current charge/discharge curves of (c) ZnO/$NiMoO_4$ core-shell nanostructures and (d) $NiMoO_4$ nanowires at different current densities. (e) The specific areal capacitance of ZnO/$NiMoO_4$ and $NiMoO_4$ at different current densities. (f) Cycling performance of the ZnO/$NiMoO_4$ and $NiMoO_4$ electrodes.

Figure 7.1.2b shows the typical cyclic voltammograms (CV) of $NiMoO_4$ nanowires. It is obvious that the CV curves show lower current and smaller CV areas. What's more, the redox peaks become diminishing with increase of the scan rate. These comparisons indicate that the introduction of ZnO scaffolds indeed facilitates the high capacitance and fast charge and discharge performance.

Figure 7.1.2c and d show that the charge-discharge performances of 3D core-shell ZnO/ $NiMoO_4$ electrodes are investigated at various current densities from 2 to 24 mA cm^{-2} at the voltage range of 0 to 0.45 V. Their areal specific capacitances (C_{SP}) at different current densities are calculated in figure 7.1.2e. It is clear that ZnO/$NiMoO_4$ electrodes can deliver high areal capacitance values of 2.09, 1.63, 1.48, 1.25, 1.21F cm^{-2}, and specific capacitance values of 2612.5, 2037.5, 1850, 1562.5, and 1512.5 F g^{-1} at different current densities of 2, 6, 8, 12, 24 mA cm^{-2}, respectively. Remarkably, the areal capacitance values of ZnO/$NiMoO_4$ electrodes still keeps at 1.21 F cm^{-2} (1512.5 F g^{-1}) when the current density is increased to 24 mA cm^{-2}, demonstrating the excellent rate capability. However, without ZnO scaffold, $NiMoO_4$ nanowires electrodes deliver lower areal capacitances are 1.77, 1.25, 1.16, and 0.75 F/cm^{-2} at the current densities of 2, 4, 8, and 12 mA cm^{-2}, respectively (Figure 7.1.2 d). Moreover, under fast charge and discharge conditions, even better enhancement is observed for the hierarchical core-shell nanostructures (e.g. from 1.18 to 1.67 times enhancement at current density of 2 and 12 mA cm^{-2}, respectively).

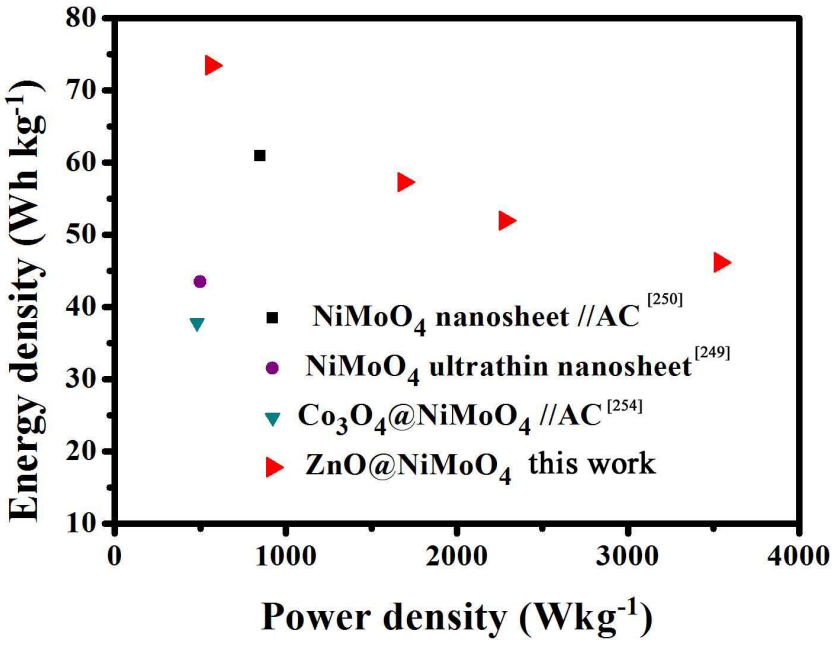

Figure7.1.3. Ragone plots of the ZnO/NiMoO4 electrode material in comparison with the literatures.[260, 261, 265]

In addition, as shown in figure 7.1.3 the max energy density of core-shell ZnO/NiMoO4 nanostructures can reach to 73.5 Wh kg^{-1} at a power density of 565 W kg^{-1}.[260, 261, 265] These results suggest that the hierarchical ZnO/NiMoO4 structures have a high-capacity at a wide range of current densities, terrific rate capability, and stability.

Such enhancement can be ascribed to the larger surface of the active shell material and the conductive core which effectively enhance the rate of ionic and electron transport and shorten the ions diffusion path. These results demonstrate that the 3D core-shell heterostructures by constructing "core" conductive and functional "shell" materials are an efficient route to improve electrochemical properties. It is believed that this kind of core-shell structures has great potential applications in high energy density storage systems.

Besides this part, I also cooperate with my colleagues in other topics, such as sodium-ion batteries and water splitting.

7.2 Vectorial Diffusion for Facile Solution-Processed Self-Assembly of Insoluble Semiconductors: A Case Study on Metal Phthalocyanines

Solution processibility is one of the most intriguing properties of organic semiconductors. However, it is difficult to find a suitable solvent and solution process for most semiconductors. For example, metal phthalocyanines (MPcs) are only soluble in non-volatile solvents, which prevent their applications from solution process. For the first time, vectorial diffusion is utilized for solution processing of MPcs. The obtained large F16CuPc and a-phase CuPc crystals and the efficient phase separation of them suggest the vectorial diffusion process is as slow as a self-assembly process, which is helpful to yield large crystals and purify the semiconductors. This method, which only uses common commercial solvents without any complex and expensive instruments and high-temperature operation, provides a facile approach for purification of organic semiconductors and growth of their crystals in large quantities. (*Chem. Eur. J.* 2014, 20, 2-7)

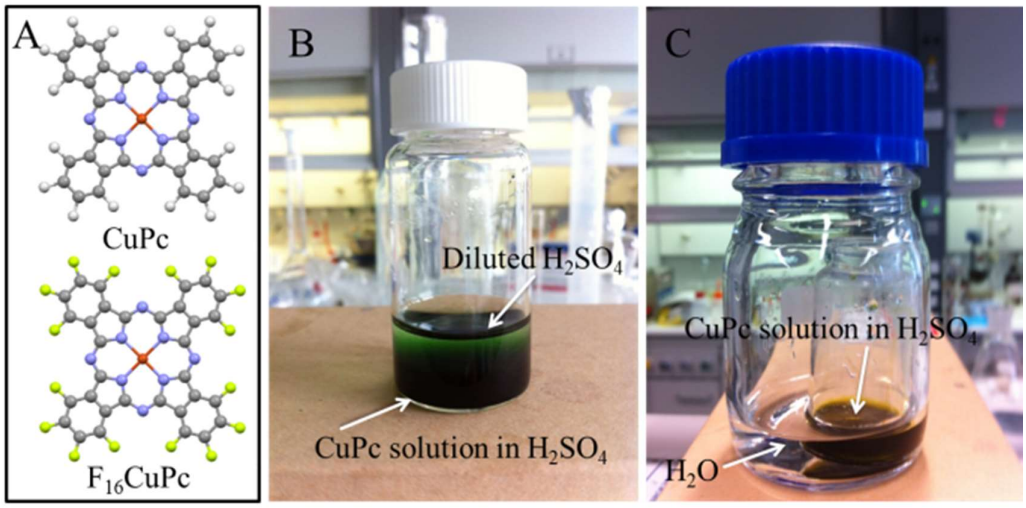

7.3 Manipulation of Disodium Rhodizonate: Factors for Fast-Charge and Fast-Discharge Sodium-Ion Batteries with Long-Term Cyclability

Organic sodium-ion batteries (SIBs) are one of the most promising alternatives of current commercial inorganic lithium-ion batteries (LIBs) especially in the foreseeable large-scale flexible and wearable electronics. However, only a few reports are involving organic SIBs so far. To achieve fast-charge and fast-discharge performance and the long-term cycling suitable

for practical applications, is still challenging. Here, important factors for high performance SIBs especially with high capacity and long-term cyclability under fast-charge and fast-discharge process are investigated. It is found that controlling the solubility through molecular design and determination of the electrochemical window is essential to eliminate dissolution of the electrode material, resulting in improved cyclability. The results show that poly (vinylidenedifl uoride) will decompose during the charge/discharge process, indicating the significance of the binder for achieving high cyclability. Beside of these, it is also shown that decent charge transport and ionic diffusion are beneficial to the fast-charge and fast-discharge batteries. For instance, the flake morphology facilitates the ionic diffusion and thereby can lead to a capacitive effect that is favorable to fast charge and fast discharge. (*Adv. Funct. Mater.* 2016, 26, 1777-1786).

7.4 Extended π−Conjugated System for Fast-Charge and -Discharge Sodium-Ion Batteries

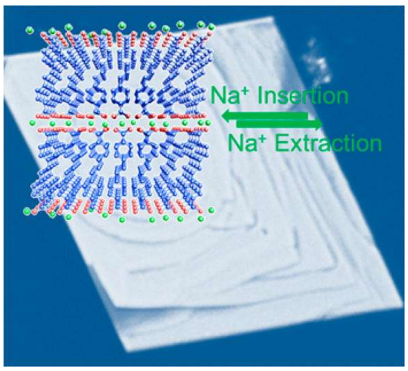

Organic sodium-ion batteries (SIBs) are potential alternatives of current commercial inorganic lithium-ion batteries for portable electronics (especially wear able electronics) because of their low cost and flexibility, making them possible to meet the future flexible and large-scale requirements. However, only a few organic SIBs have been reported so far, and most of them either were tested in a very slow rate or suffered significant performance degradation when cycled under high rate. Here, we are focusing on the molecular design for improving the battery performance and addressing the current challenge of fast-charge and -discharge. Through reasonable molecular design strategy, we demonstrate that the extension of the π -conjugated system is an efficient way to improve the

high rate performance, leading to much enhanced capacity and cyclability with full recovery even after cycled under current density as high as 10 A g^{-1}. (J. Am. Chem. Soc., 2015, 137(8), pp 3124-3130)

7.5 Constructing well-defined AZO/TiO_2 core/shell nanocones with uniformly dispersed Au NPs for enhancing photoelectrochemical water splitting

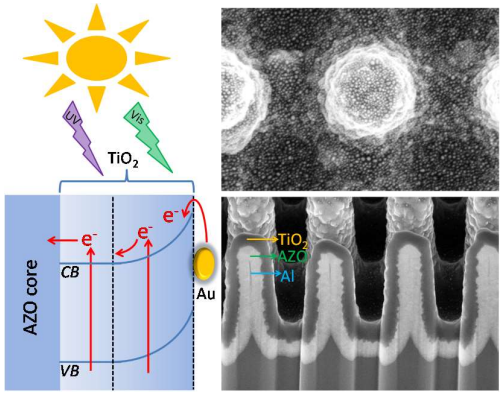

Constructing core/shell nanostructures with optimal structure and composition could maximize the solar light utilization. In this work, using an Al nanocone array as a substrate, well-defined regular array of AZO/TiO_2 core/shell nanocones with uniformly dispersed Au nanoparticles (AZO/TiO_2/Au NCA) is successfully realized through three sequential steps of atomic layer deposition, physical vapor deposition and annealing processes. By tuning the structural and compositional parameters, the advantages of light trapping and short carrier diffusion from the core/shell nanocone array, as well as the surface plasmon resonance and catalytic effects from the Au NPs can be maximally utilized. Accordingly, a remarkable PEC performance could be acquired and the photocurrent density of the AZO/TiO_2/Au NCA electrode reaches up to 1.1 mA/cm^2 at 1.23 V versus RHE under simulated sunlight illumination, which is five times of that from flat AZO/TiO_2 electrode (0.22 mA/cm^2). Moreover, the photocon version of the AZO/TiO_2/Au NCA electrode approaches to 0.73% at 0.21 V versus RHE, which is one of the highest values with the lowest external potential that ever reported in Au/TiO_2 PEC composites. These results demonstrate a feasible route toward scalable fabrication of well-modulated core/shell nanostructures and can be easily applied to other metal/semiconductor composites for high-performance PEC electrodes (*Adv. Energy Mater*. 2016, 6, 1501496).

7.6 Large-scale Highly Ordered Sb Nanorod Arrays Anode with High Capacity and Rate Capability for Sodium-Ion Batteries

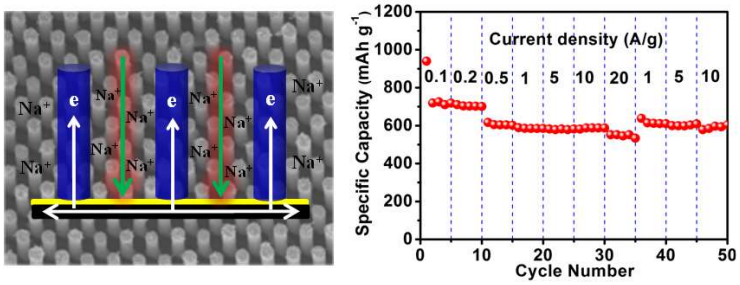

Na-ion batteries are a potential substitute to Li-ion batteries for energy storage devices. However, their poor electrochemical performance, especially capacity and rate capability, is the major bottleneck to future development. Here we propose a performance-oriented electrode structure, which is 1D nanostructure arrays with large-scale high ordering, good vertical alignment, and large interval spacing. Benefiting from these structural merits, a great enhancement in electrochemical performance could be achieved. Taking Sb as an example, we firstly report large-scale highly ordered Sb nanorod arrays with uniform large interval spacing (190 nm). In return for this electrode design, high ion accessibility, fast electron transport, and strong electrode integrity are presented here. Used as additive- and binder-free anodes for Na-ion batteries, Sb nanorod arrays showed a high capacity of 620 mA h g^{-1} at the 100th cycle with a retention of 84% up to 250 cycles at 0.2 A g^{-1}, and a superior rate capability for delivering reversible capacities of 579.7 and 557.7 mA h g^{-1} at 10 and 20 A g^{-1}, respectively. A full cell coupled by a P_2-$Na_{2/3}Ni_{1/3}Mn_{2/3}O_2$ cathode and a Sb nanorod array anode was also constructed, which showed good cycle performance up to 250 cycles, high rate capability up to 20 A g^{-1}, and large energy density up to 130 Wh kg^{-1}. These excellent electrochemical performances shall pave the way for developing more applications of Sb nanorod arrays in energy storage devices *(Energy Environ. Sci., 2015, 8, 2954-2962).*

Bibliography

[1]. Özgür HMaUm. ZnO Fundamentals, Materials and Device Technology: Wiley-VCH; 2007.
[2]. S. M. Sze and K. K. Ng. Physics of Semiconductor Devices: Wiley, New York, 3rd edn, 2007.
[3]. Zhang Z, Meng G, Wu Q, et al. Enhanced cold field emission of large-area arrays of vertically aligned ZnO-nanotapers via sharpening: experiment and theory. *Scientific reports* 2014; **4**: 4676.
[4]. Zhao CX, Li YF, Zhou J, et al. Large-Scale Synthesis of Bicrystalline ZnO Nanowire Arrays by Thermal Oxidation of Zinc Film: Growth Mechanism and High-Performance Field Emission. *Crystal Growth & Design* 2013; **13**(7): 2897-905.
[5]. Naik KK, Khare R, Chakravarty D, et al. Field emission properties of ZnO nanosheet arrays. *Applied Physics Letters* 2014; **105**(23): 233101.
[6]. Wang ZL. The new field of nanopiezotronics. *Materials Today* 2007; **10**(5): 20-8.
[7]. Wang ZL. Zinc oxide nanostructures: growth, properties and applications. *Journal of Physics: Condensed Matter* 2004; **16**(25): R829-R58.
[8]. Yu R, Niu S, Pan C, Wang ZL. Piezotronic effect enhanced performance of Schottky-contacted optical, gas, chemical and biological nanosensors. *Nano Energy* 2015; **14**: 312-39.
[9]. Zhou R, Hu G, Yu R, Pan C, Wang ZL. Piezotronic effect enhanced detection of flammable/toxic gases by ZnO micro/nanowire sensors. *Nano Energy* 2015; **12**: 588-96.
[10]. Tonezzer M, Dang TTL, Bazzanella N, Nguyen VH, Iannotta S. Comparative gas-sensing performance of 1D and 2D ZnO nanostructures. *Sensors and Actuators B: Chemical* 2015; **220**: 1152-60.
[11]. Chen TP, Chang SP, Hung FY, Chang SJ, Hu ZS, Chen KJ. Simple fabrication process for 2D ZnO nanowalls and their potential application as a methane sensor. *Sensors* 2013; **13**(3): 3941-50.
[12]. Lv R, Wang T, Su F, Zhang P, Li C, Gong J. Facile synthesis of ZnO nanopencil arrays for photoelectrochemical water splitting. *Nano Energy* 2014; **7**: 143-50.
[13]. Liu M, Nam C-Y, Black CT, Kamcev J, Zhang L. Enhancing Water Splitting Activity and Chemical Stability of Zinc Oxide Nanowire Photoanodes with Ultrathin Titania Shells. *The Journal of Physical Chemistry C* 2013; **117**(26): 13396-402.
[14]. Kim S, Na S, Jeon H, et al. Effects of Sn doping on the growth morphology and electrical properties of ZnO nanowires. *Nanotechnology* 2013; **24**(6): 065703.
[15]. Motaung DE, Makgwane PR, Ray SS. Induced ferromagnetic and gas sensing properties in ZnO-nanostructures by altering defect concentration of oxygen and zinc vacancies. *Materials Letters* 2015; **139**: 475-9.
[16]. Kushwaha A, Aslam M. Defect controlled water splitting characteristics of gold nanoparticle functionalized ZnO nanowire films. *RSC Advances* 2014; **4**(40): 20955.
[17]. Kayaci F, Vempati S, Donmez I, Biyikli N, Uyar T. Role of zinc interstitials and oxygen vacancies of ZnO in photocatalysis: a bottom-up approach to control defect density. *Nanoscale* 2014; **6**(17): 10224-34.
[18]. Kushwaha A, Aslam M. Enhanced electrical conductivity and reduced defect emissions of ZnO:Mo nanowire array films. 2013: 240-1.
[19]. Wang N, Cai Y, Zhang RQ. Growth of nanowires. *Materials Science and Engineering: R: Reports* 2008; **60**(1-6): 1-51.
[20]. Özgür U, Alivov YI, Liu C, et al. A comprehensive review of ZnO materials and devices. *Journal of Applied Physics* 2005; **98**(4): 041301.

[21]. Pearton SDPN, K.Ip ,Y.W. Heo, T. Steiner Recent progress in processing and properties of ZnO. *Progress in Materials Science* 2005; **50**(3): 293-340.
[22]. Schmidt-Mende L, MacManus-Driscoll JL. ZnO–nanostructures, defects, and devices. *Materials Today* 2007; **10**(5): 40-8.
[23]. https://en.wikipedia.org/wiki/Zinc_oxide.
[24]. Olga Dulub LAB, Ulrike Diebold. STM study of the geometric and electronic structure of ZnO(0001)-Zn, (0001)-O, (10110), and (1120) surfaces. *Surface Science* 2002; **519**(201-217).
[25]. Meyer B, Marx D. Density-functional study of the structure and stability of ZnO surfaces. *Physical Review B* 2003; **67**(3).
[26]. Lu Z, Fa JG. Zinc Oxide Nanostructures: Synthesis and Properties. *J Nanosci Nanotechnol* 2005; **5(10)**(1561-73).
[27]. Olsen L,GaJS. The High-Pressure Phase of Zincite. *J Synchrotron Rad* 1995; **2**: 233-5.
[28]. Ding Y, Kong XY, Wang ZL. Doping and planar defects in the formation of single-crystal ZnO nanorings. *Physical Review B* 2004; **70**(23).
[29]. Staemmler V, Fink K, Meyer B, et al. Stabilization of polar ZnO surfaces: validating microscopic models by using CO as a probe molecule. *Physical review letters* 2003; **90**(10): 106102.
[30]. Dulub O, Diebold U, Kresse G. Novel stabilization mechanism on polar surfaces: ZnO(0001)-Zn. *Physical review letters* 2003; **90**(1): 016102.
[31]. Coleman VA, Jagadish C. Basic Properties and Applications of ZnO. 2006: 1-20.
[32]. Woll C. The chemistry and physics of zinc oxide surfaces. *Progress in Surface Science* 2007; **82**(2-3): 55-120.
[33]. Fan HJ, Fuhrmann B, Scholz R, et al. Vapour-transport-deposition growth of ZnO nanostructures: switch between c-axial wires and a-axial belts by indium doping. *Nanotechnology* 2006; **17**(11): S231-S9.
[34]. Djurisic AB, Leung YH. Optical properties of ZnO nanostructures. *Small* 2006; **2**(8-9): 944-61.
[35]. Xiong H-M. Photoluminescent ZnO nanoparticles modified by polymers. *Journal of Materials Chemistry* 2010; **20**(21): 4251.
[36]. Wang R-C, Liu C-P, Huang J-L, Chen S-J. ZnO symmetric nanosheets integrated with nanowalls. *Applied Physics Letters* 2005; **87**(5): 053103.
[37]. Greene LE, Law M, Goldberger J, et al. *Angewandte Chemie* 2003; **115**(26): 3139-42.
[38]. Fan HJ, Scholz R, Kolb FM, Zacharias M. Two-dimensional dendritic ZnO nanowires from oxidation of Zn microcrystals. *Applied Physics Letters* 2004; **85**(18): 4142.
[39]. Fan HJ, Scholz R, Kolb FM, et al. On the growth mechanism and optical properties of ZnO multi-layer nanosheets. *Applied Physics A* 2004; **79**(8).
[40]. Meng XQ, Shen DZ, Zhang JY, et al. The structural and optical properties of ZnO nanorod arrays. *Solid State Communications* 2005; **135**(3): 179-82.
[41]. Ng HT, Chen B, Li J, et al. Optical properties of single-crystalline ZnO nanowires on m-sapphire. *Applied Physics Letters* 2003; **82**(13): 2023.
[42]. Chen Z, Wu N, Shan Z, et al. Effect of N_2 flow rate on morphology and structure of ZnO nanocrystals synthesized via vapor deposition. *Scripta Materialia* 2005; **52**(1): 63-7.
[43]. Zhao D, Andreazza C, Andreazza P, Ma J, Liu Y, Shen D. Temperature-dependent growth mode and photoluminescence properties of ZnO nanostructures. *Chemical Physics Letters* 2004; **399**(4-6): 522-6.
[44]. Lisheng Huang SW, ‡ Shaoguang Yang, Dezhen Shen, Benxi Gu, and Youwei Du. ZnO Well-Faceted Fibers with Periodic Junctions. *J Phys Chem B* 2004; **108**: 19901-3.

[45]. Wen F, Li W, Moon J-H, Kim JH. Hydrothermal synthesis of ZnO:Zn with green emission at low temperature with reduction process. *Solid State Communications* 2005; **135**(1-2): 34-7.
[46]. Yang Q, Tang K, Zuo J, Qian Y. Synthesis and luminescent property of single-crystal ZnO nanobelts by a simple low temperature evaporation route. *Applied Physics A* 2004; **79**(8).
[47]. Wang F, Ye Z, Ma D, Zhu L, Zhuge F. Rapid synthesis and photoluminescence of novel ZnO nanotetrapods. *Journal of Crystal Growth* 2005; **274**(3-4): 447-52.
[48]. Choopun S, Hongsith N, Tanunchai S, et al. Single-crystalline ZnO nanobelts by RF sputtering. *Journal of Crystal Growth* 2005; **282**(3-4): 365-9.
[49]. Weidong Yu XL, and Xiangdong Gao. Catalytic Synthesis and Structural Characteristics of High-Quality Tetrapod-Like ZnO Nanocrystals by a Modified Vapor Transport Process. *CRYSTAL GROWTH &DESIGN* 2005; **5**(1): 151-5.
[50]. Park WI, Jun YH, Jung SW, Yi G-C. Excitonic emissions observed in ZnO single crystal nanorods. *Applied Physics Letters* 2003; **82**(6): 964.
[51]. Lin B, Fu Z, Jia Y. Green luminescent center in undoped zinc oxide films deposited on silicon substrates. *Applied Physics Letters* 2001; **79**(7): 943.
[52]. P.S. Xu*, Y.M. Sun, C.S. Shi, F.Q. Xu, H.B. Pan. The electronic structure and spectral properties of ZnO and its defects. *Nuclear Instruments and Methods in Physics Research* 2003; **100**: 286-90
[53]. S.A.M. Lima FAS, M. Jafelicci Jr, M.R. Davolos. Luminescent properties and lattice defects correlation on zinc oxide. *International Journal of Inorganic Materials* 2001; **3**: 749-54.
[54]. Kobayashi A, Sankey OF, Dow JD. Deep energy levels of defects in the wurtzite semiconductors AIN, CdS, CdSe, ZnS, and ZnO. *Physical Review B* 1983; **28**(2): 946-56.
[55]. HAGEMARK KI. Defect Structure of Zn-Doped ZnO. *JOURNAL OF SOLID STATE CHEMISTRY* 1976; **16**: 293-9
[56]. Janotti A, Van de Walle CG. New insights into the role of native point defects in ZnO. *Journal of Crystal Growth* 2006; **287**(1): 58-65.
[57]. Sokol AA, French SA, Bromley ST, Catlow CRA, van Dam HJJ, Sherwood P. Point defects in ZnO. *Faraday Discuss* 2007; **134**: 267-82.
[58]. Ahn CH, Kim YY, Kim DC, Mohanta SK, Cho HK. A comparative analysis of deep level emission in ZnO layers deposited by various methods. *Journal of Applied Physics* 2009; **105**(1): 013502.
[59]. Cao B, Cai W, Zeng H. Temperature-dependent shifts of three emission bands for ZnO nanoneedle arrays. *Applied Physics Letters* 2006; **88**(16): 161101.
[60]. Zeng H, Li Z, Cai W, Liu P. Strong localization effect in temperature dependence of violet-blue emission from ZnO nanoshells. *Journal of Applied Physics* 2007; **102**(10): 104307.
[61]. Bylander EG. Surface effects on the low-energy cathodoluminescence of zinc oxide. *Journal of Applied Physics* 1978; **49**(3): 1188.
[62]. Vlasenko LS, Watkins GD. Optical detection of electron paramagnetic resonance in room-temperature electron-irradiated ZnO. *Physical Review B* 2005; **71**(12).
[63]. Wu XL, Siu GG, Fu CL, Ong HC. Photoluminescence and cathodoluminescence studies of stoichiometric and oxygen-deficient ZnO films. *Applied Physics Letters* 2001; **78**(16): 2285.
[64]. https://en.wikipedia.org/wiki/Doping.
[65]. Rahm A, Yang GW, Lorenz M, et al. Two-dimensional ZnO:Al nanosheets and nanowalls obtained by Al2O3-assisted carbothermal evaporation. *Thin Solid Films* 2005; **486**(1-2): 191-4.

[66]. Wang R-C, Liu C-P, Huang J-L, Chen S-J. Single-crystalline AlZnO nanowires/nanotubes synthesized at low temperature. *Applied Physics Letters* 2006; **88**(2): 023111.
[67]. Li SY, Lin P, Lee CY, Tseng TY, Huang CJ. Effect of Sn dopant on the properties of ZnO nanowires. *Journal of Physics D: Applied Physics* 2004; **37**(16): 2274-82.
[68]. Seung Yong Bae CWN, Ja Hee Kang, and Jeunghee Park. Comparative Structure and Optical Properties of Ga-, In-, and Sn-Doped ZnO Nanowires Synthesized via Thermal Evaporation. *J Phys Chem B* 2005; **109**: 2526-31.
[69]. Chen YW, Liu YC, Lu SX, et al. Optical properties of ZnO and ZnO:In nanorods assembled by sol-gel method. *The Journal of chemical physics* 2005; **123**(13): 134701.
[70]. Li QH, Wan Q, Wang YG, Wang TH. Abnormal temperature dependence of conductance of single Cd-doped ZnO nanowires. *Applied Physics Letters* 2005; **86**(26): 263101.
[71]. Xu CX, Sun XW, Zhang XH, Ke L, Chua SJ. Photoluminescent properties of copper-doped zinc oxide nanowires. *Nanotechnology* 2004; **15**(7): 856-61.
[72]. Zhou S-M, Zhang X-H, Meng X-M, et al. The fabrication and optical properties of highly crystalline ultra-long Cu-doped ZnO nanowires. *Nanotechnology* 2004; **15**(9): 1152-5.
[73]. Liu LQ, Xiang B, Zhang XZ, Zhang Y, Yu DP. Synthesis and room temperature ferromagnetism of FeCo-codoped ZnO nanowires. *Applied Physics Letters* 2006; **88**(6): 063104.
[74]. Yang LW, Wu XL, Huang GS, Qiu T, Yang YM. In situ synthesis of Mn-doped ZnO multileg nanostructures and Mn-related Raman vibration. *Journal of Applied Physics* 2005; **97**(1): 014308.
[75]. Liu JJ, Yu MH, Zhou WL. Well-aligned Mn-doped ZnO nanowires synthesized by a chemical vapor deposition method. *Applied Physics Letters* 2005; **87**(17): 172505.
[76]. Jr H. He CSL, Lih J. Chen, Dragomir Davidovic, and Zhong L. Wang. Large-Scale Ni-Doped ZnO Nanowire Arrays and Electrical and Optical Properties. *J AM CHEM SOC* 2005; **127**: 16376-7
[77]. Lee W, Jeong M-C, Myoung J-M. Optical characteristics of arsenic-doped ZnO nanowires. *Applied Physics Letters* 2004; **85**(25): 6167.
[78]. Wei H, Wu Y, wu L, Hu C. Preparation and photoluminescence of surface N-doped ZnO nanocrystal. *Materials Letters* 2005; **59**(2-3): 271-5.
[79]. Wang B, Callahan MJ, Bouthillette LO, Xu C, Suscavage MJ. Hydrothermal growth and characterization of nitrogen-doped ZnO crystals. *Journal of Crystal Growth* 2006; **287**(2): 381-5.
[80]. Shen G, Cho JH, Jung SI, Lee CJ. Synthesis and characterization of S-doped ZnO nanowires produced by a simple solution-conversion process. *Chemical Physics Letters* 2005; **401**(4-6): 529-33.
[81]. Guozhen Shen JHC, Jin Kyoung Yoo, Gyu-Chul Yi, and Cheol Jin Lee. Synthesis and Optical Properties of S-Doped ZnO Nanostructures: Nanonails and Nanowires. *J Phys Chem B* 2005; **109**: 5491-6.
[82]. Ishizumi A, Kanemitsu Y. Structural and luminescence properties of Eu-doped ZnO nanorods fabricated by a microemulsion method. *Applied Physics Letters* 2005; **86**(25): 253106.
[83]. Wang FR, Su YY, Liu JK, Wu Y. Enhanced photoelectric properties by the coordinating role of doping and modification. *Physical chemistry chemical physics : PCCP* 2016; **18**(6): 4850-9.

[84]. Woo H-S, Kwak C-H, Chung J-H, Lee J-H. Highly selective and sensitive xylene sensors using Ni-doped branched ZnO nanowire networks. *Sensors and Actuators B: Chemical* 2015; **216**: 358-66.
[85]. Wang B, Ren T, Chen S, et al. Resistive switching in Ga- and Sb-doped ZnO single nanowire devices. *J Mater Chem C* 2015; **3**(45): 11881-5.
[86]. Pauporte T, Lupan O, Zhang J, et al. Low-Temperature Preparation of Ag-Doped ZnO Nanowire Arrays, DFT Study, and Application to Light-Emitting Diode. *ACS Appl Mater Interfaces* 2015; **7**(22): 11871-80.
[87]. Patel PP, Hanumantha PJ, Velikokhatnyi OI, et al. Nitrogen and cobalt co-doped zinc oxide nanowires–Viable photoanodes for hydrogen generation via photoelectrochemical water splitting. *Journal of Power Sources* 2015; **299**: 11-24.
[88]. Chang Y-C. Ni-doped ZnO nanotower arrays with enhanced optical and field emission properties. *RSC Adv* 2014; **4**(99): 56241-7.
[89]. Chang LT, Wang CY, Tang J, et al. Electric-field control of ferromagnetism in Mn-doped ZnO nanowires. *Nano letters* 2014; **14**(4): 1823-9.
[90]. Hongfeng Duan HH, Luwei Sun, Shiyan Song and Zhizhen Ye. Indium-doped ZnO nanowires with infrequent growth orientation, rough surfaces and low-density surface traps. *Nanoscale research letters* 2013; **8**(493).
[91]. Qiu Y, Yan K, Deng H, Yang S. Secondary branching and nitrogen doping of ZnO nanotetrapods: building a highly active network for photoelectrochemical water splitting. *Nano letters* 2012; **12**(1): 407-13.
[92]. Mahmood K, Park SB. Growth and conductivity enhancement of N-doped ZnO nanorod arrays. *Journal of Crystal Growth* 2012; **347**(1): 104-12.
[93]. Lin YG, Hsu YK, Chen YC, Chen LC, Chen SY, Chen KH. Visible-light-driven photocatalytic carbon-doped porous ZnO nanoarchitectures for solar water-splitting. *Nanoscale* 2012; **4**(20): 6515-9.
[94]. Wang D, Xing G, Gao M, Yang L, Yang J, Wu T. Defects-Mediated Energy Transfer in Red-Light-Emitting Eu-Doped ZnO Nanowire Arrays. *The Journal of Physical Chemistry C* 2011; **115**(46): 22729-35.
[95]. Zhao C, Chen A, Ji X, et al. Growth of vertically aligned ZnO nanowire arrays on ZnO single crystals. *Materials Letters* 2015; **154**: 40-3.
[96]. P. X. Gao YD, and Z. L. Wang. Crystallographic Orientation-Aligned ZnO Nanorods Grown by a Tin Catalyst. *Nano Lett,* 2003; **3**(9): 1315-20.
[97]. Ashfold MNR, Doherty RP, Ndifor-Angwafor NG, Riley DJ, Sun Y. The kinetics of the hydrothermal growth of ZnO nanostructures. *Thin Solid Films* 2007; **515**(24): 8679-83.
[98]. Sun Y, George Ndifor-Angwafor N, Jason Riley D, Ashfold MNR. Synthesis and photoluminescence of ultra-thin ZnO nanowire/nanotube arrays formed by hydrothermal growth. *Chemical Physics Letters* 2006; **431**(4-6): 352-7.
[99]. Guo M, Diao P, Cai S. Hydrothermal growth of well-aligned ZnO nanorod arrays: Dependence of morphology and alignment ordering upon preparing conditions. *Journal of Solid State Chemistry* 2005; **178**(6): 1864-73.
[100]. Zhang Z, Lv Y, Yan J, et al. Uniform ZnO nanowire arrays: Hydrothermal synthesis, formation mechanism and field emission performance. *Journal of Alloys and Compounds* 2015; **650**: 374-80.
[101]. Elias J, Tena-Zaera R, Lévy-Clément C. Electrochemical deposition of ZnO nanowire arrays with tailored dimensions. *Journal of Electroanalytical Chemistry* 2008; **621**(2): 171-7.
[102]. Qiu J, Guo M, Feng Y, Wang X. Electrochemical deposition of branched hierarchical ZnO nanowire arrays and its photoelectrochemical properties. *Electrochimica Acta* 2011; **56**(16): 5776-82.

[103]. Liu Z, E L, Ya J, Xin Y. Growth of ZnO nanorods by aqueous solution method with electrodeposited ZnO seed layers. *Applied Surface Science* 2009; **255**(12): 6415-20.
[104]. Chander R, Raychaudhuri AK. Electrodeposition of aligned arrays of ZnO nanorods in aqueous solution. *Solid State Communications* 2008; **145**(1-2): 81-5.
[105]. Kumar N, Srivastava AK, Nath R, Gupta BK, Varma GD. Probing the highly efficient room temperature ammonia gas sensing properties of a luminescent ZnO nanowire array prepared via an AAO-assisted template route. *Dalton transactions* 2014; **43**(15): 5713-20.
[106]. Sharma SK, Rammohan A, Sharma A. Templated one step electrodeposition of high aspect ratio n-type ZnO nanowire arrays. *Journal of colloid and interface science* 2010; **344**(1): 1-9.
[107]. Wang L, Zhang X, Zhao S, Zhou G, Zhou Y, Qi J. Synthesis of well-aligned ZnO nanowires by simple physical vapor deposition on c-oriented ZnO thin films without catalysts or additives. *Applied Physics Letters* 2005; **86**(2): 024108.
[108]. Wang JS, Yang CS, Chen PI, et al. Catalyst-free highly vertically aligned ZnO nanoneedle arrays grown by plasma-assisted molecular beam epitaxy. *Applied Physics A* 2009; **97**(3): 553-7.
[109]. Chao L-C, Tsai S-Y, Lin C-N, Liau C-C, Ye C-C. Vertically aligned ZnO nanowires prepared by thermal oxidation of RF magnetron sputtered metallic zinc films. *Materials Science in Semiconductor Processing* 2013; **16**(5): 1316-20.
[110]. https://en.wikipedia.org/wiki/Chemical_vapor_deposition.
[111]. Wang PXGaZL. Substrate Atomic-Termination-Induced Anisotropic Growth of ZnO Nanowires/Nanorods by the VLS Process. *J Phys Chem B* 2004; **108**: 7534-7.
[112]. https://en.wikipedia.org/wiki/Hydrothermal_synthesis.
[113]. Vayssieres L. Growth of Arrayed Nanorods and Nanowires of ZnO from Aqueous Solutions. *Adv Mater,* 2003; **15**(5): 464-6.
[114]. Wen L, Shao Z, Fang Y, et al. Selective growth and piezoelectric properties of highly ordered arrays of vertical ZnO nanowires on ultrathin alumina membranes. *Applied Physics Letters* 2010; **97**(5): 053106.
[115]. Lei Y, Cai W, Wilde G. Highly ordered nanostructures with tunable size, shape and properties: A new way to surface nano-patterning using ultra-thin alumina masks. *Progress in Materials Science* 2007; **52**(4): 465-539.
[116]. Li L, Zhai T, Zeng H, Fang X, Bando Y, Golberg D. Polystyrene sphere-assisted one-dimensional nanostructure arrays: synthesis and applications. *J Mater Chem* 2011; **21**(1): 40-56.
[117]. Fan HJ, Werner P, Zacharias M. Semiconductor nanowires: from self-organization to patterned growth. *Small* 2006; **2**(6): 700-17.
[118]. https://en.wikipedia.org/wiki/Electrophoretic_deposition.
[119]. Sheng Xu YW, Melanie Kirkham, Jin Liu, Wenjie Mai,† Dragomir Davidovic,, Robert L. Snyder aZLW. Patterned Growth of Vertically Aligned ZnO Nanowire Arrays on Inorganic Substrates at Low Temperature without Catalyst. *J Am Chem Soc,* 2008; **130**(45).
[120]. Wang ZL. Nanostructures of zinc oxide. *Materials Today* 2004; **7**(6): 26-33.
[121]. Li Z, Fang Y, Peng L, Pan D, Wu M. EDTA-assisted synthesis of rose-like ZnO architectures. *Crystal Research and Technology* 2010; **45**(10): 1083-6.
[122]. Kołodziejczak-Radzimska A, Jesionowski T. Zinc Oxide-From Synthesis to Application: A Review. *Materials* 2014; **7**(4): 2833-81.
[123]. https://en.wikipedia.org/wiki/Field_electron_emission.
[124]. Zurita BZ. Development of Transparent and Flexible Field Emission Displays Using ZnO Films: Nagoya Institute of Technology Repository; 2015.

[125]. Ghosh D, Ghosh P, Tanemura M, et al. Highly transparent and flexible field emission devices based on single-walled carbon nanotube films. *Chemical communications* 2011; **47**(17): 4980-2.
[126]. Choi WB, Chung DS, Kang JH, et al. Fully sealed, high-brightness carbon-nanotube field-emission display. *Applied Physics Letters* 1999; **75**(20): 3129.
[127]. Wang B, Zheng Z, Wu H, Zhu L. Field emission properties and growth mechanism of In2O3 nanostructures. *Nanoscale research letters* 2014; **9**(1): 111.
[128]. Au FCK, Wong KW, Tang YH, Zhang YF, Bello I, Lee ST. Electron field emission from silicon nanowires. *Applied Physics Letters* 1999; **75**(12): 1700.
[129]. He JH, Wu TH, Hsin CL, et al. Beaklike SnO_2 nanorods with strong photoluminescent and field-emission properties. *Small* 2006; **2**(1): 116-20.
[130]. Lu D, Ogino A, Liang B, Liu J, Nagatsu M. Field-Emission Properties of Nanostructured WO_3 Arrays Fabricated Using Tungsten Hot-Filament Chemical Vapor Deposition. *Japanese Journal of Applied Physics* 2009; **48**(9): 090206.
[131]. Jeong JS, Lee JY, Cho HK. Investigation of 2D/3D defects in controlled-growth oxygen-deficient ZnO nanowires and their field emission. *Chemical Physics Letters* 2011; **503**(4-6): 266-71.
[132]. Singh DP. Synthesis and Growth of ZnO Nanowires. *Science of Advanced Materials* 2010; **2**(3): 245-72.
[133]. Zhao CX, Huang K, Deng SZ, Xu NS, Chen J. Investigation of the effects of atomic oxygen exposure on the electrical and field emission properties of ZnO nanowires. *Applied Surface Science* 2013; **270**: 82-9.
[134]. Chen S, Chen J, Liu J, Qi J, Wang Y. The effect of high-temperature oxygen annealing on field emission from ZnO nanowire arrays. *Applied Surface Science* 2015; **357**: 413-6.
[135]. Yung-Kuan Tseng C-JH, Hsin-Min Cheng, I-Nan Lin, Kuo-Shung Liu, and I-Cherng Chen. Characterization and field-Emission Properties of Needle-Like Zinc Oxide Nanowires Grown Vertically on Conductive Zinc Oxide Films. *Adv, Funct, Mater* 2013; **13**(811-814).
[136]. Zhao CX, Li YF, Chen YC, et al. Microstructure change of ZnO nanowire induced by energetic x-ray radiation and its effect on the field emission properties. *Nanotechnology* 2013; **24**(27): 275703.
[137]. Chen D, Song X, Zhang Z, et al. Transmission type flat-panel X-ray source using ZnO nanowire field emitters. *Applied Physics Letters* 2015; **107**(24): 243105.
[138]. Cui Y, Zhang X, Lei W, Di Y, Wang J, Yang X. Effect of ion bombardment on the field emission property of tetrapod ZnO. *Journal of Applied Physics* 2010; **107**(5): 054506.
[139]. Yunhua Huang YZ, Yousong Gu, Xuedong Bai, Junjie Qi, Qingliang Liao, and Juan Liu. Field Emission of a Single In-Doped ZnO Nanowire. *J Phys Chem C* 2007; **111**(9039-9043).
[140]. Ahmad M, Sun H, Zhu J. Enhanced photoluminescence and field-emission behavior of vertically well aligned arrays of In-doped ZnO Nanowires. *ACS Appl Mater Interfaces* 2011; **3**(4): 1299-305.
[141]. Garry S, McCarthy E, Mosnier JP, McGlynn E. Influence of ZnO nanowire array morphology on field emission characteristics. *Nanotechnology* 2014; **25**(13): 135604.
[142]. https://en.wikipedia.org/wiki/Photoelectrochemistry.
[143]. Shao M, Ning F, Wei M, Evans DG, Duan X. Hierarchical Nanowire Arrays Based on ZnO Core-Layered Double Hydroxide Shell for Largely Enhanced Photoelectrochemical Water Splitting. *Advanced Functional Materials* 2014; **24**(5): 580-6.

[144]. Zhang X, Liu Y, Kang Z. 3D branched ZnO nanowire arrays decorated with plasmonic au nanoparticles for high-performance photoelectrochemical water splitting. *ACS Appl Mater Interfaces* 2014; **6**(6): 4480-9.
[145]. Wang ZL. Piezopotential gated nanowire devices: Piezotronics and piezo-phototronics. *Nano Today* 2010; **5**(6): 540-52.
[146]. Pan C, Chen M, Yu R, et al. Progress in Piezo-Phototronic-Effect-Enhanced Light-Emitting Diodes and Pressure Imaging. *Advanced materials* 2016; **28**(8): 1535-52.
[147]. https://en.wikipedia.org/wiki/Powder_diffraction.
[148]. Qiu J, Li X, He W, et al. The growth mechanism and optical properties of ultralong ZnO nanorod arrays with a high aspect ratio by a preheating hydrothermal method. *Nanotechnology* 2009; **20**(15): 155603.
[149]. Lord AM, Maffeis TG, Allen MW, et al. Surface state modulation through wet chemical treatment as a route to controlling the electrical properties of ZnO nanowire arrays investigated with XPS. *Applied Surface Science* 2014; **320**: 664-9.
[150]. Yang X-J, Miao X-Y, Xu X-L, Xu C-M, Xu J, Liu H-T. Structure, X-ray photoelectron spectroscopy and photoluminescence properties of highly ordered ZnO microrods. *Optical Materials* 2005; **27**(10): 1602-5.
[151]. Al-Gaashani R, Radiman S, Daud AR, Tabet N, Al-Douri Y. XPS and optical studies of different morphologies of ZnO nanostructures prepared by microwave methods. *Ceramics International* 2013; **39**(3): 2283-92.
[152]. Maffeis TGG, Penny MW, Castaing A, Guy OJ, Wilks SP. XPS investigation of vacuum annealed vertically aligned ultralong ZnO nanowires. *Surface Science* 2012; **606**(1-2): 99-103.
[153]. Dongseok Park YT, Jaehyun Kim and Kijung Yong. LOW-TEMPERATURE SYNTHESIZED ZnO NANONEEDLES: XPS AND PL ANALYSIS. *Surface Review and Letters* 2007; **14**(1061-1065).
[154]. Walker TGLLY, A. Wadeasa, S. U. Ali, M. H. Asif, Q. X. Zhao and O. Nur. Zinc oxide nanowires: controlled low temperature growth and some electrochemical and optical nano-devices. *Journal of Materials Chemistry* 2009; **2009**(19): 1006-18.
[155]. Han X, Wang G, Wang Q, et al. Ultraviolet lasing and time-resolved photoluminescence of well-aligned ZnO nanorod arrays. *Applied Physics Letters* 2005; **86**(22): 223106.
[156]. https://en.wikipedia.org/wiki/Hall_effect.
[157]. Chang J, Dommer M, Chang C, Lin L. Piezoelectric nanofibers for energy scavenging applications. *Nano Energy* 2012; **1**(3): 356-71.
[158]. Chang Y-C. Low temperature growth of ZnO nanowire arrays with enhanced high performance photocatalytic activity and reusability. *Catalysis Communications* 2014; **56**: 45-9.
[159]. Kuo T-J, Lin C-N, Kuo C-L, Huang MH. Growth of Ultralong ZnO Nanowires on Silicon Substrates by Vapor Transport and Their Use as Recyclable Photocatalysts. *Chemistry of Materials* 2007; **19**(21): 5143-7.
[160]. Anantachaisilp S, Smith SM, Ton-That C, Osotchan T, Moon AR, Phillips MR. Tailoring Deep Level Surface Defects in ZnO Nanorods for High Sensitivity Ammonia Gas Sensing. *The Journal of Physical Chemistry C* 2014; **118**(46): 27150-6.
[161]. Zhang Q, Dandeneau CS, Zhou X, Cao G. ZnO Nanostructures for Dye-Sensitized Solar Cells. *Advanced materials* 2009; **21**(41): 4087-108.
[162]. Gao M, Li W, Liu Y, Li Q, Chen Q, Peng L-M. Microphotoluminescence study of individual suspended ZnO nanowires. *Applied Physics Letters* 2008; **92**(11): 113112.

[163]. Fan Z, Chang P-c, Lu JG, et al. Photoluminescence and polarized photodetection of single ZnO nanowires. *Applied Physics Letters* 2004; **85**(25): 6128.
[164]. Kao CY, Hsin CL, Huang CW, et al. High-yield synthesis of ZnO nanowire arrays and their opto-electrical properties. *Nanoscale* 2012; **4**(5): 1476-80.
[165]. Ahn MW, Park KS, Heo JH, et al. Gas sensing properties of defect-controlled ZnO-nanowire gas sensor. *Applied Physics Letters* 2008; **93**(26): 263103.
[166]. Tiwale N. Zinc oxide nanowire gas sensors: fabrication, functionalisation and devices. *Materials Science and Technology* 2015; **31**(14): 1681-97.
[167]. Sinha M, Mahapatra R, Mondal B, Maruyama T, Ghosh R. Ultrafast and Reversible Gas-Sensing Properties of ZnO Nanowire Arrays Grown by Hydrothermal Technique. *The Journal of Physical Chemistry C* 2016; **120**(5): 3019-25.
[168]. Wei An XW, and X. C. Zeng*. Adsorption of O_2, H_2, CO, NH_3, and NO_2 on ZnO Nanotube: A Density Functional Theory Study. *J Phys Chem C* 2008; **112**(5747-5755).
[169]. Giri PK, Bhattacharyya S, Singh DK, Kesavamoorthy R, Panigrahi BK, Nair KGM. Correlation between microstructure and optical properties of ZnO nanoparticles synthesized by ball milling. *Journal of Applied Physics* 2007; **102**(9): 093515.
[170]. Lupan O, Pauporté T, Viana B, Aschehoug P. Electrodeposition of Cu-doped ZnO nanowire arrays and heterojunction formation with p-GaN for color tunable light emitting diode applications. *Electrochimica Acta* 2011; **56**(28): 10543-9.
[171]. Ghosh A, Guha P, Thapa R, et al. Tuning the work function of randomly oriented ZnO nanostructures by capping with faceted Au nanostructure and oxygen defects: enhanced field emission experiments and DFT studies. *Nanotechnology* 2016; **27**(12): 125701.
[172]. https://en.wikipedia.org/wiki/Scanning_electron_microscope.
[173]. https://en.wikipedia.org/wiki/Energy-dispersive_X-ray_spectroscopy.
[174]. https://en.wikipedia.org/wiki/Transmission_electron_microscopy.
[175]. https://en.wikipedia.org/wiki/X-ray_photoelectron_spectroscopy.
[176]. https://en.wikipedia.org/wiki/Photoluminescence.
[177]. https://en.wikipedia.org/wiki/Ultraviolet%E2%80%93visible_spectroscopy.
[178]. https://en.wikipedia.org/wiki/Confocal_microscopy.
[179]. https://en.wikipedia.org/wiki/Time-resolved_spectroscopy.
[180]. https://en.wikipedia.org/wiki/Conductive_atomic_force_microscopy.
[181]. Kim S-H, Jeong S-W, Hwang D-K, Park S-J, Seong T-Y. Zn ⁄ Au Ohmic Contacts on n-Type ZnO Epitaxial Layers for Light-Emitting Devices. *Electrochemical and Solid-State Letters* 2005; **8**(8): G198.
[182]. Das AK, Srinivasan A. Evidence of oxygen defect induced ferromagnetism in heat treated electrospun ZnO nanowires. *Journal of Magnetism and Magnetic Materials* 2016; **404**: 190-6.
[183]. Liu W, Li W, Hu Z, Tang Z, Tang X. Effect of oxygen defects on ferromagnetic of undoped ZnO. *Journal of Applied Physics* 2011; **110**(1): 013901.
[184]. Bera A, Basak D. Role of defects in the anomalous photoconductivity in ZnO nanowires. *Applied Physics Letters* 2009; **94**(16): 163119.
[185]. He M-R, Xiao P, Zhao J, Dai S, Ke F, Zhu J. Quantifying the defect-dominated size effect of fracture strain in single crystalline ZnO nanowires. *Journal of Applied Physics* 2011; **109**(12): 123504.
[186]. Appavoo K, Liu M, Sfeir MY. Role of size and defects in ultrafast broadband emission dynamics of ZnO nanostructures. *Applied Physics Letters* 2014; **104**(13): 133101.
[187]. Djurišić AB, Leung YH, Tam KH, et al. Defect emissions in ZnO nanostructures. *Nanotechnology* 2007; **18**(9): 095702.

[188]. Lord AM, Ward MB, Evans JE, et al. Enhanced Long-Path Electrical Conduction in ZnO Nanowire Array Devices Grown via Defect-Driven Nucleation. *The Journal of Physical Chemistry C* 2014; **118**(36): 21177-84.
[189]. Sharma PK, Pandey AC, Zolnierkiewicz G, Guskos N, Rudowicz C. Relationship between oxygen defects and the photoluminescence property of ZnO nanoparticles: A spectroscopic view. *Journal of Applied Physics* 2009; **106**(9): 094314.
[190]. Jin H-J, Oh S-H, Park C-B. Unidirectional variation of lattice constants of Al–N-codoped ZnO films by RF magnetron sputtering. *Applied Surface Science* 2008; **254**(7): 2207-10.
[191]. Jie J, Morita A, Shirai H. Role of oxygen atoms in the growth of magnetron sputter-deposited ZnO films. *Journal of Applied Physics* 2010; **108**(3): 033521.
[192]. Walter Water S-YC. Physical and structural properties of ZnO sputtered films. *Materials Letters* 2002; **55**: 67-72.
[193]. Wang L, Pu Y, Chen YF, et al. MOCVD growth of ZnO films on Si(111) substrate using a thin AlN buffer layer. *Journal of Crystal Growth* 2005; **284**(3-4): 459-63.
[194]. Chien C-T, Wu M-C, Chen C-W, et al. Polarization-dependent confocal Raman microscopy of an individual ZnO nanorod. *Applied Physics Letters* 2008; **92**(22): 223102.
[195]. Ngo-Duc T, Singh K, Meyyappan M, Oye MM. Vertical ZnO nanowire growth on metal substrates. *Nanotechnology* 2012; **23**(19): 194015.
[196]. Chen ZQ, Kawasuso A, Xu Y, et al. Production and recovery of defects in phosphorus-implanted ZnO. *Journal of Applied Physics* 2005; **97**(1): 013528.
[197]. Zheng JH, Jiang Q, Lian JS. Synthesis and optical properties of flower-like ZnO nanorods by thermal evaporation method. *Applied Surface Science* 2011; **257**(11): 5083-7.
[198]. Chang YC, Chen LJ. ZnO Nanoneedles with Enhanced and Sharp Ultraviolet Cathodoluminescence Peak. *J Phys Chem C* 2007; **111**: 1268-72.
[199]. Shalish I, Temkin H, Narayanamurti V. Size-dependent surface luminescence in ZnO nanowires. *Physical Review B* 2004; **69**(24).
[200]. Wang J, Zhuang H, Li J, Xu P. Synthesis, morphology and growth mechanism of brush-like ZnO nanostructures. *Applied Surface Science* 2011; **257**(6): 2097-101.
[201]. Yang Y, Tay BK, Sun XW, et al. Quenching of surface-exciton emission from ZnO nanocombs by plasma immersion ion implantation. *Applied Physics Letters* 2007; **91**(7): 071921.
[202]. Xing G, Wang D, Yi J, et al. Correlated d^0 ferromagnetism and photoluminescence in undoped ZnO nanowires. *Applied Physics Letters* 2010; **96**(11): 112511.
[203]. Hahn EE. Some Electrical Properties of Zinc Oxide Semiconductor. *Journal of Applied Physics* 1951; **22**(7): 855.
[204]. Børseth TM, Svensson BG, Kuznetsov AY, Klason P, Zhao QX, Willander M. Identification of oxygen and zinc vacancy optical signals in ZnO. *Applied Physics Letters* 2006; **89**(26): 262112.
[205]. Fan Z, Wang D, Chang P-C, Tseng W-Y, Lu JG. ZnO nanowire field-effect transistor and oxygen sensing property. *Applied Physics Letters* 2004; **85**(24): 5923.
[206]. Wang W, Xiong HD, Edelstein MD, et al. Low frequency noise characterizations of ZnO nanowire field effect transistors. *Journal of Applied Physics* 2007; **101**(4): 044313.
[207]. Leiter F, Alves H, Pfisterer D, Romanov NG, Hofmann DM, Meyer BK. Oxygen vacancies in ZnO. *Physica B: Condensed Matter* 2003; **340-342**: 201-4.
[208]. Quemener V, Vines L, Monakhov EV, Svensson BG. Electronic properties of vacancy related defects in ZnO induced by mechanical polishing. *Applied Physics Letters* 2011; **99**(11): 112112.

[209]. Studenikin SA, Golego N, Cocivera M. Fabrication of green and orange photoluminescent, undoped ZnO films using spray pyrolysis. *Journal of Applied Physics* 1998; **84**(4): 2287.
[210]. Liu X. Growth mechanism and properties of ZnO nanorods synthesized by plasma-enhanced chemical vapor deposition. *Journal of Applied Physics* 2004; **95**(6): 3141.
[211]. Zuo A, Hu P, Bai L, Yuan F. Synthesis of tunable 3D ZnO architectures assemblied with nanoplates. *Crystal Research and Technology* 2009; **44**(6): 613-8.
[212]. Zeng H, Cai W, Hu J, Duan G, Liu P, Li Y. Violet photoluminescence from shell layer of Zn/ZnO core-shell nanoparticles induced by laser ablation. *Applied Physics Letters* 2006; **88**(17): 171910.
[213]. Huang GS, Wu XL, Yang LW, Shao XF, Siu GG, Chu PK. Dependence of blue-emitting property on nanopore geometrical structure in Al-based porous anodic alumina membranes. *Applied Physics A* 2005; **81**(7): 1345-9.
[214]. Vassiliou JK, Mehrotra V, Russell MW, et al. Magnetic and optical properties of γ-Fe_2O_3 nanocrystals. *Journal of Applied Physics* 1993; **73**(10): 5109.
[215]. Mechanics of Materials Volume 1: An Introduction to the Mechanics of Elastic and Plastic Deformation of Solids and Structural Materials, E. J. Hearn, Butterworth-Heinemann, Oxford, 3rd edn, 1997.
[216]. Reshchikov MA, Morkoç H, Nemeth B, et al. Luminescence properties of defects in ZnO. *Physica B: Condensed Matter* 2007; **401-402**: 358-61.
[217]. Djurišić AB, Leung YH, Tam KH, et al. Green, yellow, and orange defect emission from ZnO nanostructures: Influence of excitation wavelength. *Applied Physics Letters* 2006; **88**(10): 103107.
[218]. Hsu NE, Hung WK, Chen YF. Origin of defect emission identified by polarized luminescence from aligned ZnO nanorods. *Journal of Applied Physics* 2004; **96**(8): 4671.
[219]. Vanheusden K, Warren WL, Seager CH, Tallant DR, Voigt JA, Gnade BE. Mechanisms behind green photoluminescence in ZnO phosphor powders. *Journal of Applied Physics* 1996; **79**(10): 7983.
[220]. Vidya R, Ravindran P, Fjellvåg H, et al. Energetics of intrinsic defects and their complexes in ZnO investigated by density functional calculations. *Physical Review B* 2011; **83**(4).
[221]. Ahn CH, Han WS, Kong BH, Cho HK. Ga-doped ZnO nanorod arrays grown by thermal evaporation and their electrical behavior. *Nanotechnology* 2009; **20**(1): 015601.
[222]. Wong KM*, Alay-e-Abbas SM, Shaukat A, Fang Y, Lei Y. First-principles investigation of the size-dependent structural stability and electronic properties of O-vacancies at the ZnO polar and non-polar surfaces. *Journal of Applied Physics* 2013; **113**(1): 014304. (*email addresses : km2002wong@gmail.com, km2002wong@yahoo.com.sg, kmwong@kinmunwong.me)
[223]. Wong KM*, Alay-e-Abbas SM, Fang Y, Shaukat A, Lei Y. Spatial distribution of neutral oxygen vacancies on ZnO nanowire surfaces: An investigation combining confocal microscopy and first principles calculations. *Journal of Applied Physics* 2013; **114**(3): 034901. (*email addresses : km2002wong@gmail.com, km2002wong@yahoo.com.sg, kmwong@kinmunwong.me)
[224]. Chichibu SF, Onuma T, Kubota M, et al. Improvements in quantum efficiency of excitonic emissions in ZnO epilayers by the elimination of point defects. *Journal of Applied Physics* 2006; **99**(9): 093505.
[225]. A. F. Kohan GC, D. Morgan and Chris G. Van de Walle. First-principles study of native point defects in ZnO. *PHYSICAL REVIEW B* 2000; **61**: 15019-27.

[226]. Reparaz JS, Güell F, Wagner MR, Hoffmann A, Cornet A, Morante JR. Size-dependent recombination dynamics in ZnO nanowires. *Applied Physics Letters* 2010; **96**(5): 053105.
[227]. Hong S, Joo T, Park WI, Jun YH, Yi G-C. Time-resolved photoluminescence of the size-controlled ZnO nanorods. *Applied Physics Letters* 2003; **83**(20): 4157.
[228]. Georgobiani AN, Gruzintsev AN. Effect of surface morphology on manganese ion luminescence kinetics in ZnS:Mn^{2+} films. *Inorganic Materials* 2011; **47**(2): 107-11.
[229]. Lee SK, Chen SL, Hongxing D, et al. Long lifetime of free excitons in ZnO tetrapod structures. *Applied Physics Letters* 2010; **96**(8): 083104.
[230]. Pozina G, Yang LL, Zhao QX, Hultman L, Lagoudakis PG. Size dependent carrier recombination in ZnO nanocrystals. *Applied Physics Letters* 2010; **97**(13): 131909.
[231]. Chia CH, Lai YJ, Han TC, Chiou JW, Hu YM, Chou WC. High-excitation effect on photoluminescence of sol-gel ZnO nanopowder. *Applied Physics Letters* 2010; **96**(8): 081903.
[232]. Lenchyshyn LC, Thewalt MLW, Houghton DC, et al. Photoluminescence mechanisms in thin $Si_{1-x}Ge_x$ quantum wells. *Physical Review B* 1993; **47**(24): 16655-8.
[233]. Ip K, Thaler GT, Yang H, et al. Contacts to ZnO. *Journal of Crystal Growth* 2006; **287**(1): 149-56.
[234]. Ashkenov N, Mbenkum BN, Bundesmann C, et al. Infrared dielectric functions and phonon modes of high-quality ZnO films. *Journal of Applied Physics* 2003; **93**(1): 126.
[235]. C. Brezinski HoCFaPA, Springer BH, 1991.
[236]. Kim YS, Park CH. Rich variety of defects in ZnO via an attractive interaction between O vacancies and Zn interstitials: origin of n-type doping. *Physical review letters* 2009; **102**(8): 086403.
[237]. Oba F, Nishitani SR, Isotani S, Adachi H, Tanaka I. Energetics of native defects in ZnO. *Journal of Applied Physics* 2001; **90**(2): 824.
[238]. Wang LL, Gong SD, Wu LH, Li XJ. Field emission from zinc oxide nanorod bundles grown on silicon nanoporous pillar array. *Applied Surface Science* 2013; **270**: 124-7.
[239]. Kuo F-L, Li Y, Solomon M, Du J, Shepherd ND. Workfunction tuning of zinc oxide films by argon sputtering and oxygen plasma: an experimental and computational study. *Journal of Physics D: Applied Physics* 2012; **45**(6): 065301.
[240]. Jiansheng Jie GW, Xinhai Han, and J. G. Hou. Synthesis and Characterization of ZnO:In Nanowires with Superlattice Structure. *J Phys Chem B* 2004; **108**: 17027-31.
[241]. Chan Woong, Na SYB, and Jeunghee Park. Short-Period Superlattice Structure of Sn-Doped $In_2O_3(ZnO)_4$ and $In_2O_3(ZnO)_5$ Nanowires. *J Phys Chem B* 2005; **109**: 12785-90
[242]. Xitian Zhang HL, Hong Gao, Xiaojing Wang, Haiyang Xu, Quan Li, and Suikong Hark. Crystal Structure of $In_2O_3(ZnO)_m$ Superlattice Wires and Their Photoluminescence Properties. *Crystal Growth & Design* 2009; **9**(1): 364-7.
[243]. Z. R. Dai ZWPaZLW. Novel Nanostructures of Functional Oxides Synthesized by Thermal Evaporation *Adv, Funct, Mater,* 2003; **12**(1): 9-24.
[244]. Wander A, Schedin F, Steadman P, et al. Stability of polar oxide surfaces. *Physical review letters* 2001; **86**(17): 3811-4.
[245]. Zhu YW, Zhang HZ, Sun XC, et al. Efficient field emission from ZnO nanoneedle arrays. *Applied Physics Letters* 2003; **83**(1): 144.
[246]. Qian X, Liu H, Guo Y, Song Y, Li Y. Effect of Aspect Ratio on Field Emission Properties of ZnO Nanorod Arrays. *Nanoscale research letters* 2008; **3**(8): 303-7.
[247]. Jie J, Wang G, Han X, et al. Indium-doped zinc oxide nanobelts. *Chemical Physics Letters* 2004; **387**(4-6): 466-70.
[248]. https://en.wikipedia.org/wiki/Supercapacitor.

[249]. Grote F, Wen L, Lei Y. Nano-engineering of three-dimensional core/shell nanotube arrays for high performance supercapacitors. *Journal of Power Sources* 2014; **256**: 37-42.
[250]. Gu Z, Nan H, Geng B, Zhang X. Three-dimensional $NiCo_2O_4$@$NiMoO_4$ core/shell nanowires for electrochemical energy storage. *J Mater Chem A* 2015; **3**(22): 12069-75.
[251]. Guo D, Zhang P, Zhang H, et al. $NiMoO_4$ nanowires supported on Ni foam as novel advanced electrodes for supercapacitors. *Journal of Materials Chemistry A* 2013; **1**(32): 9024.
[252]. Li L, Zhang YQ, Liu XY, et al. One-dimension $MnCo_2O_4$ nanowire arrays for electrochemical energy storage. *Electrochimica Acta* 2014; **116**: 467-74.
[253]. Liu M-C, Kong L-B, Lu C, et al. Design and synthesis of $CoMoO_4$-$NiMoO_4 \cdot xH_2O$ bundles with improved electrochemical properties for supercapacitors. *J Mater Chem A* 2013; **1**(4): 1380-7.
[254]. Ma X-J, Kong L-B, Zhang W-B, Liu M-C, Luo Y-C, Kang L. Design and synthesis of 3D Co_3O_4@$MMoO_4$ (M = Ni, Co) nanocomposites as high-performance supercapacitor electrodes. *Electrochimica Acta* 2014; **130**: 660-9.
[255]. Mai LQ, Yang F, Zhao YL, Xu X, Xu L, Luo YZ. Hierarchical $MnMoO_4$/$CoMoO_4$ heterostructured nanowires with enhanced supercapacitor performance. *Nature communications* 2011; **2**: 381.
[256]. Wang Q, Wang X, Liu B, et al. $NiCo_2O_4$ nanowire arrays supported on Ni foam for high-performance flexible all-solid-state supercapacitors. *Journal of Materials Chemistry A* 2013; **1**(7): 2468.
[257]. Zhang H, Wang J, Shan Q, Wang Z, Wang S. Tunable electrode morphology used for high performance supercapacitor: Polypyrrole nanomaterials as model materials. *Electrochimica Acta* 2013; **90**: 535-41.
[258]. Cai D, Huang H, Wang D, et al. High-performance supercapacitor electrode based on the unique ZnO@Co_3O_4 core/shell heterostructures on nickel foam. *ACS Appl Mater Interfaces* 2014; **6**(18): 15905-12.
[259]. Chi-Chang Hu K-HC, Ming-Champ Lin, and Yung-Tai Wu. Design and Tailoring of the Nanotubular Arrayed Architecture of Hydrous RuO_2 for Next Generation Supercapacitors. *Nano Lett,* 2006; **6**(12): 2690-5.
[260]. Xiao K, Xia L, Liu G, Wang S, Ding L-X, Wang H. Honeycomb-like $NiMoO_4$ultrathin nanosheet arrays for high-performance electrochemical energy storage. *J Mater Chem A* 2015; **3**(11): 6128-35.
[261]. Peng S, Li L, Wu HB, Madhavi S, Lou XWD. Controlled Growth of $NiMoO_4$ Nanosheet and Nanorod Arrays on Various Conductive Substrates as Advanced Electrodes for Asymmetric Supercapacitors. *Advanced Energy Materials* 2015; **5**(2): n/a-n/a.
[262]. Cai D, Liu B, Wang D, et al. Facile hydrothermal synthesis of hierarchical ultrathin mesoporous $NiMoO_4$ nanosheets for high performance supercapacitors. *Electrochimica Acta* 2014; **115**: 358-63.
[263]. Cai D, Liu B, Wang D, et al. Enhanced performance of supercapacitors with ultrathin mesoporous $NiMoO_4$ nanosheets. *Electrochimica Acta* 2014; **125**: 294-301.
[264]. Ren W, Guo D, Zhuo M, Guan B, Zhang D, Li Q. $NiMoO_4$@$Co(OH)_2$ core/shell structure nanowire arrays supported on Ni foam for high-performance supercapacitors. *RSC Adv* 2015; **5**(28): 21881-7.
[265]. Wei Hong JW, Peiwei Gong, Jinfeng Sun, Lengyuan Niu, Zhigang Yang, Zhaofeng Wang, Shengrong Yang,. Rational construction of three dimensional hybrid Co_3O_4@$NiMoO_4$ nanosheets array for energy storage application. *Journal of Power Sources* 2014; **270**: 516-25.

Scientific contributions

I have published and jointly published 14 papers in SCI-indexed international scientific journals during my Ph.D. period, including 6 papers with impact factor higher than 8 (Small, Energy & Environmental Science, Advanced Energy Materials, Advanced Functional Materials, Journal of the American Chemical Society) and 8 papers with impact factor between 2 and 8 (Applied Catalysis B: Environmental, Nanoscale, Chemistry-A European Journal, Journal of Materials Chemistry, Journal of Applied Physics)The published papers were cited by more than 310 times during my PhD (Data from google scholar database).

Publications in SCI-indexed Scientific Journals

1 Y. G. Fang, C.L. Wang, R. Xu, M. Peterlechner, L.Y. Wen, Y. Mi, G. Wilde, Y. Lei*, Three-dimensional ZnO/$NiMoO_4$ core-shell nanostructures for high-performance supercapacitor**.** (**Submitted**)

2. Y. G. Fang[+], K. M. Wong[+], Y. Lei*, Synthesis and field emission properties of different ZnO nanostructure arrays", ***Nanoscale Research Letters*** 2012, 7:197. (+contributed equally) (IF 2.779)

3. K. M. Wong[+], Y. G. Fang[+], A. Devaux, L. Y. Wen, J. Huang, L. De Cola, Y. Lei*, 'Assorted analytical and spectroscopic techniques for the optimization of the defect-related properties in size-controlled ZnO nanowires', ***Nanoscale*** 3, 4830-4839, 2011. (+contributed equally) (IF 7.394),

4 Zhou M., Xu Y., Xiang J.X., Wang C.L., Liang L.Y., Fang Y.G., Wen L.Y., Mi Y., Lei Y.*, 'Understanding the Orderliness of Atomic Arrangement towards Enhanced Sodium Storage', ***Advanced Energy Materials*** (Impact factor 16.146),accepted and in press, 2016.

5 Y. Mi, L.Y. We, R. Xu, Z.J. Wang, D.W. Cao, Y.G. Fang, and Y. Lei*, Constructing a AZO/TiO_2 Core/Shell Nanocone Array with Uniformly Dispersed Au NPs for Enhancing Photoelectrochemical Water Splitting, ***Adv. Energy Mater***. 2015, 1501496. (IF 16.146)

6. C.L Wang, Fang Y.G., Xu Y., Liang L.Y., Zhou M, Zhao H.P., Lei Y.*, Manipulation of Disodium Rhodizonate: Factors for Fast-Charge and -Discharge Sodium-Ion Batteries with Long-Term Cyclability, ***Advanced Functional Materials***, 2015. (IF 11.805)

7. C. Wang, Y. Xu, Y. Fang, M. Zhou, L. Liang, S. Singh, H. Zhao, A. Schober, Y. Lei*. Extended π-Conjugated System for Fast-Charge and -Discharge Sodium-Ion Batteries. ***J. Am. Chem. Soc***. 137(8), 312413130, 2015. (IF 12.113)
8. Mi Y., Wen L.Y., Wang Z.J., Cao D.W., Fang Y.G., Lei Y.*, Building of Anti-Restack 3D BiOCl Hierarchitecture by Ultrathin Nanosheets towards Enhanced Photocatalytic Activity, ***Applied Catalysis B: Environmental***, 176, 332-337, 2015.(IF 7.435)
9. Liang L.Y., Xu Y., Wang C.L., Wen L.Y., Fang Y.G., Mi Y., Zhou M., Zhao H.P., Lei Y.*, 'Large-scale Highly Ordered Sb Nanorod Arrays Anode with High Capacity and Rate Capability for Sodium-Ion Batteries', ***Energy Environ. Sci.***, 2015, **8**, 2954-2962. (IF 20.523)
10. Wen L.Y., Mi Y., Wang C.L., Fang Y.G., Grote F., Zhao H.P., Zhou M., Lei Y.*, 'Cost-effective atomic layer deposition synthesis of Pt nanotube arrays: application for high performance supercapacitor', ***Small*** (IF 8.368), 10, 3162–3168, 2014 (It was reported by Materials Views China as the hot article. http://www.materialsviewschina.com/2014/08/yuan-zi-ceng-chen-ji-ji-shu-zhi-bei-gui-jin-shu-fu-za-na-mi-jie-gou-qu-de-jin-zhan-di-jia-gao-xiao-pt-na-mi-guan-he-cheng-ji-qi-ying-yong/).
11. Wang C.L., Fang Y.G., Wen L.Y., Zhou M., Xu Y., Zhao H.P., De Cola L.*, Hu W.P.*, Lei Y.*, 'Vectorial diffusion for facile solution-processed self-assembly of insoluble semiconductors: a case study on metal phthalocyanines', ***Chemistry-A European Journal,*** 20, 10990-10995, 2014. (IF 5.731)
12. Wang C.L., Wen L.Y., Kups T., Mi Y., Vellacheri R., Fang Y.G., Schaaf P., Zhao H.P., Lei Y.*, 'Growth control of AgTCNQ nanowire arrays by using a template-assisted electro-deposition method', ***Journal of Materials Chemistry C*** (backside cover paper), 1, 8003-8006, 2013 (was selected as the inside cover). (IF 4.696)
13. K. M. Wong*, S. M. Alay-e-Abbas, Y. G. Fang, A. Shaukat, Y. Lei*, "Spatial distribution of neutral oxygen vacancies on ZnO nanowire surfaces: An investigation combining confocal microscopy and first principles calculations", ***Journal of Applied Physics,*** 114 (3), 034901-1 to 034901-10, 2013 (IF 2.183) ([+]email: km2002wong@ gmail.com)
14. K. M. Wong*, S. M. Alay-e-Abbas, A. Shaukat, Y. G. Fang, Y. Lei*, "First-principles investigation of the size-dependent structural stability and electronic properties of O-vacancies at the ZnO polar and non-polar surfaces", ***Journal of Applied Physics,*** 113 (1),

014304-1 to 014304-11, 2013. (IF 2.183), This JAP article was the most highly cited regular article among over 4000 JAP articles that was published in the year 2013.

15. L. Y. Wen, K. M. Wong, Y. G. Fang, M. H. Wu, Y. Lei*, 'Fabrication and characterization of well-aligned, high density ZnO nanowire arrays and their realizations in Schottky device applications using a two-step approach', ***Journal of Materials Chemistry***, 21, 7090-7097, 2011 (IF 6.626) (It was selected as one of the hot articles in RSC blog. http://blogs.rsc.org/jm/2011/05/10/hot-articles-on-nanowire-arrays-for-schottky-diodes-an-anticancer-bio-conjugate-and-a-flower-like-sensor/).

Conference posters and talk

1. Y. G. Fang, K. M. Wong, A. Devaux, L.Y. Wen, L. De Cola and Y. Lei*, " Fabrication and the characterization of the electrical, optical and field emission properties of regular ZnO and PbSe nanowires arrays", 76th Annual Conference of the DPG, April 25-30, 2012, Berlin, Germany.
2. Y. G. Fang, K. M. Wong, Y. Mi, L.Y. Wen, G. Wilde, Y. Lei*, "Polystyrene spheres assisted anodization method for the preparation of size-controlled pore diameter and separation in the AAO template", 77th Annual Conference of the DPG, Mar 10-15, 2013, Regensburg, Germany.
3. Y. G. Fang, K. M. Wong, G. Wilde, Yong Lei, "Hierarchical $NiMoO_4$@MnO_2 core-shell heterostructured nanowire arrays on Ni foam ashigh-performance supercapacitor electrodes," 78th Annual Conference of the DPG, 30.03.-04.04.2014, Dresden, Germany.
4. Wong K.M., Wen L.Y., Fang Y.G., Grote F., Sun H., Lei Y., 'Fabrication and Characterization of Well-Aligned Zinc Oxide Nanowire Arrays and their realizations in Schottky-Device Applications', 75th Annual Conference of the DPG, March 13-18, 2011, Dresden, Germany. **Talk**

Acknowledgment

Foremost, I wish to express my sincere gratitude to my advisor Prof. Dr. Yong Lei for providing me the opportunity to finish my Ph.D. thesis in his research group at Technische Universität Ilmenau. My special thanks go to him for his support and guidance during the four and half years. When I get problems in my research, he always gives me important and constructive advices. To improve my research abilities, he often encourages me to join in many academic activities. Besides the academic fields, I also would like to thank Prof. Dr. Yong Lei for his help in daily life.

I would like to thank Prof. Dr. Gerhard Wilde for providing many convenient conditions in his group at the University of Münster. This is very important for me to complete my thesis. During the four years in his group, many wonderful memories have been left in my mind.

Moreover, I would like to thank all the colleagues form our group for not only the academic issues but also daily life. My special appreciation goes to Dr. Kin Mun Wong for his guidance, analysis and discussion for my research works as well as optimizing the experiments with additional first principle simulations and calculations. Many thanks go to Mr. Rui Xu for the electrochemical measurements and Dr. Chengliang Wang, Dr. Liaoyong, Wen, and Dr. Yan Mi, Dr. Zhijie Wang for the samples characterizations. Also, I also want to thanks for Dr. Min Zhou, Ms Liying Liang, Dr. Huaping Zhao, Dr. Yang Xu, Dr. Ahmed Shukur Hameed Al-Haddad, Mrs. Moumou Li, and Mr. Ranjith Vellacheri for their fruitful discussions and helps.

For HRTEM, XRD, SEM measurements, I would like to thank Dr. Martin Peterlechner and Dr. Harald Rösner for their helps and time in University of Münster. I also would like to thank Dipl. Phys. Stefan Ostendorp and Dr. Nina Winkler for supplying helps in the lab.

It is a great pleasure to work together with you all.

Last but not the least, I would like to thank everyone who helped me.

Wish you all a good health, a happy family and all the best!

Declaration

I hereby declare that this Ph.D. dissertation entitled “Structural Parameters (Size, Defect and Doping) of ZnO Nanostructures and Relations with their Optical and Electrical Properties” was carried out by me for the degree of Doctor of Philosophy under the supervision of Prof. Dr. Yong Lei. All the dates or information in this thesis that have been directly or indirectly consulted or used from other sources are clearly stated. This dissertation has not been submitted, in part or in whole, for any other degree or examination in any other University. I have acknowledged all main sources of help, and I have made clear exactly what was done by others and what I have contributed when the work was done jointly with others. Some of the results may have been published in scientific journals or elsewhere. I am aware that the falsity of this declaration will be regarded as an attempt of deception and will cause the derogation of the doctoral procedure.